Impact of Climate Change on Flood Inundation in the Lower Mekong Basin Considering Various Sources of Climate Outputs

Try Sophal

2021

Impact of Climate Change on Flood Inundation in the Lower Mekong Basin Considering Various Sources of Climate Outputs

by

Try Sophal

A Dissertation

Submitted in partial fulfillment of the
requirement for the Degree of Doctor of Engineering

Kyoto University

March 2021

ACKNOWLEDGEMENT

This thesis is the result of three years of work in the International Doctoral Program in Kyoto University, Japan. The favorable outcome of this thesis would not have been achievable without the priceless contribution of many people.

First of all, I would like to express my deepest gratitude to Professor Kaoru Takara for his acceptance granted me the opportunity to come to Japan as a research student in former Takara lab (now Sayama lab). Before he officially left DPRI, he had indeed introduced me to Tanaka lab to further my doctoral course in Kyoto University.

Secondly, I would like to express my sincere gratitude to my supervisor, Professor Shigenobu Tanaka, for his supervision, support, and acceptance which allowed me to become member of Tanaka lab. I deeply appreciate his valuable supervision, knowledge sharing, and advice during these three years of my doctoral program in Japan.

I would also like to recognize my co-supervisor, Associate Professor Kenji Tanaka, for his valuable comments and suggestions in this thesis. These were beyond my ability; thus, without his kind help and support, this thesis could not be done successfully.

I gratefully acknowledge my co-supervisor, Associate Professor Takahiro Sayama, for his great achievement of developing the RRI model which is the major tool used in this thesis. More importantly, I would like to specifically thank him for providing technical support and scientific discussion and comments on the work inside this thesis.

Special thanks equally go to Dr. Oeurng Chantha, for his advice, suggestion, and support with observed hydrological data used in this thesis. Without his support, this thesis would not have successfully completed.

I convey special acknowledgement to my previous supervisors, Associate Professor Lee Giha during my master's degree in Kyungpook National University, Republic of Korea and Dr. Ly Sarann and Dr. Oeurng Chantha during my engineer's degree in the Institute of Technology of Cambodia, Kingdom of Cambodia for their guidance and advice, providing strong basic knowledge of hydrology and water resources.

I would like to thank all members of Tanaka's laboratory: Dr. Tim San, Dr. Hu San, Shiojiri San, Hiraoka San, Sanjar San, Hino San, Hak San, Tasaka San, Inagaki San, Iwakawa San, Kobayashi San, and Yamada San for forming a formidable team and conducive working environment in Tanaka lab. Many thanks also go to all members in Sayama lab for creating such a joyful research environment during my research student there.

I also thank to the secretary in Tanaka lab, Kawasaki San, Furutani San, and Sawada San and secretary in former Takara lab, Inoue San and Saidera San, for their support on administrative work during my study in Kyoto University.

I would like to say thanks to my parents for fulfilling their parental and financial obligation since my childhood and throughout my studies. I am thankful to all of my siblings and relatives for their contribution in form of advice and support towards successful completion of this thesis. Especially, special thank goes to Hengkungkea Mak for her time and effort on English correction and proof reading.

I would like to appreciate all professors and lecturers at Kyoto University, Kyungpook National University, and Institute of Technology of Cambodia for their knowledge sharing. Great thanks to all friends, seniors, and juniors who have always willingly discussed and shared the necessary knowledge.

Last but not least, this thesis is not possible to be done without financial support from Japan International Cooperation Agency (JICA) during AUN-SEED/Net Doctoral Scholarship Program in Japan Phase 3. I gratefully thank to all JICA Kansai staffs, especially

responsible persons for AUN-SEED/Net Program: Miyashita San, Inoue San, Hirai San, and Aoki San, for their warm care and support during my stay in Japan.

Although I cannot mention all those from whom I received the help, and I am sure that their support and encouragement were the powerful force in making this thesis successfully.

Sophal Try

Kyoto University, 30 November, 2020

ABSTRACT

Climate change has become one among the global concerns and is currently affecting the resilience of aquatic ecosystem worldwide. Through the increase of greenhouse gas emission and global mean temperature, climate change is able to alter the spatiotemporal patterns of rainfall which poses a great impact on river flow and flood inundation. In the Mekong River Basin (MRB), annual flooding, being an important hydrological characteristic, drives the high productivity of the ecosystem and biodiversity in the Tonle Sap Lake as well as the Mekong Delta. Therefore, changing the annual river flow and flood inundation in the MRB seriously affects the biodiversity production and people's daily lives.

This thesis aims to provide more understanding of the characteristics of flood inundation and estimate the effects of climate change on flood inundation in the MRB by considering various sources of climate outputs. The main focuses of this thesis are explained as the following.

Firstly, prior to the study on climatic impacts, the validated long-term historical precipitation in the MRB is importantly required, and the gauged observation is currently not available enough for the climate change study in this thesis. Therefore, the performance of five gridded precipitation datasets including APHRODITE, GPCC, PERSIANN-CDR, GSMaP, and TRMM were evaluated with the available gauged rainfall (2000–2007). The results showed that GPCC and TRMM performed satisfactorily in simulating river discharge in the MRB. Since the GPCC dataset is available for longer periods (1982–2016), it is used for reference precipitation and historical discharge simulation for climate change study in the followings.

Secondly, the large ensemble climate dataset (d4PDF), which consists of 100 ensemble members in the historical (1951–2010) and 90 members in the future (2051–2110) projections, was used to calculate the frequency changes of extreme flood inundation in the Lower Mekong Basin (LMB). Under 4 K increasing scenario, the results of extreme flood

events showed an increase in peak discharge by 25%, 33%, and 40%; inundation extent by 19%, 29%, and 36%; and inundation volume by 23%, 34%, and 37% for 50-year, 100-year, and 1000-year return periods, respectively.

In addition, the effects of climate change in the LMB were estimated from the present climate (1979–2003) to future climate (2075–2099) using high- (MRI-AGCM3.2H) and super-high-resolution (MRI-AGCM-3.2S) datasets. By applying with linear scaling bias correction method, the results of climate change suggested that flood magnitude in the LMB will be severer by the end of twenty-first century. The increment of precipitation of 6.6–14.2% was able to lead an increase of river flow exceeding 5% of time (Q_5) 13–30%, annual peak inundation extent 19–43%, and peak inundation volume 24–55% in the LMB for ranging of four Representative Concentration Pathways (RCPs) and four sea surface temperature (SST) scenarios.

Moreover, the performance of the new Coupled Model Intercomparison Project Phase 6 (CMIP6) for flood estimation was evaluated by comparing with the previous CMIP5. According to the performance analysis based on Taylor diagrams, the results indicated an improvement of 8 CMIP6 GCMs in terms of precipitation and flood simulation with higher correlation and less error values than the same models in CMIP5. The projection of future flood inundation in the MRB from 8 CMIP6 GCMs showed an increase of annual peak discharge at Kratie between 10.1–17.9% and 9.9–28.9% for SSP2-4.5 and SSP5-8.5 scenarios, respectively during three projection periods in the near future (2026–2050), mid future (2051–2075), and far future (2076–2100).

Last but not least, this thesis analyzed various sources of climate change outputs to assess the possible impacts of climate change on flood inundation in the MRB. Generally, the results from the large ensemble dataset (d4PDF), high- and super-high-resolution AGCM (MRI-AGCM3.2H and MRI-AGCM3.2S), and the most recent CMIP6 GCMs were consistent to reveal the significant increase of the severity and magnitude of future flood inundation in the MRB under the effect of climate change. However, the extreme flood events would vary their increasing magnitude depending on future projection scenarios. In

order to reduce the forthcoming possibility of flood damages, it requires efficient long-term water resources planning and management, flood adaptation and mitigation strategies, flood prevention infrastructure, and effective flood early warning and forecasting systems.

CONTENTS

LIST OF TABLES

LIST OF FIGURES

LIST OF ABBREVIATIONS

2-D LIE	2-D Local Inertial Equation
ACC	Flow Accumulation
AGCM	Atmospheric General Circulation Model
AMS	Annual Maximum Series
APHRODITE	Asian Precipitation Highly-Resolved Observational Data Integration Towards Evaluation
AR5	The fifth assessment report
CDF	Cumulative Distribution Function
CMIP5	Coupled Model Intercomparison Project Phase 5
CMIP6	Coupled Model Intercomparison Project Phase 6
d4PDF	database for Policy Decision making for Future climate change
DEM	Digital Elevation Model
DIR	Flow Direction
ECS	Equilibrium Climate Sensitivity
EM-DAT	Emergency Events Database
ET	Evapotranspiration
GCM	General Circulation Model
GEV	The Generalized Extreme Value
GFDL	Geophysical Fluid Dynamics Laboratory
GHG	Greenhouse gas
GISS	The Goddard Institute for Space Studies
GPCC	Global Precipitation Climatology Centre
GSMaP	Global Satellite Mapping of Precipitation
HR	Hit Ratio
IPSL	Institut Pierre Simon Laplace
JICA	Japan International Cooperation Agency
JMA-AGCM	Japanese Meteorological Agency AGCM
IPCC	Intergovernmental Panel on Climate Change

JRA-55	Japanese 55-year Reanalysis dataset
K-L	Kullback-Leibler test
K-S	The Kolmogorov-Smirnov test
LMB	Lower Mekong Basin
MERIT	Multi-Error-Removed-Improved-Terrain
MODIS	Moderate Resolution Imaging Spectroradiometer
MRB	Mekong River Basin
MRC	Mekong River Commission
NASA	National Aeronautics and Space Administration
NE	Normalized Error
NSE	Nash-Sutcliffe Efficiency
PBIAS	Percent Bias
PDF	Probability Density Function
PDR	Peak Discharge Ratio
PERSIANN-CDR	The Precipitation Estimation from Remotely Sensed Information using Artificial Neural Networks-Climate Data Record
R^2	coefficient of determination
RCP	Representative Concentration Pathway
RMSD	Root Mean Square Difference
RMSE	Root Mean Square Error
RRI	Rainfall-Runoff-Inundation model
SCE-UA	Shuffled Complex Evolution Method
SSP	Shared Socioeconomic Pathway
SST	Sea Surface Temperature
STD	Standard Deviation
SWAT	Soil and Water Assessment Tool
TR	True Ratio
TRMM	Tropical Rainfall Measuring Mission
T-SAS	Time-Space Accounting Scheme
VE	Relative Volume Error

CHAPTER 1 General Introduction

1.1 Background

Flooding is one of the major natural disasters which disturb the prosperity, safety, and amenity of human settlements (Jha et al., 2012). Flood risk is defined as the synthesis of hazardous phenomenon flooding and vulnerable system of loss which carries together with natural, human, social, economic, and environmental aspects. Nowadays, the flood risk is a damaging natural hazard in the world. The studies of flood phenomena and consequences are useful for flood control, risk reduction, improvement of resilience, and flood management. Moreover, flood forecasting and early warning are important to evacuate the residents from the likely damage. The necessary states to understand the flood phenomenon are the characteristics of hydrology, hydraulics, geography, the sensitivity of the assets, and environmental economics.

Flood risk management is extremely complex, involving public and private interests, confronting society, economy, politics, environment, religion, and nature. The economic evaluation of flood damage plays an important role in decision making. Economic analyses of flood risk are also crucial for budget determination and planning. Flood risk analysis is an indispensable tool to support land-use policy, flood management projects, including financial determination.

Complexity arises when it comes to selecting the comprehensive method and models in implementing flood damage estimations because different approaches may have different influence on estimation accuracy. Data availability is the main challenge that many researchers are facing in real practice (Messner, 2007). It is requisite to understand the impacts of data and methods used for flood damage evaluation.

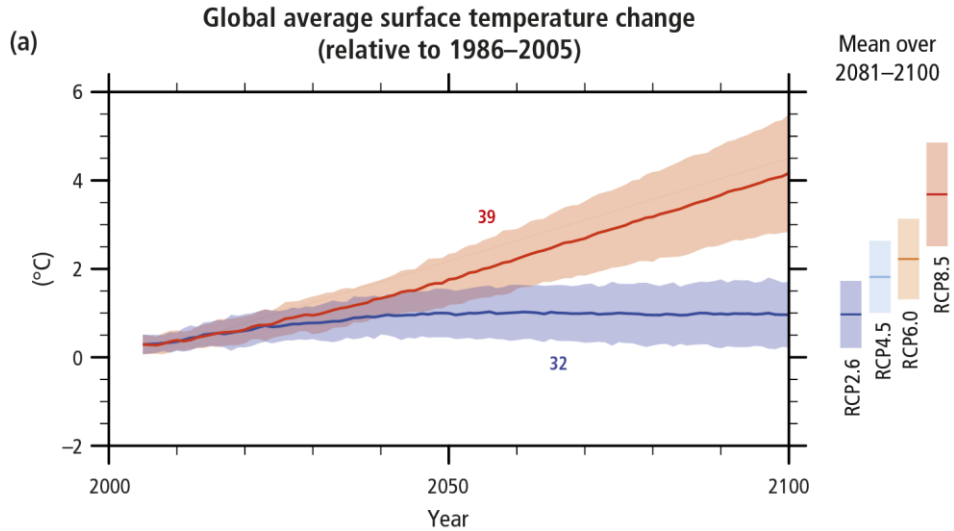

Figure 1.1 Global average surface temperature change from 2006 to 2100 from the multi-model simulation in CMIP5 relative to 1986–2005 (IPCC, 2014).

Climate change has become a global issue that attracts worldwide attention. Climate change is the major factor in changing precipitation and evapotranspiration (Wang et al., 2019), affecting the variation of river flow and flood characteristics. The changes in spatiotemporal patterns of precipitation would lead to altering the frequency and intensity of flooding in the river basin. The impacts of climate change on flooding are complicated which causes results in agricultural damages, people's life losses, economic damages, and other critical ecosystem vulnerabilities. Southeast Asia is one of the most vulnerable regions to the impact of climate change. The impacts of climate change on flooding in the Mekong River Basin (MRB), the mainland of Southeast Asia, would affect the food production, domestic water supply, transportation, and culture (MRC, 2005).

According to the Fifth Assessment Report of the Intergovernmental Panel on Climate Change (IPCC AR5), the evidence of observed climate change impacts is the strongest and most comprehensive for the natural system. The changing of precipitation and the melting of snow and ice are altering the global hydrological system. The increase of global mean surface temperature by the end of the 21st century (2081–2100) relative to 1986–2005 is

likely between 0.3°C to 1.7°C under the RCP2.6 scenario and 2.6°C to 4.8°C under the RCP8.5 scenario (Figure 1.1).

The changes in average surface temperature and average precipitation are not uniform in each region around the globe (Figure 1.2). The extreme precipitation events over the wet tropical regions will be likely more intense and frequent. The risk of climate-related impacts will increase as well as the interaction of climate-related hazards with vulnerability and exposure to human and natural systems (IPCC, 2014). Hence, it is crucial to evaluate the risk assessment from the possible range of impacts from the low greenhouse gas emission scenario (e.g. RCP2.6 in CMIP5 models) to the high emission scenario (e.g. RCP8.5). This information could increase the awareness and ability for climate change adaptation and possible risk reduction and mitigation.

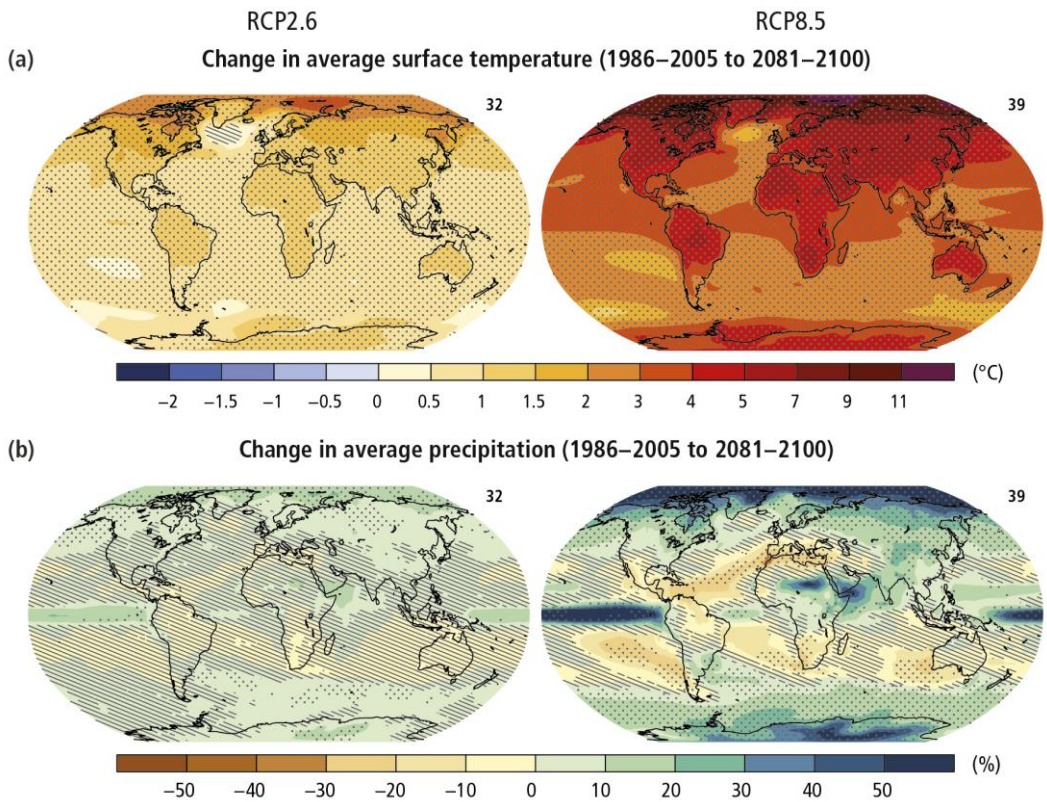

Figure 1.2 Change in average surface temperature (a) and change in average precipitation (b) based on multi-model mean projection for 2081–2100 relative to 1986–2005 under the RCP2.6 (left) and RCP8.5 (right) scenarios (IPCC, 2014).

1.2 Objectives

This thesis aims to provide the analysis on the determination of the impacts of climate change on flood inundation in the MRB by considering various sources of climate outputs. The detailed principle objectives are as the following.

- To evaluate the performance of satellite-based precipitation products for flood inundation modeling in the MRB.
- To determine the effective duration of precipitation which is highly correlated to peak flood inundation in the LMB.
- To examine the changes in effective duration from the present to the future projection climate in the MRB.
- To address the changes in flood characteristics of extreme events from the present to the future climate projections.
- To investigate the changes in flood characteristics from the present to the future climate by considering various emission scenarios and sea surface temperature scenarios.
- To evaluate the performance of the recent climate dataset CMIP6 by comparing to the previous CMIP5 for the projections of future flood inundation in the MRB.

1.3 Outline of Thesis

This thesis attempts to deal with multiple sources of climate datasets for climate change assessment on flood inundation in the MRB. This thesis consists of seven chapters which can be seen in Figure 1.3. Chapter 1 presents a general introduction, and Chapter 2 describes the study site and rainfall-runoff-inundation modeling used in this study. Chapter 3 explains the evaluation of the performance of satellite-based precipitation products for rainfall-runoff and flood inundation modeling in the MRB where gauged observed availability is quite limited. Chapter 4 focuses on the investigation of projection of future extreme flood inundation events by using a large ensemble climate dataset. Chapter 5 shows assessing the effects of climate change on flood inundation using high resolutions AGCM outputs by considering various future projected scenarios. Then, Chapter 6 presents the performance

evaluation of CMIP5 and CMIP6 climate projection GCMs for flood inundation in the MRB.

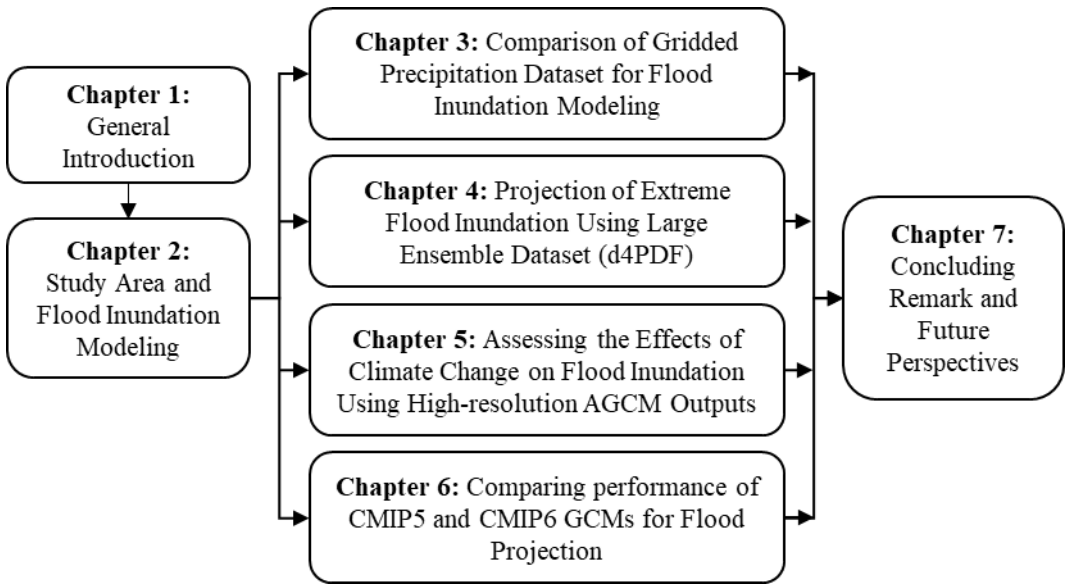

Figure 1.3 Roadmap of this thesis.

Chapter 1 presents the background of the study on flood inundation modeling, climate change impacts, the principle objectives, and the key contents implemented in this thesis.

Chapter 2 describes the basic information and characteristics of the study area of the MRB, including climate, situation of flood characteristics, and the rainfall-runoff-inundation (RRI) model mainly used as a modeling tool in this dissertation.

Chapter 3 addresses the performance of satellite-based precipitation products (namely as APHRODITE, GPCC, PERSIANN, GSMaP, and TRMM) for flood inundation modeling in the MRB by comparing their performance with the available gauged observation period (2000–2007). The best performing gridded precipitation (high accuracy and less error) dataset is used for reference and long-term historical simulation of the RRI model in climate change study in the following chapters.

Chapter 4 firstly defines the effective duration of precipitation prior to peak flood inundation and assesses the changes of effective precipitation and extreme flood inundation events (i.e. 50-year, 100-year, and 1000-year return periods) from the present to future projections in the MRB. This study used a large ensemble climate dataset (d4PDF) which consists of 6000-year (60-year: 1950-2010 × 100-ensemble) in the present and 5400-year (60-year: 2050–2110 × 90-ensemble) in the future. The changes in peak river discharge, inundation extent, and inundation volume from present to future climate were evaluated.

Chapter 5 provides the impact assessment of climate change from the present (1979–2003) to the future (2075–2099) climate, considering four greenhouse gas emission scenarios (RCP2.6, RCP4.5, RCP4.5, and RCP8.5) and four different sea surface temperature patterns (SSTs). The changes in annual precipitation, Q_5 (high flow exceeding 5% of the time), peak inundation area, and peak inundation volume were figured out from present to future.

Chapter 6 shows the performance evaluation of the most recent climate dataset CMIP6 from the Intergovernmental Panel on Climate Change (IPCC) by comparing with CMIP5. The temporal and spatial distribution of 8 general circulation models (GCMs) from the same institution in CMIP5 and CMIP6 were evaluated.

Finally, Chapter 7 summarizes the thesis with concluding remarks, research limitations, and further perspective of this dissertation.

References

IPCC, (2014). Climate Change 2014: Synthesis Report. Contribution of Working Groups I, II and III to the Fifth Assessment Report of the Intergovernmental Panel on Climate Change [Core Writing Team, R.K. Pachauri and L.A. Meyer (eds.)]. IPCC, Geneva, Switzerland, 151 pp.

Jha, A. K., Bloch, R., and Lamond, J. (2012). Cities and flooding: a guide to integrated urban flood risk management for the 21st century: World Bank Publications.

Mekong River Commission (MRC), (2005). Overview of the hydrology of the Mekong Basin (Vol. 82). Vientiane, Lao PDR.

Messner, F. (2007). Evaluating flood damages: guidance and recommendations on principles and methods: Helmholz Unweltforschungszentrum (UFZ).

Wang, H., Xiao, W., Wang, Y., Zhao, Y., Lu, F., Yang, M., Hou B., and Yang, H. (2019). Assessment of the impact of climate change on hydropower potential in the Nanliujiang River basin of China. *Energy*, 167, 950–959. doi: 10.1016/j.energy.

CHAPTER 2 Study Area and Flood Inundation Modeling

2.1 The Study Area

2.1.1 The Mekong River Basin

The Mekong River is one of the largest river basins in the world. Its drainage area, 795,000 km^2, lies in China, Myanmar, Lao PDR, Thailand, Cambodia, and Vietnam (Figure 2.1; Table 2.1). Annual flooding is an important hydrological characteristic of the MRB where it drives the high productivity of ecosystems and biodiversity (Lamberts and Koponen, 2008), particularly the Tonle Sap floodplain and the Mekong Delta (Kummu et al., 2006). The population is approximately 69 million (Varis et al., 2012). The mean annual discharge of the basin was 14,500 m^3/s (MRC, 2005). The annual hydrological regimes in the MRB had a strong seasonal change. The MRB is located in the tropical monsoon climate with two seasons: rainy season (May–October) and dry season (November–April) (MRC, 2005). The flood season, accounting for 80–90% of annual flow, is exclusively essential for maintaining the aquatic ecosystem in the basin (MRC, 2010).

The annual flood pulse drives benefits in the environmental, social, and economic sectors in the LMB greater than any other river basins in the world. For example, flood deposited the sediments, improving the natural soil fertilizers for agriculture across the LMB floodplains. The flood can flush and transport the polluted water out of the basin. Moreover, the river system supports many sectors including fisheries, navigation, and hydropower. The annual flooding significantly contributes to recharging the groundwater table and maintaining the river morphology. In the dry season, the floodwater, stored from flood season, is used for agricultural irrigation.

Most areas in the LMB are prone to flooding (Try et al., 2019) with significant annual flood economic damages of approximately US$ 60–70 million (MRC, 2011). Flood damage in the Mekong region has increased dramatically from 1984 to 2017 (Try et al., 2018a), and the frequency and severity of extreme flood events have also increased in the LMB (Oddo et al., 2018).

Figure 2.1 The location of the Mekong River Basin.

The MRB is located in the various physiographic regions, including the Tibetan Plateau, Three Rivers Area, Lacang Basin, Northern Highlands, Khorat Plateau, Tonle Sap Basin, and the Mekong Delta. The geographical distribution of high elevated mountainous area in the upstream of the MRB links to significant flood hazards in the LMB. Figure 2.2 shows the whole basin profile of elevation and upstream drainage area along with the distance from the headwaters to the river mouth in the Mekong Delta. The flow form the catchment area 24% of the total size in the Lancang River (Upper Mekong River in China and Myanmar) contributes to only 18% of the basin annual flow, of which Lao PDR, Thailand, Cambodia, and Vietnam drains 35%, 18%, 18%, and 11% (Table 2.1), respectively.

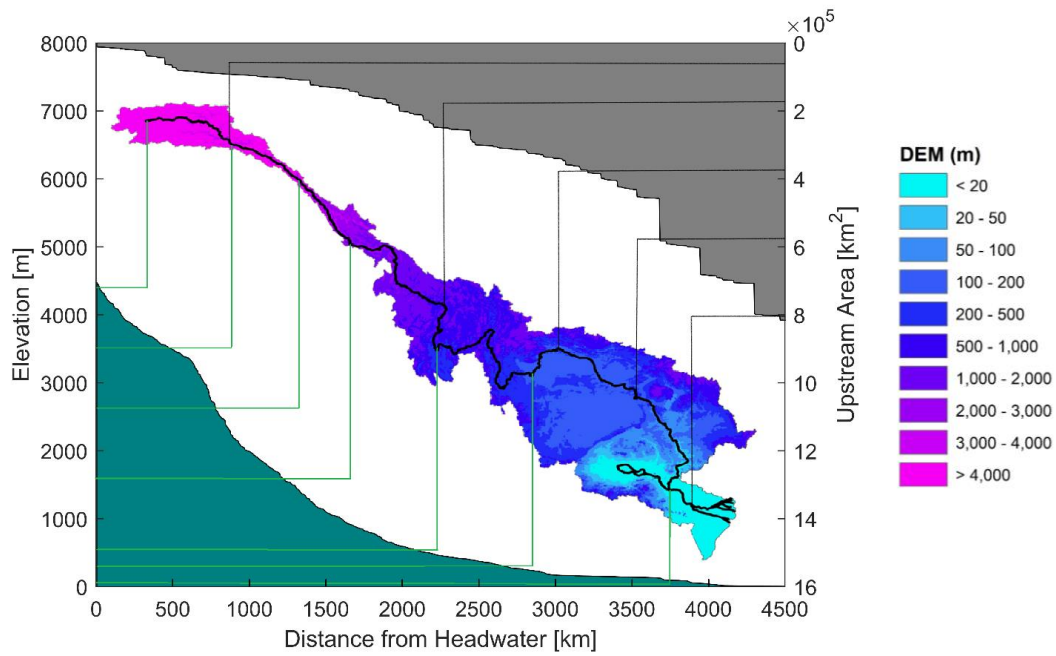

Figure 2.2 Longitudinal river profile of the Mekong River from the headwaters to the river mouth.

Table 2.1 The distribution of catchment size and flow of the MRB in each country.

Description	China	Myan-mar	Lao PDR	Thai-land	Cambo-dia	Viet-nam	Total MRB
Area ($\times$1000 km^2)	165	24	202	184	155	65	795
Catchment as % of MRB	21	3	25	23	20	8	100
Flow as % of MRB	16	2	35	18	18	11	100

2.1.2 The Tonle Sap Lake

The Tonle Sap Lake, the heart of the MRB, is the largest freshwater body in Southeast Asia located in the flood plain of Cambodia (Figure 2.3). This lake supports the people living in and around its floodplain (Kummu, 2009; Siev et al., 2018; Uk et al., 2018). The Tonle Sap River connects Phnom Penh, the intersection of the Mekong's mainstream, the Tonle Sap River, and the Bassac River, to the Tonle Sap Lake. The Tonle Sap Lake in the LMB has a unique hydrologic system of two-directional flows. In the dry season, the water flows from the Tonle Sap Lake to the Mekong River, while the water level of the river is higher than the water level in the lake causing the water flowing backward to the Tonle Sap Lake in the rainy season. The surface area of the lake expands from 2,600km^2 in the dry season to 12,000km^2 in the wet season resulting in the inundation from the floodplain (Oeurng et al., 2019).

The huge seasonal inundations during flood season are the predominant ecosystem driver as an interaction between the main lake and the Mekong River. This natural phenomenon maintains high productivity and biodiversity (Arias et al., 2013; Keskinen et al., 2013; Sarkkula et al., 2003; Uk et al., 2018). The floodplain of the Tonle Sap Lake can be categorized into five types: open water body, forest, seasonally flooded habitat, transitional habitat, and rain-fed habitat (Arias et al., 2012). More than one million people who are living on and around the Tonle Sap Lake are directly depending on its ecosystem services (Kummu et al., 2008).

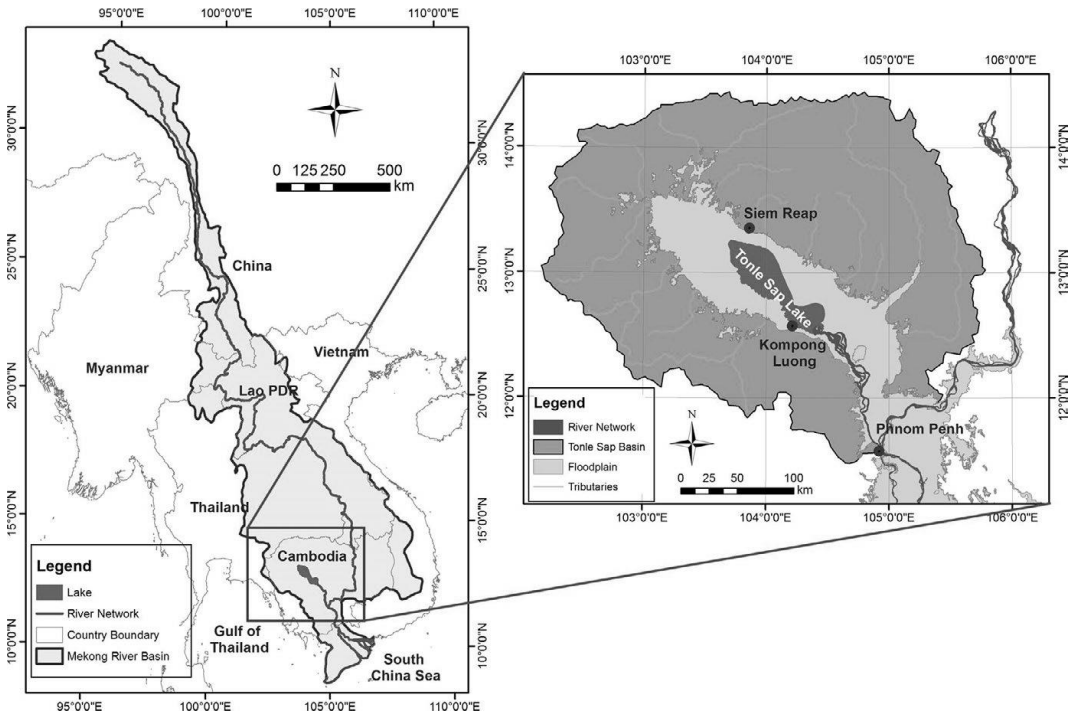

Figure 2.3 Location of the Tonle Sap Lake in the Lower Mekong Basin of Cambodia (Uk et al., 2018).

The Tonle Sap Lake and its floodplain are vulnerable to hydrological changes mainly due to the development of water infrastructure (Arias et al., 2012; Baran et al., 2001; Johnstone et al., 2013; Kite, 2001; Lamverts, 2008; Lamberts and Koponen, 2008; Uk et al., 2018), climate change effect (Burnett et al., 2013; Chadwick et al., 2008; Hoang et al., 2016; Johnstone et al., 2013; Keskinen et al., 2013), water quality degradation (Chea et al., 2016; Sarkkula et al., 2003), and land use/land cover change (Senevirathne et al., 2010). The natural resources and biodiversity are prone to be affected by altering the hydrological cycle in the Tonle Sap Lake the Mekong river systems (Arias et al., 2012; Uk et al., 2018).

2.1.3 Flood Situation in the Mekong Region

Flood has become one of the most widespread and frequent natural disasters causing losses of people's lives and properties (Yilmaz et al., 2010). There were 8,835 global disasters from 1970 to 2012, accounting for 1.94 million deaths and US$ 2.4 trillion in economic damages (WMO, 2014). In the Lower Mekong Basin, the average annual cost of floods is between US$ 60 and 70 million (MRC, 2010). Figures 2.4 and 2.5 illustrate the flood economic damage and the number of flood events in the Mekong sub-region (i.e. Cambodia, China, Lao PDR, Myanmar, Thailand, and Vietnam). These figures were plotted based on the EM-DAT database (http://www.emdat.be/database). Both flood economic damages and the number of flood events significantly increased from 1984 to 2017. The increase of flood economic damages might be due to the country's economic development. Try et al. (2018a) found a significant increase in satellite nightlight values, representing the economic activities from 1992 to 2013 in the Mekong region. In addition, the escalation of extreme flood events in the MRB might be mainly caused by climate change effects (Lauri et al., 2012; Perera et al., 2017; Try et al., 2020a; 2020b; Västilä et al., 2010).

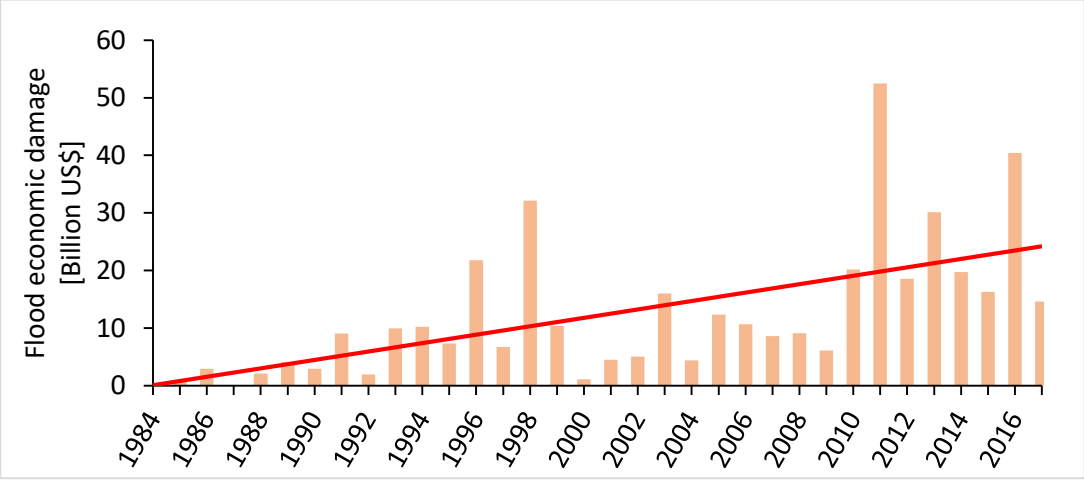

Figure 2.4 Flood economic damages of the greater Mekong sub-region. The data was retrieved from EM-DAT database.

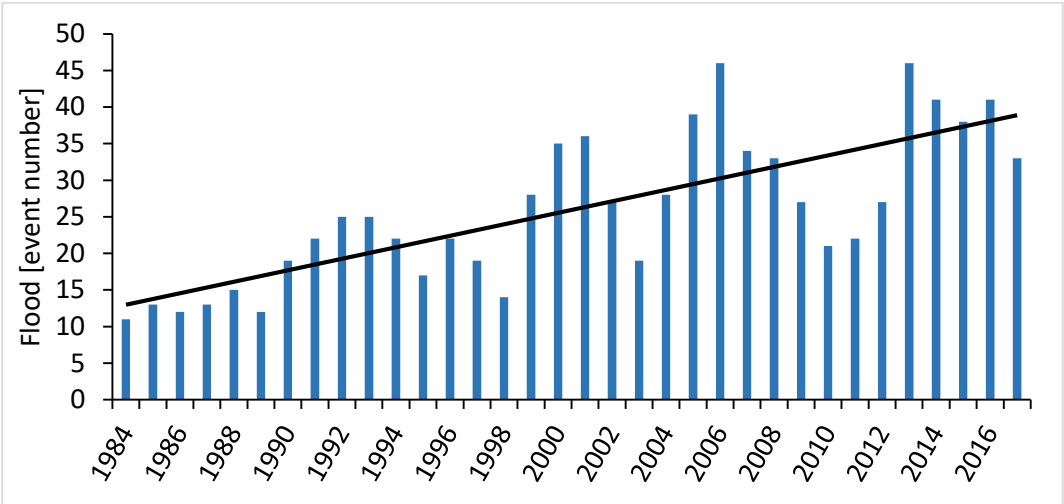

Figure 2.5 Flood event number in the greater Mekong sub-region. The data was retrieved from EM-DAT database.

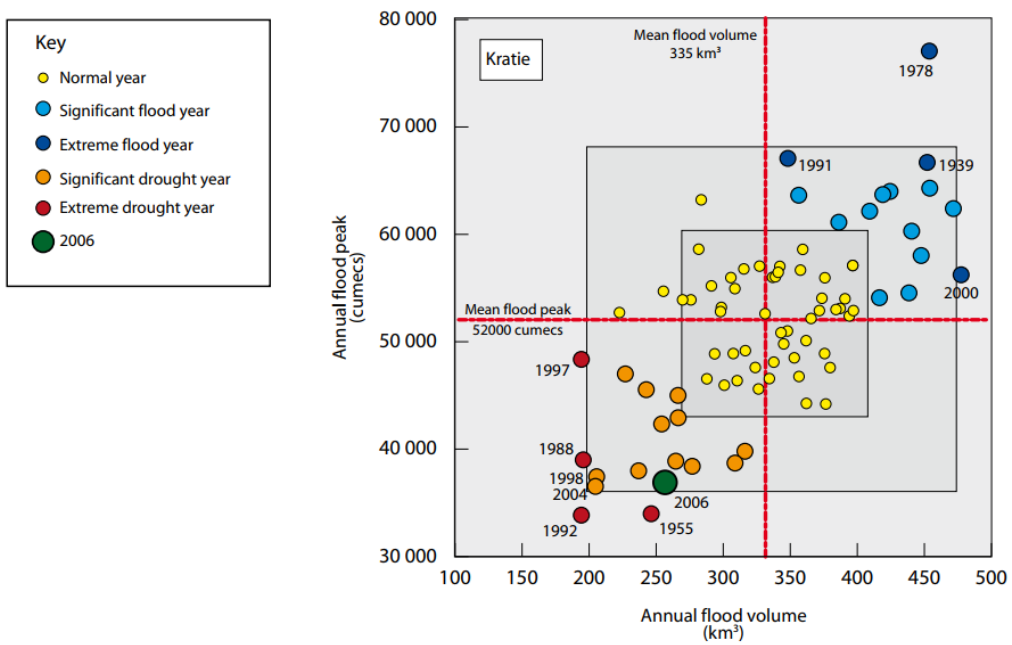

Figure 2.6 Scatter plots of the distribution of annual maximum flood discharge and the volume of the annual flood hydrograph at Kratie between 1924 and 2006. The darker boxes indicate one and two standard deviations for each variable above and below their respective means (MRC, 2007).

The mean annual peak discharge and mean annual flood volume flowing through Kratie station for 83 years (1924–2006) were 52,000 m^3/s and 335 km^3 with standard deviations of 8,300 m^3/s and 70 km^3 respectively. Figures 2.6 and 2.7 provide significant insight into historical floods in the Mekong River. The 2000 flood covered the inundated area of 45,000 km^2 in the Tonle Sap floodplain and the Mekong Delta. This extreme flood event killed more than 800 people (MRC, 2005) and caused economic damages of more than US$ 282 million (MRC, 2014). It was the most extreme flood event in terms of flood volume of approximately 480 km^3 at Kratie while its annual peak discharge was only marginally above the average. The estimated recurrence interval of exceptionally high flood volume of 2000 flood lay between 20 and 50 years in Figure 2.7.

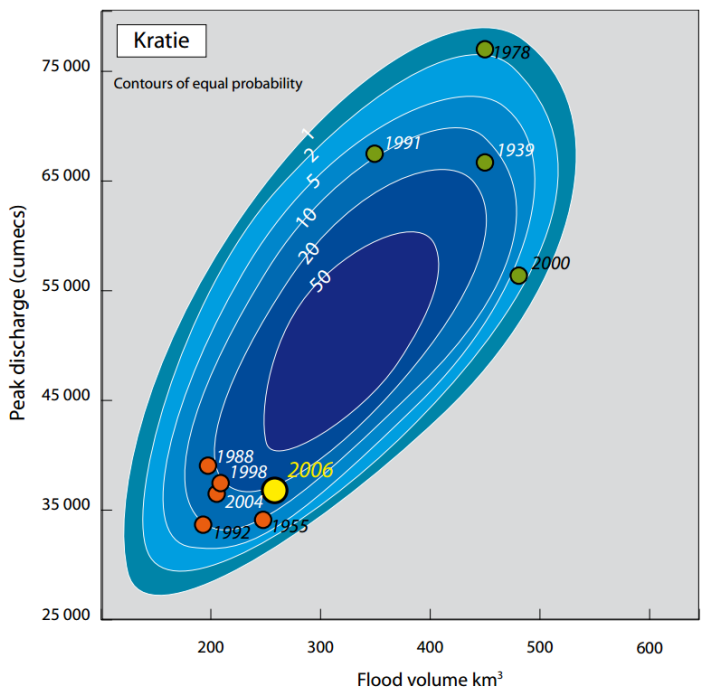

Figure 2.7 The statistical distribution of the annual flood peak and volume at Kratie. The points located outside the 1% line correspond to a recurrence interval in excess of 1:100 year; the points located outside the 2% line have a recurrence interval greater than 50 years, and so forth (MRC, 2007).

The application of a distributed rainfall-runoff-inundation (RRI, Sayama et al., 2015a; 2015b) model and a Time-Space Accounting Scheme (T-SAS, Sayama and McDonnel, 2009) is able to track and identify the source of flow from the spatial zone of the upstream area. Their application to the MRB during a large historical flood event in 2011 indicated that the Upper Mekong Basin from China and Myanmar (pink), northern Lao PDR (blue), southern Lao PDR and eastern Thailand (green), and floodplain of the MRB in Cambodia and Vietnam (red) contributed by 18%, 28%, 39%, and 15% to flow at Kratie; and 16%, 25%, 35%, and 24% to the total basin flow (Figure 2.8).

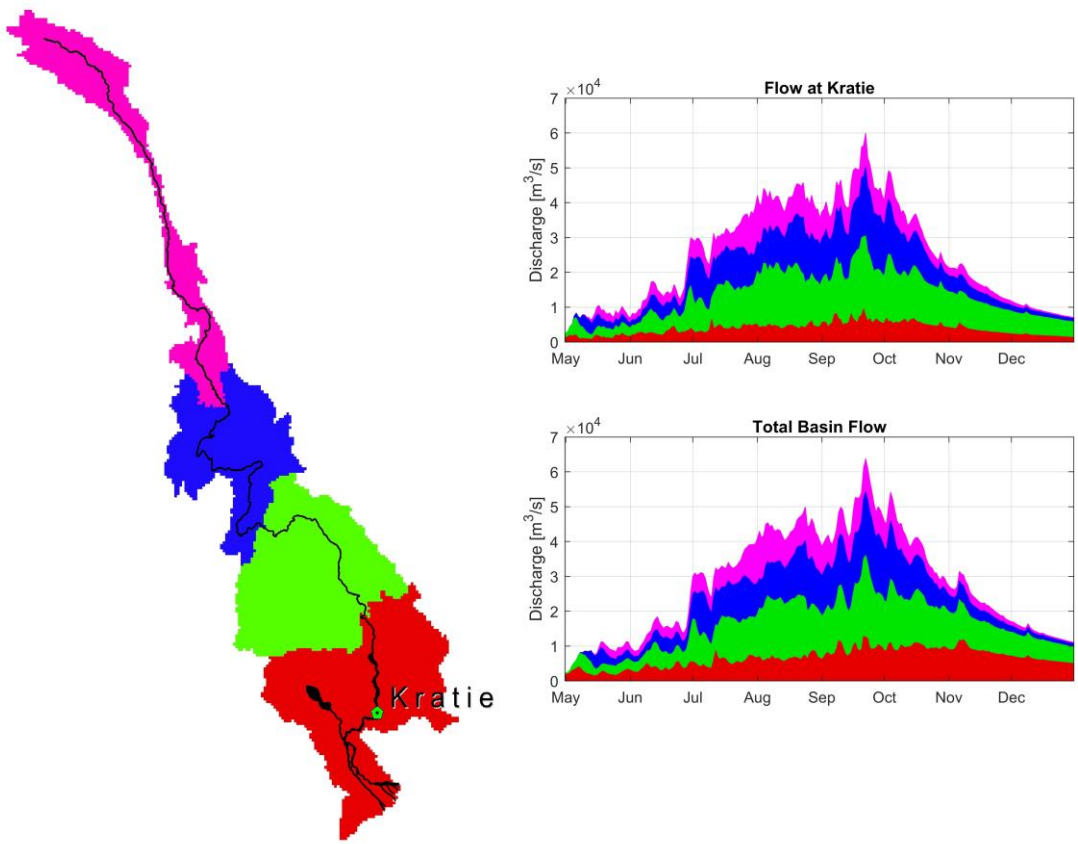

Figure 2.8 Hydrograph separation for spatial zone from the upstream of the MRB for 2011 flood event. The color represents the spatial zone identities which are the sources of flow at Kratie and the total basin.

2.1.4 Climate of the Mekong Basin

The climate in the Mekong River Basin is dominantly covered by tropical monsoon with a seasonal change between the rainy season (May – October) and dry season (November – April) period (MRC, 2005). The south-west monsoon brings heavy rains and high humidity from mid-May to early October, and drier and cooler air (lower temperature) is from north-east from early November to March (Table 2.2). Tropical cyclones occur in most areas of the basin in the wettest periods in August, September, and early October. In the Upper Mekong Basin, there is a similar monsoon climate with the LMB in Yunnan province of China, even though the topographic conditions are considerable variation. However, the climate changes from tropical and subtropical monsoons in the southern Yunnan to temperate monsoon in the headwaters at the elevation of approximately 4,500 above mean sea level (m.a.s.l.) in the Tibetan Plateau.

Table 2.2 Seasonal climate in the Mekong River Basin.

Cool/Cold		Hot/Dry		Wet						Cool/Cold	
Jan	Feb	Mar	Apr	May	Jun	Jul	Aug	Sep	Oct	Nov	Dec
NE Monsoon		Transition		SW Monsoon						NE Monsoon	

Figure 2.9 shows the spatial distribution of average annual precipitation for the entire Mekong region from Asian Precipitation Highly-Resolved Observational Data Integration Towards Evaluation of Water Resources (APHRODITE) (Yasutomi et al., 2011; Yatagai et al., 2012). In general, the annual precipitation in the LMB is much higher compared to the Upper Mekong Basin (Lancang River) in Myanmar and China. The map clearly indicates the high precipitation Lao PDR while the low precipitation was observed in the Plateau in Thailand comparing to the other parts in the LMB. According to the gauged observation, the annual basin average precipitation in the entire MRB is approximately 1,480 mm (Try et al., 2020c). In the Upper Mekong Basin, the precipitation is quite a little amount comparing to the LMB. For instance, the annual precipitation at Deqen in the Tibetan Plateau is only around 600 mm. Snow is rare in the valleys of the Upper Mekong, but it is more significant in the higher altitudes and the source of water in the dry season and spring (April and May) for the flow in the mainstream of the Lancang River.

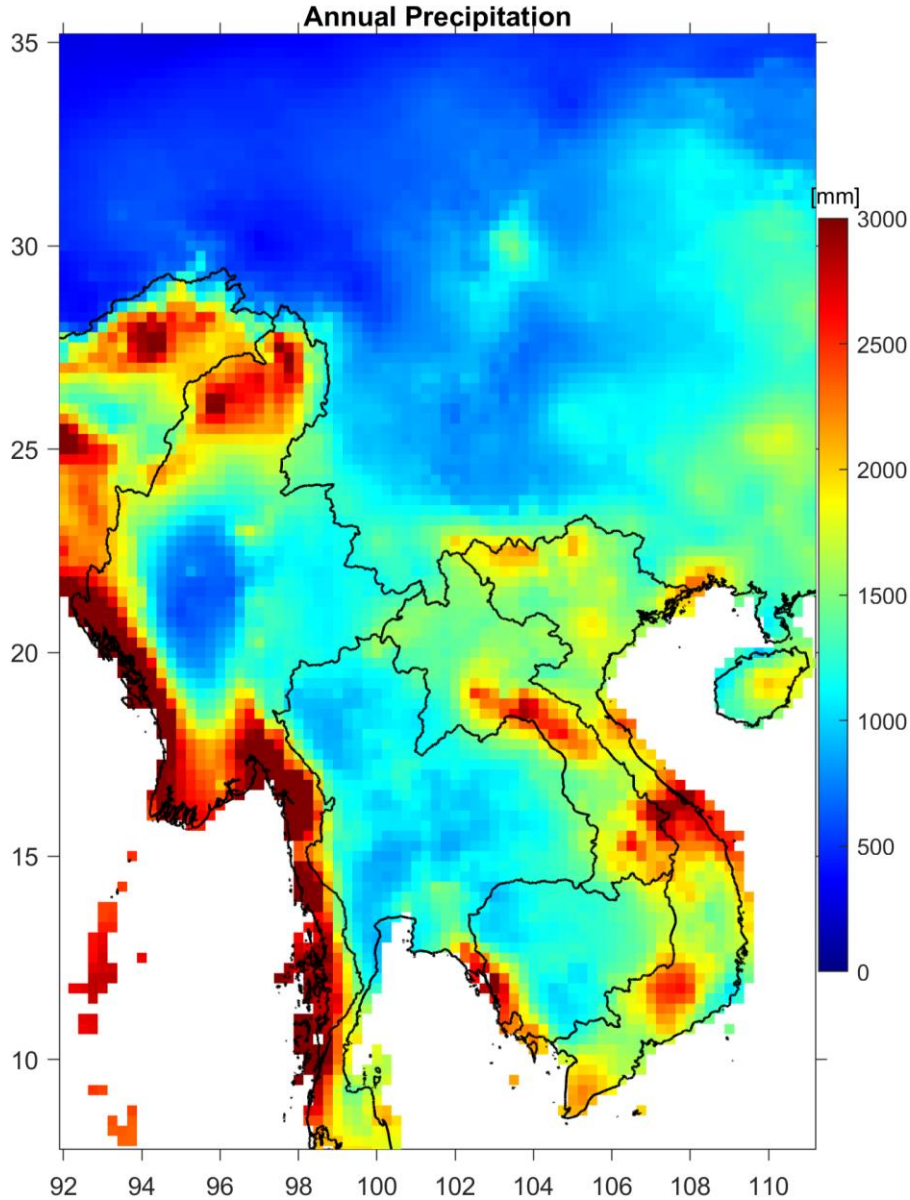

Figure 2.9 Annual precipitation from APHRODITE dataset.

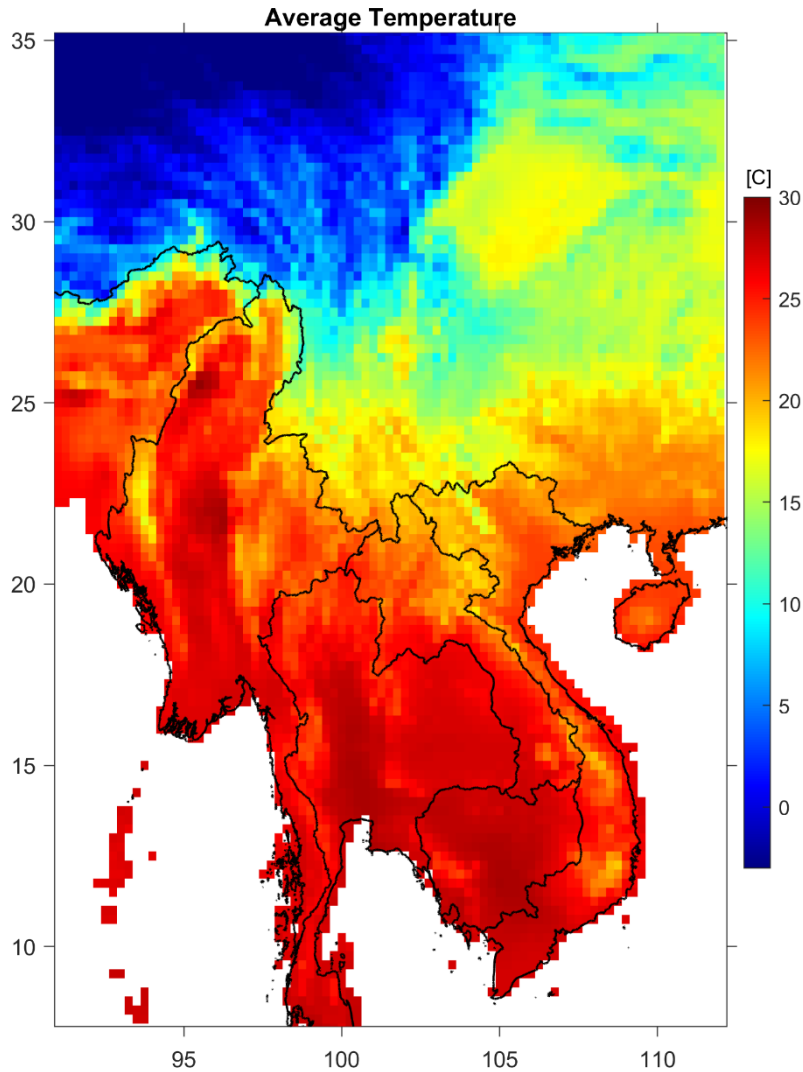

Figure 2.10 Average temperature from APHRODITE dataset.

The seasonal range of mean temperature in the lowlands and river valleys of the LMB is not relatively large. However, there are significant changes between the dry and rainy seasons and from day to night (MRC, 2005). Mean summer temperatures from March to October are similarly within the LMB from Phnom Penh in Cambodia (28 – 30°C) to Luang Prabang (26 – 28°C) in Lao PDR and Chiang Rai (26 – 29°C) in Thailand (MRC, 2005). Figure 2.10 shows the average distribution of temperature for the entire MRB from the APHRODITE dataset (Yasutomi et al., 2011). At the high elevation area in the Upper Se

San in Vietnam with 2,500 m.a.s.l., the temperature is only 2 – 3°C lower than the lowlands. Winter mean temperatures decrease to 26 – 27°C in Phnom Penh and 21 – 23°C in Chiang Rai (MRC, 2005). The temperature is cooler in the Upper Basin in Yunnan, China. The average temperatures at Jinhong station are lower than temperatures in Chiang Rain only 2 – 3°C in summer and 5 – 6°C in winter. At the high elevation of 4,000 m.a.s.l. in the Plateau of Tibet in Deqen, the temperatures can reach below zero in winter and 13°C in summer.

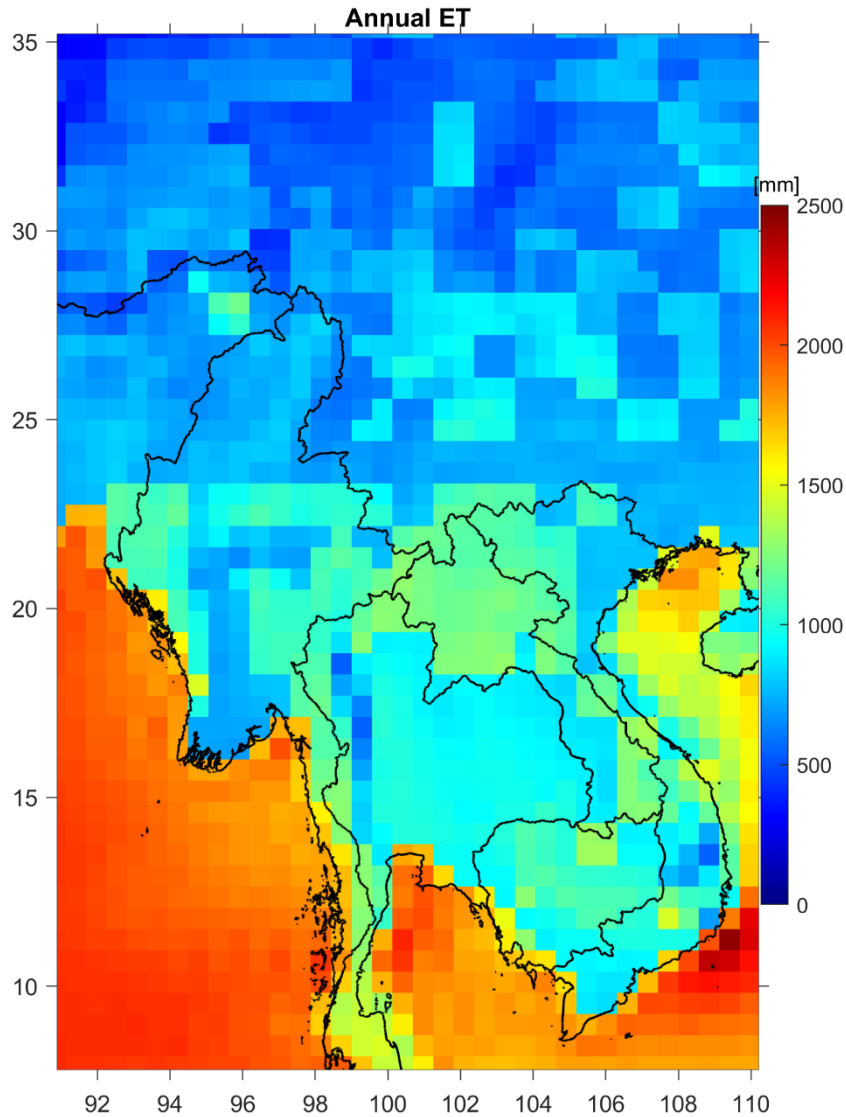

Figure 2.11 Annual evapotranspiration (ET) from JRA-55 dataset.

The annual rates of evapotranspiration in the MRB vary with little variability from year to year but high relative humidity. The Korat Plateau in north-east Thailand is one of the driest in the region. For example, the observed mean annual rainfall at Khon Kaen is about 1,200 mm comparing to the annual rate of evapotranspiration of up to 1,900 mm (MRC, 2005). Generally, within the LMB, the evapotranspiration rate does not reach below 1000 mm. The evapotranspiration in the Upper Basin in Yunnan is much lower than the LMB due to lower temperature and large variation of altitude and slope. Figure 2.11 displays the distribution of evapotranspiration extracted from the Japanese 55-year Reanalysis (JRA-55) dataset (Kobayashi et al., 2015).

2.2 Rainfall-Runoff-Inundation Model

2.2.1 Model Overview

This study used the Rainfall-Runoff-Inundation (RRI) model which is a 2D distributed model capable of simulating rainfall-runoff and flood inundation simultaneously (Sayama et al., 2012). The model has been applied in various basins to simulate large-scale flooding, to conduct hazard mapping and real-time inundation prediction. It is also used to elucidate flooding characteristics as well as to assess flood risk at a river basin scale (Bhagabati and Kawasaki, 2017; Kuribayashi et al., 2016; Perera et al., 2017; Sayama et al., 2015a; 2015b; Try el at., 2020a; 2020b; 2020c).

At the stream network cell level, the model assumes that both river channel and surrounding slopes are located in the same grid. The model slope grid cells receive rainfall and flow based on the 2D diffusive wave equations, while the in-channel flow is calculated with the 1D diffusive equations. The RRI model simulation deals with surface and subsurface flow in the mountainous area and the Green-Ampt infiltration method in the floodplain separately. The flow interaction between the river channel and the slope is computed at a running time step interval based on different overflowing formulae, which depends on water-level and levee-height conditions. The RRI model provides the output of river discharge, river water level, inundation extent, and inundation depth at the same time. The

model was integrated into the global optimization algorithm of the Shuffled Complex Evolution (SCE-UA) tool (Duan et al., 1994) for calibration of its sensitive parameters.

Rainfall-Runoff-Inundation (RRI) model is a two-dimensional distributed model dealing with slopes and river channels separately (Sayama et al., 2012; Sayama et al., 2015a; 2015b). The RRI model calculates flow on slopes and rivers based on 2D and 1D diffusive wave equations which are able to consider reversed flow (Figure 2.12). At the river grid cell, the model considers slope and river are located in the same grid cell. To represent the rainfall-runoff-inundation processes, the RRI model simulates lateral subsurface flow, vertical infiltration, and surface flow. The lateral surface flow is important for mountainous regions accounting for saturated subsurface and surface flows (Figure 2.13.a). The vertical infiltration flow is calculated by the Green-Ampt model (Figure 2.13.b). The flow interaction between slope and river channel depends on differences in water level and levee-height.

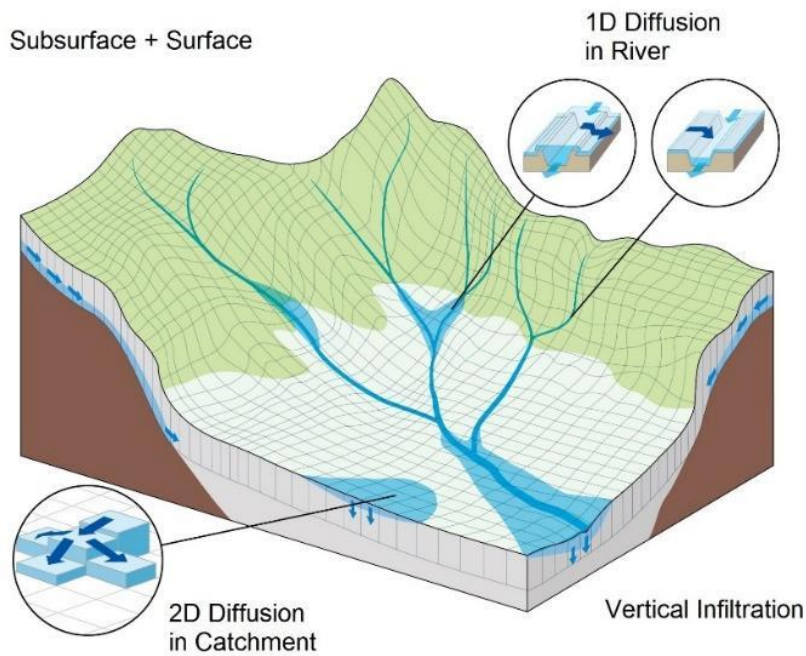

Figure 2.12 Schematic diagram of the RRI model (Sayama et al., 2015a).

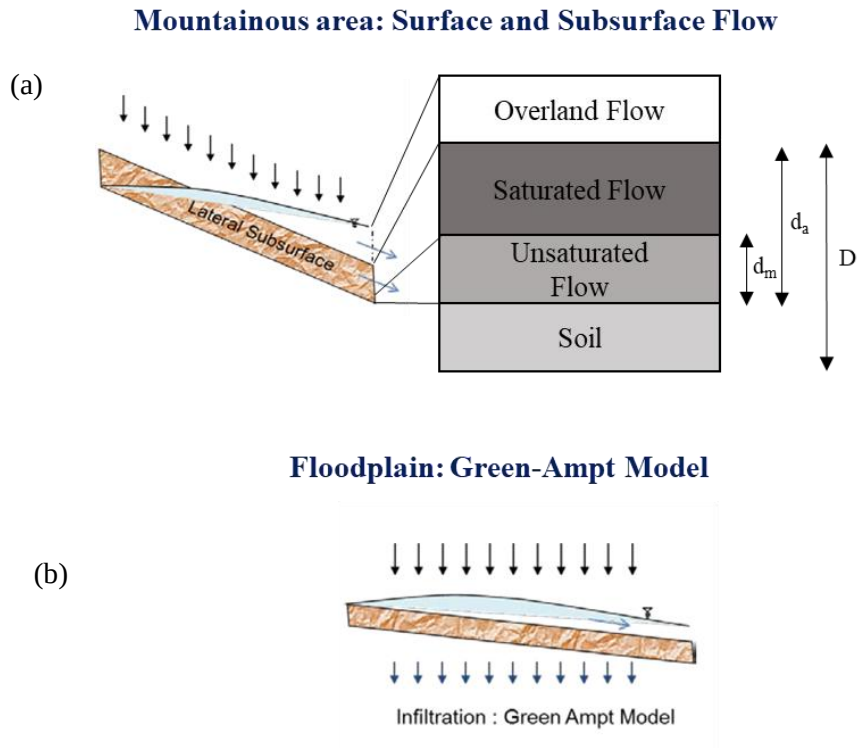

Figure 2.13 Graphical representation of (a) surface and subsurface flow for hill slope region and (b) Green-Ampt infiltration model for floodplain

The RRI model has been widely used for different purposes in various study areas, confirming its good performance and ability to simulate flood inundation. For instance, the RRI model was used to study the characteristics of the 2011 flood (Sayama et al., 2015a) and hydrologic sensitivity of rainfall-runoff and inundation (Sayama et al., 2015b) in the Chao Phraya River Basin, Thailand. Try et al. (2018b) used the RRI model for reproducing a historical large flood event in 2000 in the MRB, and Try et al. (2020a) evaluated the performance of satellite-based precipitation products. Perera et al. (2017) and Try et al. (2020b) used the RRI model to evaluate the effects of climate change in the LMB by considering various Representative Concentration Pathways (RCPs) and sea surface temperature (SST) scenarios. Moreover, Try et al. (2020c) used the RRI model for the projection of extreme flood inundation events in the MRB. Additionally, the RRI model has been successfully applied in other river basins, including Nyaungdon Area (Khaing et

al., 2019) and Bogo River Basin (Bhagabati and Kawasaki, 2017) in Myanmar, Solo River Basin (Kudo et al., 2016) and Batanghari River Basin (Yamamoto et al., 2020) in Indonesia, Kabul River Basin in Afghanistan (Sayama et al., 2012), Kalu and Mundeni River Basins in Sri Lanka (Rasmy et al., 2019), Kelantan River Basin in Malaysia (Chong et al., 2017), and several other river basins in Japan (Sayama et al., 2019).

2.2.2 Model Structure

A storage cell-based inundation model is used to calculate lateral flow in grid cells (Hunter et al., 2007). The governing equations of the RRI model are derived according to the following mass balance equation (2.1) and momentum equation (2.2) and (2.3) for gradually varied unsteady flow.

$$\frac{\partial h}{\partial t} + \frac{\partial q_x}{\partial x} + \frac{\partial q_y}{\partial y} = r - f \tag{2.1}$$

$$\frac{\partial q_x}{\partial t} + \frac{\partial u q_x}{\partial x} + \frac{\partial v q_y}{\partial y} = -gh\frac{\partial H}{\partial x} - \frac{\tau_x}{\rho_w} \tag{2.2}$$

$$\frac{\partial q_y}{\partial t} + \frac{\partial u q_x}{\partial x} + \frac{\partial v q_y}{\partial y} = -gh\frac{\partial H}{\partial y} - \frac{\tau_y}{\rho_w} \tag{2.3}$$

where h is the height of the water from the local surface, q_x and q_y are the unit width discharges in x and y directions, u and v are the flow velocities in x and y directions, r is the rainfall intensity, H is the height of the water from the datum, ρ_w is the density of water, g is the gravitational acceleration, and τ_x and τ_y are the shear stresses in x and y directions. The second terms of the right-hand side of equations (2.2) and (2.3) are calculated with Manning's equation:

$$\frac{\tau_x}{\rho_w} = \frac{g n^2 u\sqrt{u^2 + v^2}}{h^{1/3}} \tag{2.4}$$

$$\frac{\tau_y}{\rho_w} = \frac{gn^2 v\sqrt{u^2+v^2}}{h^{1/3}} \tag{2.5}$$

where n is Manning's roughness parameter. According to the approximation of the diffusion wave approach, inertia terms (the left side terms of equations (2.2) and (2.3)) are neglected. On the other hand, by dividing x and y directions (i.e. u and v are neglected in equations (2.2) and (2.3)), we obtain as the following:

$$q_x = -\frac{1}{n}h^{5/3}\sqrt{\left|\frac{\partial H}{\partial x}\right|}\,\mathrm{sgn}\left(\frac{\partial H}{\partial x}\right) \tag{2.6}$$

$$q_y = -\frac{1}{n}h^{5/3}\sqrt{\left|\frac{\partial H}{\partial y}\right|}\,\mathrm{sgn}\left(\frac{\partial H}{\partial y}\right) \tag{2.7}$$

where sgn is the signum function.

The RRI model spatially discretized mass balance equation (2.1) as follows:

$$\frac{dh^{i,j}}{dt} + \frac{q_x^{i,j-1} - q_x^{i,j}}{\Delta x} + \frac{q_y^{i-1,j} - q_y^{i,j}}{\Delta y} = r^{i,j} - f^{i,j} \tag{2.8}$$

where $q_x^{i,j}$ and $q_y^{i,j}$ are x and y direction discharges from a grid cell at (i,j).

In this study, we considered the effect of unsaturated and saturated subsurface flow and surface flow with single variable of h (Sayama and McDonnell, 2009).

$$q_x = \begin{cases} -k_m d_m \left(\frac{h}{d_m}\right)^{\beta}\frac{\partial H}{\partial x}, & (h \le d_m) \\ -k_a(h-d_m)\frac{\partial H}{\partial x} - k_m d_m \frac{\partial H}{\partial x}, & (d_m < h \le d_a) \\ -\frac{1}{n}(h-d_a)^{\frac{5}{3}}\sqrt{\left|\frac{\partial H}{\partial x}\right|}\,\mathrm{sgn}\left(\frac{\partial H}{\partial x}\right) - k_a(h-d_m)\frac{\partial H}{\partial x} - k_m d_m \frac{\partial H}{\partial x}, & (d_a < h) \end{cases} \tag{2.9}$$

$$q_y = \begin{cases} -k_m d_m \left(\frac{h}{d_m}\right)^{\beta} \frac{\partial H}{\partial y}, & (h \le d_m) \\ -k_a (h - d_m) \frac{\partial H}{\partial y} - k_m d_m \frac{\partial H}{\partial x}, & (d_m < h \le d_a) \\ -\frac{1}{n}(h - d_a)^{\frac{5}{3}} \sqrt{\left|\frac{\partial H}{\partial y}\right|} \operatorname{sgn}\left(\frac{\partial H}{\partial y}\right) - k_a (h - d_m) \frac{\partial H}{\partial y} - k_m d_m \frac{\partial H}{\partial y}, & (d_a < h) \end{cases} \quad (2.10)$$

where:

- k_a is the hydraulic conductivity of the lateral saturated soil layer
- k_m *is un*saturated hydraulic conductivity ($k_m = k_a/\beta$)
- d_m is the soil depth of unsaturated layer
- d_a is the total soil depth of the effective porosity.

Infiltration loss can be calculated using the Green-Ampt infiltration model (Rawls et al., 1992) as shown in the following equation:

$$f = k_v \left[1 + \frac{(\phi - \theta_i) S_f}{F}\right] \quad (2.11)$$

where k_v is the vertical saturated hydraulic conductivity, ϕ is the soil porosity, θ_i is the initial water content, S_f is the suction at the vertical wetting front, and F is the cumulative infiltration depth.

The RRI model calculates stream flow at river grid cells with one-dimensional diffusive wave. The river geometry is assumed to be rectangle, whose shapes are noted by width W (m) and depth D (m) as the following equations:

$$W = C_W A^{S_W} \quad (2.12)$$

$$D = C_D A^{S_D} \quad (2.13)$$

where C_W, S_W, C_D and S_D are river geometry parameters, and A is upstream contributing area (km^2).

2.2.3 Modeling Procedure

The procedure of RRI modeling is shown in Figure 2.14. The required input datasets are precipitation, topography (digital elevation model, flow direction, and flow accumulation), land use, evapotranspiration (ET), and river geometry. The RRI model was integrated with a global optimization called shuffled complex evolution developed at the University of Arizona (SCE-UA, Duan et al., 1994) to calibrate the sensitive parameters. The SCE-UA algorithm continues adjusting the values of parameters until obtaining the satisfactory results by comparing with observed river discharge and satellite-based inundation extent. After that, the calibrated RRI model will be used to simulate another period of flood inundation performance by reserving the same parameter values. The RRI model provides the outputs as river discharge, river water level, flood extents, and inundation depths.

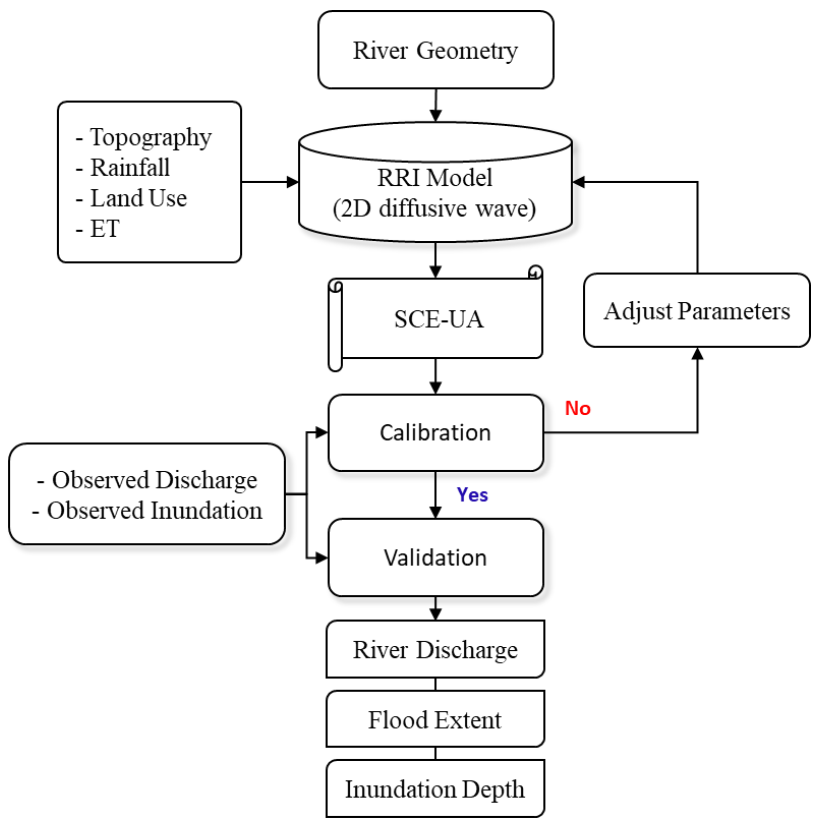

Figure 2.14 Integration of RRI model with SCE-UA Optimization.

The SCE-UA optimization algorithm (Duan et al., 1992; 1993; 1994) is an effective and efficient technique for calibration of a non-linear hydrological model. This computer-based automatic algorithm has been widely used by numerous researchers (Gan and Biftu, 1996; Lee et al., 2006; 2007; Kim et al., 2008; Lee and Kang, 2015; Try et al., 2018b; 2020a), and it has been found to be a practical method influenced by the choice of parameters. The concepts of this approach follow three of the following: (1) the combination of the simplex procedure by applying a controlled random searching approach; (2) competitive evolution; and (3) complex shuffling (Figure 2.15. This automatic calibration aims to search for the proper values of the parameters of the RRI model by optimizing the value of the objective function. More detail of the algorithm of SCE-UA is available in Appendix B.

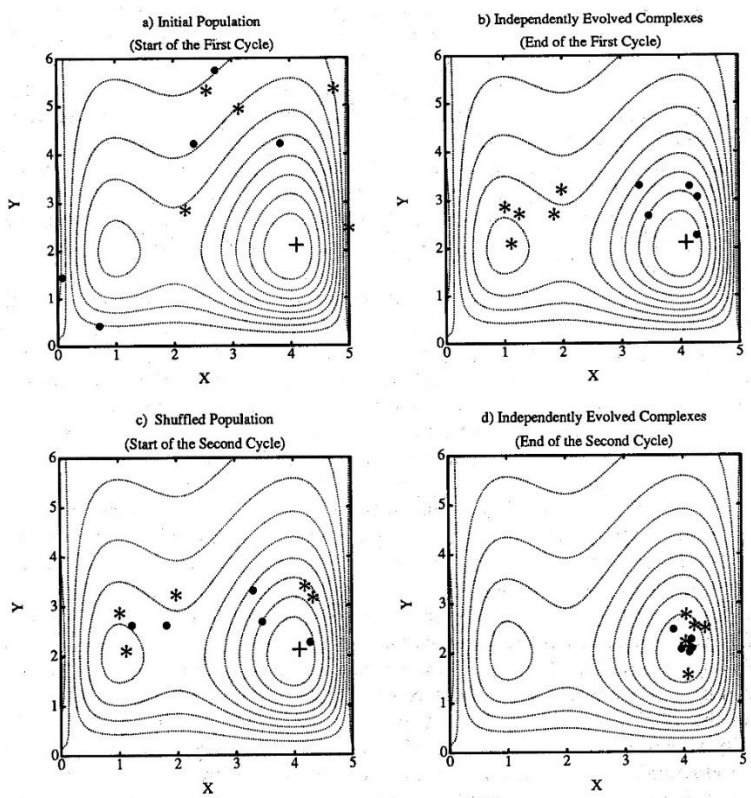

Figure 2.15 Illustration of Shuffled complex evolution (SCE-UA) method (Duan et al., 1994).

2.3 Summary

This chapter presented the study area of the Mekong River Basin, the focused area for this thesis. The basic information of the hydrological system, flood characteristics, and climate condition were introduced. On the other hand, the rainfall-runoff-inundation (RRI) model, a two-dimensional diffusive wave model, was described in details of its governing equation and simulation characteristics and. The RRI model was used as the main hydrological tool and flood inundation modeling in this thesis by integrating with a global optimization algorithm SCE-UA for the calibration of sensitive parameters. Chapter 3 used the RRI model for comparison of the performance of gridded precipitation for flood inundation modeling in the MRB. Chapter 4 employed the RRI model for the future projection of extreme flood inundation in the MRB using a large ensemble climate dataset under 4 K increasing scenario. Chapter 5 applied the RRI model with a high- and super-high-resolution climate dataset to evaluate the effects of climate change under different sea surface temperature (SST) and RCP scenarios. Finally, Chapter 6 utilized the RRI model to compare the performance of the most recent CMIP6 models with the previous CMIP5 models.

References

Arias, M. E., Cochrane, T. A., Piman, T., Kummu, M., Caruso, B. S., and Killeen, T. J. (2012). Quantifying changes in flooding and habitats in the Tonle Sap Lake (Cambodia) caused by water infrastructure development and climate change in the Mekong Basin. *Journal of Environmental Management*, *112*, 53–66. doi: 10.1016/j.jenvman.2012.07.003.

Arias, M. E., Cochrane, T. A., Norton, D., Killeen, T. J., and Khon, P. (2013). The flood pulse as the underlying driver of vegetation in the largest wetland and fishery of the mekong basin. *Ambio*, *42*(7), 864–876. doi: 10.1007/s13280-013-0424-4.

Baran, E., Van Zalinge, N., and Bun, N. P. (2001). Floods, floodplains and fish production in the Mekong Basin: Present and past trends, pp. 920–932. In A. Ali, et al. (Eds.), *Second Asian Wetlands symposium* (p. 1166). Pulau Pinang, Malaysia: Penerbit Universiti Sains Malaysia.

Bhagabati, S. S. and Kawasaki, A., (2017). Consideration of the rainfall-runoff-inundation (RRI) model for flood mapping in a deltaic area of Myanmar. *Hydrological Research Letters*, *11*(3), pp.155-160. doi: 10.3178/hrl.11.155.

Burnett, W., Wattayakorn, G., Kum, V., and Sioudom, K. (2013). Assessing the impact of climate change and development pressures on nutrient inputs into the Mekong River and Tonle Sap, FL, USA.

Chadwick, M., Juntopas, M., and Sithirth, M. (2008). Sustaining Tonle Sap: An assessment of development challenges facing the great lake (pp. 6–9). Bangkok, Thailand: The Sustainable Mekong Research Network (Summernet).

Chea, R., Grenouillet, G., and Lek, S. (2016). Evidence of water quality degradation in Lower Mekong Basin revealed by self-organizing map. *PLoS ONE*, *11*(1), 1–19. doi: 10.1371/journal.pone.0145527.

Chong, K. L., Sayama, T., Takara, K., and Abustan, I. (2017). Effects of Diffusive Wave and Flood Inundation on Time of Concentration. *Journal of Japan Society of Civil Engineers (Hydraulic Engineering)*, 73(4), pp.I_151-I_156. doi: 10.2208/jscejhe.73.I_151.

Duan, Q., Sorooshian, S., and Gupta, V. K. (1992), Effective and efficient global optimization for conceptual rainfall-runoff models. *Water Resources Research* 28(4), 1015-1031. doi: 10.1029/91WR02985.

Duan, Q., Gupta, V. K., and Sorooshian, S. (1993), Shuffled complex evolution approach for effective and efficient global minimization, *Journal of Optimization Theory and Application*, 76(3), 501-521.

Duan, Q., Sorooshian, S., and Gupta, V. K., (1994). Optimal use of the SCE-UA global optimization method for calibrating watershed models. *J. Hydrology*, 158 (3–4): 265–284. doi: 10.1016/0022 -1694(94)90057-4

Gan, T. Y., and Biftu, G. F. (1996). Automatic calibration of conceptual rainfall-runoff models: Optimization algorithms, catchment conditions, and model structure. *Water resources research*, 32(12), 3513-3524. doi: 10.1029/95WR02195.

Hoang, L. P., Lauri, H., Kummu, M., Koponen, J., Vliet, M. T. H. V., Supit, I., Rik, L., Pavel, K., and Ludwig, F. (2016). Mekong River flow and hydrological extremes under climate change. *Hydrology and Earth System Sciences*, *20*(7), 3027–3041. doi: 10.5194/hess-20-3027-2016.

Hunter, N. M., Bates, P. D., Horritt, M. S., and Wilson, M. D. (2007). Simple spatially-distributed models for predicting flood inundation: a review. *Geomorphology*, 90(3), 208-225. doi: 10.1016/j.geomorph.2006.10.021.

Johnstone, G., Puskur, R., Declerck, F., Mam, K., Il, O., Mak, S., Pech S., Seak S., Chan, S., and Hak, S. (2013). Tonle Sap Scoping Report. CGIAR Research Program on Aquatic Agricultural Systems. Penang, Malaysia. Project Report: AAS-2013-28.

Keskinen, M., Kummu, M., Salmivaara, A., Someth, P., Lauri, H., Moel, D. H., Ward, P., and Sokhem, P. (2013). *Tonle Sap now and in the future?* Final Report of the Exploring Tonle Sap Futures Study, Aalto University and 100Gen Ltd. with Hatfield Consultants Partnership, VU University Amsterdam, EIA Ltd. and Institute of Technology of Cambodia, in partnership with Tonle Sap Authority and Supreme National Economic Council. Water & Development Publications WD-11, Aalto University, Espoo, Finland.

Khaing, Z.M., Zhang, K., Sawano, H., Shrestha, B.B., Sayama, T., and Nakamura, K., (2019). Flood hazard mapping and assessment in data-scarce Nyaungdon area, Myanmar. *PloS One*, 14(11), p.e0224558. doi: 10.1371/journal.pone.0224558.

Kim, S., Tachikawa, Y., Lee, G., and Takara, K. (2008). Prediction of the largest ever flood: case study on typhoon Rusa in 2002 at the Gamcheon basin, Korea. *Proceedings of Hydraulic Engineering*, 52, 67-72.

Kite, G. (2001). Modelling the Mekong: Hydrological simulation for environmental impact studies. *Journal of Hydrology*, *253*(1–4), 1–13. doi: 10.1016/S0022-1694(01)00396-1.

Kobayashi, S., Ota, Y., Harada, Y., Ebita, A., Moriya, M., Onoda, H., Onogi, K., Kamahori, H., Kobayashi, C., Endo, H., Miyaoka, K., and Takahashi, K. (2015) The JRA-55 reanalysis: general specifications and basic characteristics. *J. Meteor. Soc. Japan*, 93:5–48. doi: 10.2151/jmsj.2015-001.

Kudo, S., Sayama, T., Hasegawa, A., and Iwami, A. (2016). Analysis of flood risk change in future climate in terms of discharge and inundation in the Solo River Basin. *Proceedings of the 7th International Conference on Water Resources and Environment Research—ICWRER.*

Kummu, M., Sarkkula, J., Koponen, J., and Nikula, J. (2006). Ecosystem management of the Tonle Sap Lake: an integrated modelling approach. *International Journal of Water Resources Development*, 22(3): 497-519. doi: 10.1080/07900620500482915.

Kummu, M., Penny, D., Sarkkula, J., and Koponen, J. (2008). Sediment: Curse or blessing for Tonle Sap Lake? *Ambio*, *37*(3), 158–163. doi: 10.1579/0044-7447(2008)37[158:SCOBFT]2.0.CO;2

Kummu M. (2009) Water management in Angkor: Human impacts on hydrology and sediment transportation. . *J. Environ. Manage*; 90, 1413–1421.

Kuribayashi, D., Ohara, M., Sayama, T., Konja, A., and Sawano, H. (2016). Utilization of the flood simulation model for disaster management of local government. *Journal of Disaster Research, 11*(6), pp.1161-1175. doi: 10.20965/jdr.2016.p1161.

Lamberts, D. (2008). Little impact, much damage; the consequences of Mekong River flow alterations for the Tonle Sap ecosystem. In M. Kummu, M. Keskinen, & O. Varis (Eds.), *Modern myths of the Mekong* (pp. 3–18). Helsinki, Finland: Helsinki University of Technology.

Lamberts, D., and Koponen, J. (2008). Flood pulse alterations and productivity of the Tonle Sap ecosystem: a model for impact assessment. AMBIO: A Journal of the Human Environment 37(3): 178-184. doi: 10.1579/0044-7447(2008)37[178:FPAAPO]2.0.CO;2.

Lauri, H., Moel, H.D., Ward, P., Räsänen, T., Keskinen, M., and Kummu, M. (2012). Future changes in Mekong River hydrology: impact of climate change and reservoir operation on discharge. *Hydrol Earth Syst Sci*, 16:4603–4619. doi: 10.5194/hess-16-4603-2012.

Lee, G., Tachikawa, Y., and Takara, K. (2006). Analysis of hydrologic model parameter characteristics using automatic global optimization method. *Annuals of Disaster Prevention Research Institute*, 67-80.

Lee, G., Tachikawa, Y., and Takara, K. (2007). Identification of model structural stability through comparison of hydrologic models. *Proceedings of Hydraulic Engineering*, 51, 49-54.

Lee, S., and Kang, T. (2015). Analysis of Constrained Optimization Problems by the SCEUA with an Adaptive Penalty Function. *Journal of Computing in Civil Engineering*, 30(3), 04015035. doi: 10.1061/(ASCE)CP.1943-5487.0000493.

MRC, (2005). Overview of the Hydrology of the Mekong Basin vol. 82. Mekong River Commission, Vientiane, Lao PDR.

MRC, (2007). Annual Mekong flood report 2006. Mekong River Commission, Vientiane, Lao PDR.

MRC, (2010). State of the Basin Report 2010, Mekong River Commission, Vientiane, Lao PDR.

MRC, (2011). Planning atlas of the lower Mekong river basin, Mekong River Commission. Vientiane, Laos PDR.

MRC, (2014). Annual Mekong Flood Report 2011. Mekong River Commission, Vientiane, Lao PDR.

Oddo, P., Ahamed, A., and Bolten, J. (2018). Socioeconomic Impact Evaluation for Near Real-Time Flood Detection in the Lower Mekong River Basin. *Hydrology*, 5(2), 23. doi: 10.3390/hydrology5020023

Oeurng, C., Thomas A. C., Chung, S., Mathias G. K., Piman, T., and Mauricio E. A. (2019). Assessing climate change impacts on river flows in the Tonle Sap Lake Basin, Cambodia. *Water*, 11, no. 3: 618. doi: 10.3390/w11030618.

Perera, E., Sayama, T., Magome, J., Hasegawa, A., and Iwami, Y. (2017). RCP8.5-based future flood hazard analysis for the lower Mekong river basin. *Hydrology*, 4(4):55. doi: 10.3390/hydrology4040055.

Rasmy, M., Sayama, T., and Koike, T., (2019). Development of water and energy Budget-based Rainfall-Runoff-Inundation model (WEB-RRI) and its verification in the Kalu

and Mundeni River Basins, Sri Lanka. *Journal of Hydrology, 579,* p.124163. doi: 10.1016/j.jhydrol.2019.124163.

Rawls, W. J., Ahuja, L. R., Brakensiek, D. L., Shirmohammadi, A., and Maidment, D. (1992). Infiltration and soil water movement: McGraw-Hill Inc.

Sarkkula, J., Kiirikki, M., Koponen, J., and Kummu, M. (2003). Ecosystem processes of the Tonle Sap Lake. In 1st Workshop of Ecotone Phase II. Phnom Penh, Cambodia (pp. 1–14).

Senevirathne, N., Mony, K., Samarakoon, L., and Hazarika, M. K. (2010). Land use/land cover change detection of Tonle Sap Watershed, Cambodia. In 31st Asian Conference on Remote Sensing 2010, ACRS 2010 (pp. 852–857).

Sayama, T., and McDonnell, J. J. (2009). A new time-space accounting scheme to predict stream water residence time and hydrograph source components at the watershed scale. *Water resources research,* 45(7). doi: 10.1029/2008WR007549.

Sayama, T., Ozawa, G., Kawakami, T., Nabesaka, S., and Fukami, K. (2012). Rainfall-Runoff-Inundation analysis of the 2010 Pakistan flood in the Kabul River basin, *Hydrological Science Journal*, 57(2), 298-312. doi: 10.1080/02626667.2011.644245.

Sayama, T., Tatebe, Y., and Tanaka, S. (2015a). An emergency response-type rainfall-runoff inundation simulation for 2011 Thailand floods, *Journal of Flood Risk Management*, 1-8. doi: 10.1111/jfr3.12147.

Sayama, T., Tatebe, Y., Iwami, Y., and Tanaka, S. (2015b). Hydrologic sensitivity of flood runoff and inundation: 2011 Thailand floods in the Chao Phraya River basin, *Nat. Hazards Earth Syst. Sci.*, 15, pp. 1617-1630, doi: 10.5194/nhess-15-1617-2015.

Sayama, T., Matsumoto, K., Kuwano, Y. and Takara, K., (2019). Application of Backpack-Mounted Mobile Mapping System and Rainfall–Runoff–Inundation Model for Flash Flood Analysis. *Water*, *11*(5), p.963. doi: 10.3390/w11050963.

Siev, S., Heejun, Y., Sok, T., Uk, S., Song, L., Dilini K, Oeurng, C., Hul, S., Yoshimura, C. (2018). Sediment Dynamics in a Large Shallow Lake Characterized by Seasonal Flood Pulse in Southeast Asia. *Science of the Total Environment*. 631: 597–607. doi: 10.1016/j.scitotenv.2018.03.066.

Try, S., Lee, D., and Lee, G. (2018a). Application of nightlight satellite imagery for assessing flooding potential area in the Mekong river basin. *J. Korea Warer Resour. Assoc*. 51(7), 565-574. doi: 10.3741/JKWRA.2018.51.7.565.

Try, S., Lee, G., Yu, W., Oeurng, C., and Jang, C. (2018b). Large-Scale Flood-Inundation Modeling in the Mekong River Basin. *Journal of Hydrologic Engineering*, 23 (7). doi: 10.1061/(ASCE) HE.1943-5584.0001664.

Try, S., Lee, G., Yu, W., and Oeurng, C. (2019). Delineation of flood-prone areas using geomorphological approach in the Mekong River Basin. *Quaternary International*, 503, 79-86. doi: 10.1016/j.quaint.2018.06.026.

Try, S., Tanaka, S., Tanaka, K., Sayama, T., Lee, G., and Oeurng, C. (2020a). Assessing the effects of climate change on flood inundation in the Lower Mekong Basin using high-resolution AGCM outputs. *Progress in Earth and Planetary Science.* doi: 10.1186/s40645-020-00353-z.

Try, S., Tanaka, S., Tanaka, K., Sayama, T., Hu, M., Sok, T., and Oeurng, C. (2020b). Projection of extreme flood inundation in the Mekong River Basin under 4 K increasing scenario using large ensemble climate data. *Hydrological Processes*. doi: 10.1002/hyp.13859.

Try, S., Tanaka, S., Tanaka, K., Sayama, T., Oeurng, C., Uk, S., Takara, K., Hu, M., and Han, D., (2020c). Comparison of gridded precipitation datasets for rainfall-runoff and inundation modeling in the Mekong River Basin. *Plos ONE*, 15(1), p.e0226814. doi: 10.1371/journal.pone.0226814.

Uk, S., Yoshimura, C., Siev, S., Try, S., Yang, H., Oeurng, C., Li, S., and Hul, S. (2018). Tonle Sap Lake: Current Status and Important Research Directions for Environmental Management. *Lakes & Reservoirs*. 23(3): 177-189. doi: 10.1111/lre.12222.

Varis, O., Kummu, M., and Salmivaara, A. (2012). Ten major rivers in monsoon Asia-Pacific: An assessment of vulnerability. Applied Geography, 32(2), 441-454. doi: 10.1016/j.apgeog.2011.05.003.

Västilä, K., Kummu, M., Sangmanee, C., and Chinvanno, S. (2010). Modelling climate change impacts on the flood pulse in the lower Mekong floodplains. *J. Water Climate Change*, 1(1):67–86. doi: 10.2166/wcc.2010.008.

WMO, (2014). Atlas of Mortality and Economic Losses from weather, Climate and Water Extremes (1970-2012) (Vol. WMO-No.1123): World Meteorological Organization.

Yamamoto, E.M.S., Sayama, T., and Yamamoto, K., (2020). Comparison of runoff generation methods for land use impact assessment using the SWAT model in humid tropics. *Hydrological Research Letters*, *14*(2), pp.81-88. doi: 10.3178/hrl.14.81.

Yasutomi, N., Hamada, A., and Yatagai, A. (2011): Development of a long-term daily gridded temperature dataset and its application to rain/snow discrimination of daily precipitation. *Global Environmental Research*, V15N2, 165-172.

Yatagai, A., Kamiguchi, K., Arakawa, O., Hamada, A., Yasutomi, N., and Kitoh, A. (2012). APHRODITE: Constructing a Long-term Daily Gridded Precipitation Dataset for Asia based on a Dense Network of Rain Gauges, *Bulletin of American Meteorological Society*. doi: 10.1175/BAMS-D-11-00122.1.

Yilmaz, K. K., Adler, R. F., Tian, Y., Hong, Y., and Pierce, H. F. (2010). Evaluation of a satellite-based global flood monitoring system. *International Journal of Remote Sensing*, *31*(14), 3763-3782. doi: 10.1080/01431161.2010.483489.

CHAPTER 3: Comparison of gridded precipitation datasets for rainfall-runoff and inundation modeling in the Mekong River Basin

3.1 Introduction

Annual flooding is an important hydrological characteristic of the Mekong River Basin (MRB), especially in the Lower Mekong River (LMB) in which flooding is a way of life. On the one hand, prolonged floods challenge the survival and sustainability of the local community, causing huge socio-economic damages. The annual average cost of the flood damages in the LMB ranges between 60 and 70 million USD (MRC, 2011; Try et al., 2018a). The flood in 2011 caused more than 430 million USD and the death toll reached 396 (MRC, 2015). On the other hand, flooding drives the high productivity of the ecosystem and biodiversity in the downstream floodplains (Lu et al., 2014; Try et al., 2019). It is critically essential to understand the characteristics of the hydrological regime in the MRB for sustainable development and flood management.

Hydrological modeling is an effective approach to extrapolate and interpolate missing information over time and space between observations for hydrological assessment (Hu et al., 2019). Oeurng et al. (2019) studied the Tonle Sap sub-basin of MRB using the SWAT model. Try et al. (2018b) applied the RRI model for a single flood event in the LMB. Tanaka et al. (2018) investigated the flood characteristics in the Tonle Sap floodplain using an integrated hydrological-hydraulic model. However, the study of the hydrological regime over the whole MRB using a reliable model and related input is still lacking and needs to be fully addressed.

Precipitation is useful for understanding the mechanism of the hydrological system and is the most necessary input data in hydrological and hydraulic modeling (Hu et al., 2017). Therefore, accurate precipitation data is required for effective hydrological studies. The available ground precipitation data at the country level in the MRB is limited (Ono et al., 2013). Thus, it is necessary to evaluate the gridded rainfall products which are widely and freely available. To date, the evaluation of gridded precipitation has been conducted in several sub-basins of the MRB (Luo et al., 2019; Phoeurn and Ly, 2018; Thom et al., 2017). However, the performance evaluation of gridded precipitation for flood-inundation modeling in the whole MRB has not been reported yet.

Therefore, this study aims 1) to evaluate the performance of a rainfall-runoff-inundation model in the whole MRB for river discharge and flood inundation prediction; 2) to assess the performances of different gridded precipitation datasets in simulating the river discharge in the whole MRB and flood inundation in the LMB.

3.2 Methodology

3.2.1 Rainfall-Runoff-Inundation Model

This study used the Rainfall-Runoff-Inundation (RRI) with a spatial resolution of 2.5 arc minutes to understand the hydrological system for the whole MRB (Figure 3.1.a) and 1.5 arc minutes for the LMB (Figure 3.1.b) for more accurate inundation estimation. The time series of the river discharge at Stung Treng station was used as the boundary condition during the LMB simulation. The topography data including digital elevation model (DEM), flow direction (DIR), and flow accumulation (ACC) were obtained from the Multi-Error-Removed-Improved-Terrain (MERIT DEM) at the original resolution of 3 arc seconds (approx. 90 m at the equator) (Yamazaki et al., 2017). A topographic data scale-up algorithm in the RRI model was applied to transform the topography data to 1.5 and 2.5 arc minutes for LMB and MRB respectively. The land use data were obtained from the MODIS Land Cover Type Product (MCD12Q1) (Friedl et al., 2010). The surface evaporation was from the Japanese 55-year Reanalysis dataset (JRA-55) with a spatial resolution of 0.5625° and 3-hour temporal resolution (Kobayashi et al., 2015).

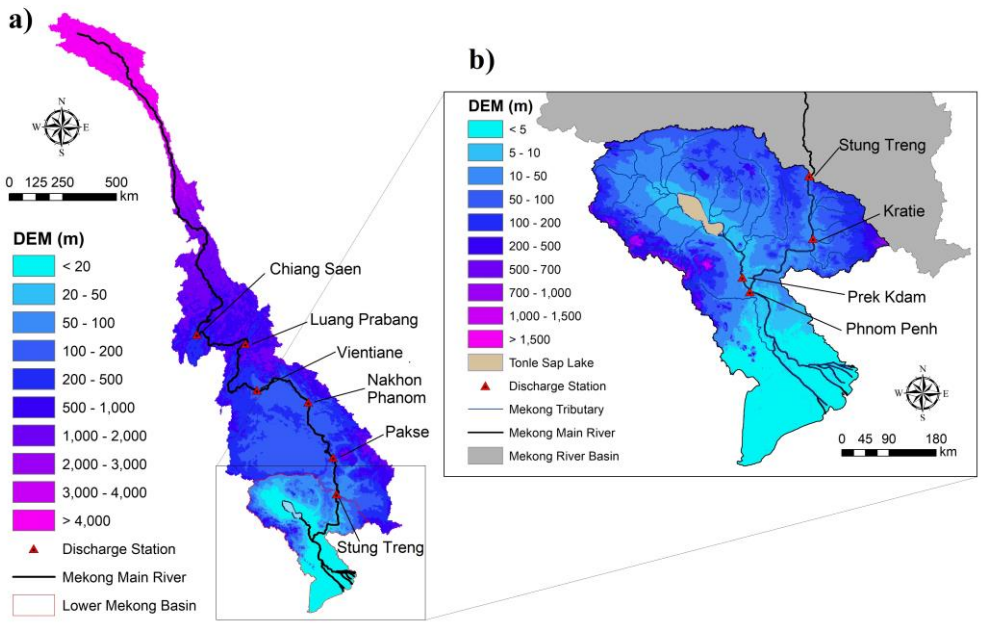

Figure 3.1 Location of the Mekong River Basin (a) and the Lower Mekong Basin (b) (Try et al., 2020).

3.2.2 Precipitation Datasets

This study used five gridded precipitation datasets including APHRODITE, GPCC, PERSIANN-CDR, GSMaP-RNL, and TRMM-3B42V7. Those datasets were chosen as a wide range of precipitation datasets at different spatial and temporal resolutions that should be explored for an informative assessment. Brief information on the gridded rainfall products used in this study is illustrated in Table 3.1. The basin average annual precipitation recorded by the rain gauge is 1,488 mm/year, APHRODITE 1,349 mm/year, GPCC 1,588 mm/year, PERSIANN-CDR 1,720 mm/year, GSMaP-RNL 1,145 mm/year, and TRMM-3B42V7 1,393 mm/year.

Table 3.1 Description of the gridded precipitation datasets used in this study.

Dataset	Version	Spatial/temporal resolution	Period	Source
APHRODITE	V1801R1	0.25°/daily	1998–2015	Yatagai et al. (2012)
GPCC	V.2018 (V2)	1°/daily	1982–2016	Ziese et al. (2018)
PERSIANN	CDR	0.25°/daily	1983–present	Ashouri et al. (2015)
GSMaP	RNL	0.1°/hourly	2000–present	Kubuta et al. (2007)
TRMM	3B42V7	0.25°/3-hourly	1998–present	Huffman et al. (2007)

3.2.2.1 APHRODITE dataset

The APHRODITE rainfall product is created by collecting and analyzing data from the gauged rainfall from 5,000–12,000 stations across Asia (Yasutomi et al., 2011). This product was produced by a joint project from the Research Institute for Humanity and Nature and Meteorological Research Institute covering 1951 to 2007 for Version V1101 and 1998-2015 for Version V1801R1. This study used APHRODITE Version V1801R1 with the daily temporal resolution and the spatial resolution of 0.25° (Yatagai et al., 2012).

3.2.4.2 GPCC dataset

The Global Precipitation Climatology Center (GPCC) Full Data Daily Version 2018 is based on the gauged precipitation from 67,200 stations worldwide provided by national meteorological and hydrological services, regional and global data collection organizations such as the World Meteorological Organization (Ziese et al., 2018). This product contains daily precipitation from 1982–2016 with the spatial resolution of 1° covering latitude: -90° to 90° and longitude: -180° to 180°.

3.2.4.3 PERSIANN dataset

Precipitation Estimation from Remotely Sensed Information using Artificial Neural Networks–Climate Data Record (PERSIANN-CDR) is developed by the Center for

Hydrometeorology and Remote Sensing measures rainfall using infrared (IR) brightness temperature data from geostationary satellites (Ashouri et al., 2015). The PERSIANN-CDR dataset is daily and 0.25° in space covering 60°S to 60°N from 1983 to the present.

3.2.4.4 TRMM dataset

The Tropical Rainfall Measuring Mission (TRMM) Multi-satellite Precipitation Analysis (TMPA) is a product resulting from the combination of precipitation from multiple satellites and rain gauges (Huffman et al., 2007). The data covers the latitude from 50°S to 50°N from 1998 to the present. TRMM 3B42 algorithm version 7 (TRMM-3B42V7) at fine spatial and temporal scales (0.25°×0.25° and 3-hourly) were used in this study.

3.2.4.5 GSMaP dataset

The Global Satellite Mapping of Precipitation (GSMaP) is derived from Precipitation Radar (PR), statistical classification, and scattering algorithms (Kubota et al., 2007). This study used GSMaP reanalysis version (GSMaP-RNL) precipitation available hourly from 2000 to date with a fine resolution of 0.1° covering 60°S to 60°N.

3.2.3 Evaluation Approach of Gridded Precipitation Datasets

The present study focused on the period from 2000 to 2007, due to the existence of the largest number of rainfall gauged stations and a few missing data during this period. The RRI model was calibrated and validated using the gauged rainfall during 2000–2007 as the gauged data from 2000 to 2007 used in this study showed good quality and density. Gauged rainfall has been commonly used for hydrological model calibration (Luo et al., 2019). Meanwhile, it is reported that model calibration using gridded data would produce unrealistic parameters (Thom et al., 2017; Habib et al., 2010). The calibrated model was used to simulate river flow and flood inundation using the gridded precipitation datasets. To evaluate the performance of streamflow simulation, we used three indicators including Nash-Sutcliffe model efficiency (NSE), coefficient of determination (R^2), and relative volume error (VE), as follows:

$$\mathrm{NSE} = 1 - \frac{\sum(Q_{sim}(t) - Q_{obs}(t))^2}{\sum(Q_{obs}(t) - \overline{Q_{obs}})^2} \quad (3.1)$$

$$\mathrm{R}^2 = \frac{\sum((Q_{sim}(t) - \overline{Q_{sim}})(Q_{obs}(t) - \overline{Q_{obs}}))^2}{\sum(Q_{sim}(t) - \overline{Q_{sim}})^2 \sum(Q_{obs}(t) - \overline{Q_{obs}})^2} \quad (3.2)$$

$$\mathrm{VE} = \frac{\sum Q_{sim}(t) - \sum Q_{obs}(t)}{\sum Q_{obs}(t)} \quad (3.3)$$

where $Q_{sim}(t)$ and $Q_{obs}(t)$ are the simulated and observed discharges at time step t, and $\overline{Q_{sim}}$ and $\overline{Q_{obs}}$ are the simulated and observed average discharges. To evaluate the performance of inundation simulation, we used three indices including true ratio (TR), hit ratio (HR), and normalized error (NE), as follows:

$$\mathrm{TR} = \frac{\mathrm{IC_{obs}} \cap \mathrm{IC_{sim}}}{\mathrm{IC_{sim}}} \quad (3.4)$$

$$\mathrm{HR} = \frac{\mathrm{IC_{obs}} \cap \mathrm{IC_{sim}}}{\mathrm{IA_{obs}}} \quad (3.5)$$

$$\mathrm{NE} = \frac{\mathrm{IC_{sim}} - \mathrm{IC_{obs}}}{\mathrm{IC_{obs}}} \quad (3.6)$$

where $\mathrm{IC_{sim}}$ and $\mathrm{IC_{obs}}$ are the number of inundated cells from the model simulation and MODIS observation data.

3.3 Result and Discussion

3.3.1 RRI Model Calibration and Validation

3.3.1.1 River Discharge

The model calibration and validation were carried out using the gauged precipitation between 2000–2003 and 2004–2007, respectively. The RRI model was calibrated using an

automatic global optimization algorithm called the Shuffled Complex Evolution (SCE-UA) at Stung Treng to evaluate the characteristics of the upstream area. Then, the daily discharge at this station was extracted as the input for the boundary condition to simulate the flood inundation performance at downstream of the Mekong River. The calibration was done using gauged rainfall with 500 simulations by changing the values of fives parameters: roughness coeficient for river (n_river), effective porosity (gamm_a), lateral saturated hydaulic conductivity (k_a), porosity for subsurface soil (gamma_m), and parameter for unsaturated hydraulic conductivity (β).

The comparison of the simulated and observed river discharges in Luang Prabang, Pakse, Stung Treng, and Prek Kdam is shown in Figure 3.2. It was found that there is a good agreement between the observation and simulation. The Stung Treng station provided the highest statistical performance indices with NSE = 0.94, R^2 = 0.94, VE = 0.05 in the calibration and NSE = 0.89, R^2 = 0.92, VE = 0.09 in the validation (Table 3.2). The statistics at Pakse were NSE = 0.90 and 0.89, R^2 = 0.94 and 0.91, VE = 0.14 and 0.09 during calibration and validation, respectively. For the upstream located areas at Luang Prabang, the evaluation indicators were NSE = 0.81, R^2 = 0.83 and -0.13 in the calibration and NSE = 0.77, R^2 = 0.78, VE = 0.06 in the validation. NSE and R^2 at Prek Kdam were 0.75 and 0.84 in the calibration and 0.69 and 0.77 in the validation. The coefficients of relative volume error VE = -0.27 and -0.31 in Prek Kdam were calculated by the assumption of the absolute value of inflow and outflow.

Table 3.2 Model performance of the river discharge evaluation at the gauging stations during calibration (2000–2003) and validation (2004–2007) periods.

Dataset		NSE	R^2	VE
Luang Prabang	Calibration	0.81	0.83	-0.13
	Validation	0.77	0.78	-0.06
Pakse	Calibration	0.90	0.94	0.14
	Validation	0.89	0.91	0.09

Stung Treng	Calibration	0.94	0.94	0.05
	Validation	0.89	0.92	0.09
Prek Kdam	Calibration	0.75	0.84	-0.27
	Validation	0.69	0.77	-0.31

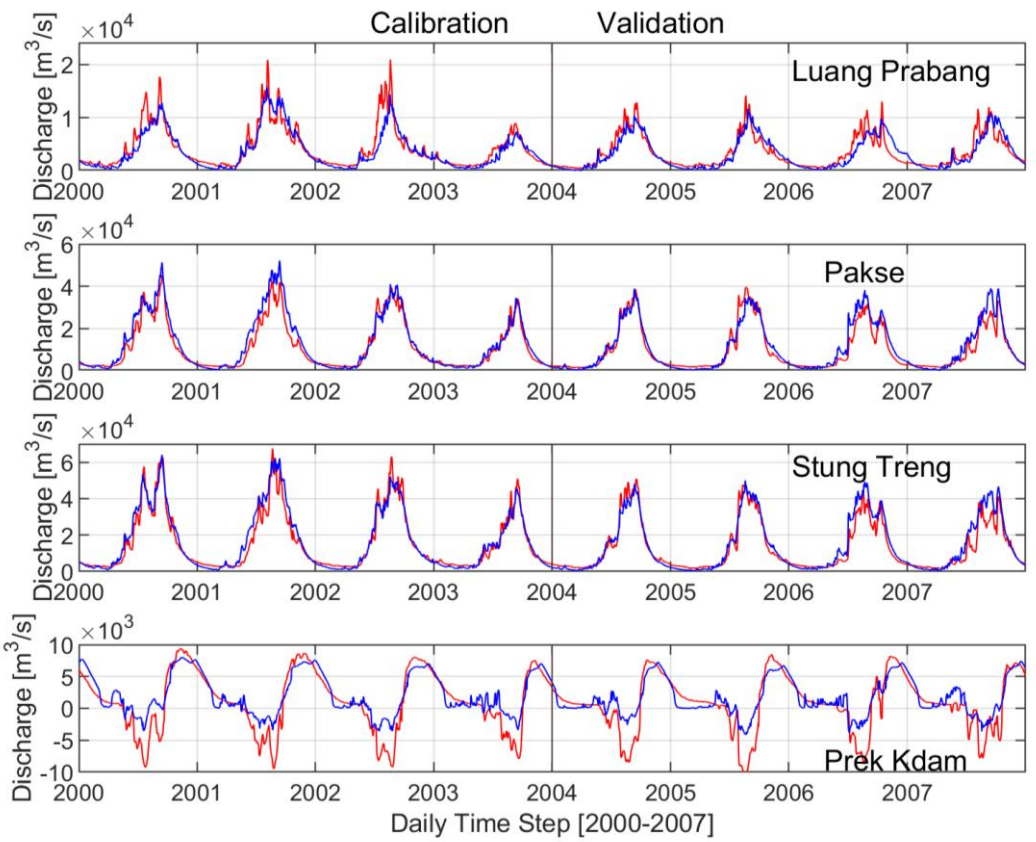

Figure 3.2 Simulated (blue) and observed (red) discharge during the calibration and validation periods at Luang Prabang (a), Pakse (b), Stung Treng (c), and Prek Kdam (d). (Note: The positive value at Prek Kdam represents the flow from Phnom Penh to the Tonle Sap Great Lake; the negative value indicates the reversed flow from the Tonle Sap lake to Phnom Penh).

3.3.1.2 Flood Inundation

For inundation estimation, the annual peak flood extent in the LMB during 2000–2007 was compared with the MODIS flood observation dataset (Figure 3.3). This study selected the

threshold value 0.5 m of water depth to distinguish between the flood and non-flood areas. Previous studies (Perera et al., 2017; Sayama et al., 2015a; 2015b; Try et al., 2018b; 2020) have chosen this threshold value since the water level is related to severe flood damage in the floodplain where the agricultural area is dominant land use type (Okada et al., 2011). According to the performance indices of the spatial inundation extent in Table 3.3, the RRI model simulated the flood extent with a good agreement of 84% accuracy (i.e. the hit ratio in 2000 was 0.84). On the other hand, the hit ratio in 2006 was 0.89 corresponding to the accuracy of 89% of the simulated inundation area. The average values are TR = 0.68, HR = 0.81, and NE = 0.23; and TR = 0.56, HR = 0.80, and NE = 0.43 during calibration (2000–2003) and validation (2004–2007) respectively. The flood inundation simulation in this study was better than the previous study by Sayama et al. (2015a) in Chao Phraya River Basin in terms of true ratio and hit ratio (i.e. their average values during 2005–2011 were TR = 0.41 and HR = 0.30). However, the normalized error value in the Chao Phraya case study was lower than that of this study (NE = -0.18).

Table 3.3 Model performance of the flood inundation extent compared with the remote sensing dataset.

	Year	IC_obs	IC_sim	IC_obs∩IC_sim	TR	HR	NE
Calibration	2000	5177	5011	4187	0.84	0.81	-0.03
	2001	4731	5610	3973	0.71	0.84	0.19
	2002	3860	4697	3257	0.69	0.84	0.22
	2003	2093	3280	1596	0.49	0.76	0.57
				Avg.	0.68	0.81	0.23
Validation	2004	2597	3307	1972	0.60	0.76	0.27
	2005	2204	2915	1590	0.55	0.72	0.32
	2006	2955	4562	2627	0.58	0.89	0.54
	2007	2526	3942	2125	0.54	0.84	0.56
				Avg.	0.56	0.80	0.43

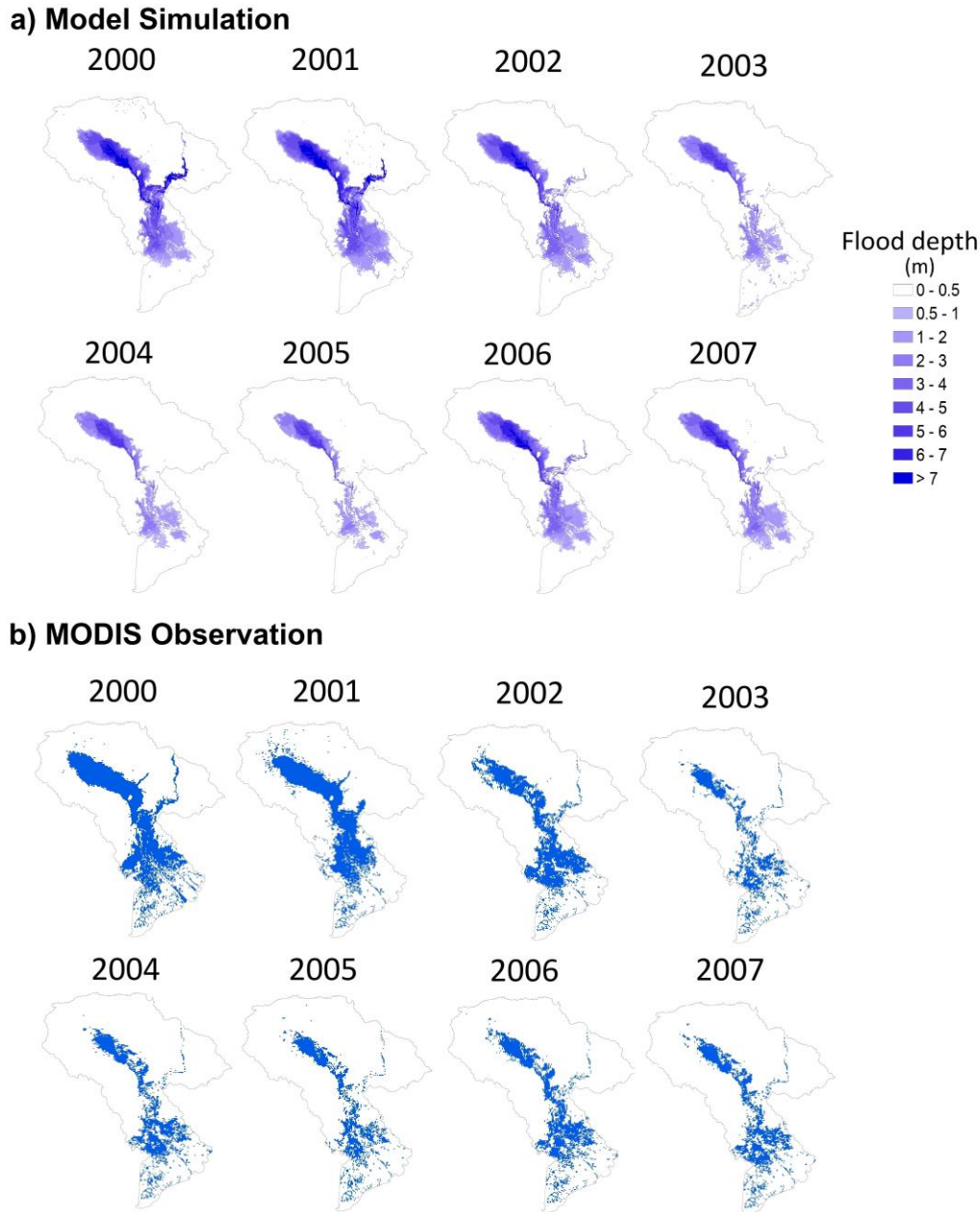

Figure 3.3 Model simulation and MODIS flood observation of the annual maximum flood extent from 2000 to 2007.

3.3.2 Performances of Gridded Precipitation Datasets

After model calibration and validation, the same parameter setting was used to simulate river discharge and flood inundation using the five gridded precipitation datasets during 2000–2007. Figure 3.4 illustrated the observed and simulated discharge from all the precipitation datasets at Stung Treng. The performance indices include NSE from 0.42 to 0.92; R^2 from 0.73 to 0.93; and VE from -0.46 to 0.21 (Table 3.4). The results of the river discharge indicated that APHRODITE, TRMM and GPCC datasets performed better with NSE =0.81, 0.85, 0.84; R^2 = 0.90, 0.89, 0.88; and VE = -0.19, 0.12, 0.13 at Stung Treng station followed by PERSIANN, and GSMaP. In addition, the extreme flow of the highest 5% of flow (Q_5) from the flow duration curve was evaluated (Figure 3.5). The ratio of Q_5 from the simulated discharges using the individual precipitation datasets were 1.00, 0.82, 1.09, 1.12, 0.53, 1.10 for rain-gauge, APHRODITE, GPCC, PERSIANN, GSMaP, and TRMM respectively.

Table 3.4 Performance indices for individual precipitation datasets.

Dataset	NSE	R^2	VE
Rain gauge	0.92	0.93	0.07
APHRODITE	0.81	0.90	-0.19
GPCC	0.84	0.88	0.13
PERSIANN	0.80	0.88	0.21
GSMaP	0.42	0.73	-0.46
TRMM	0.85	0.89	0.12

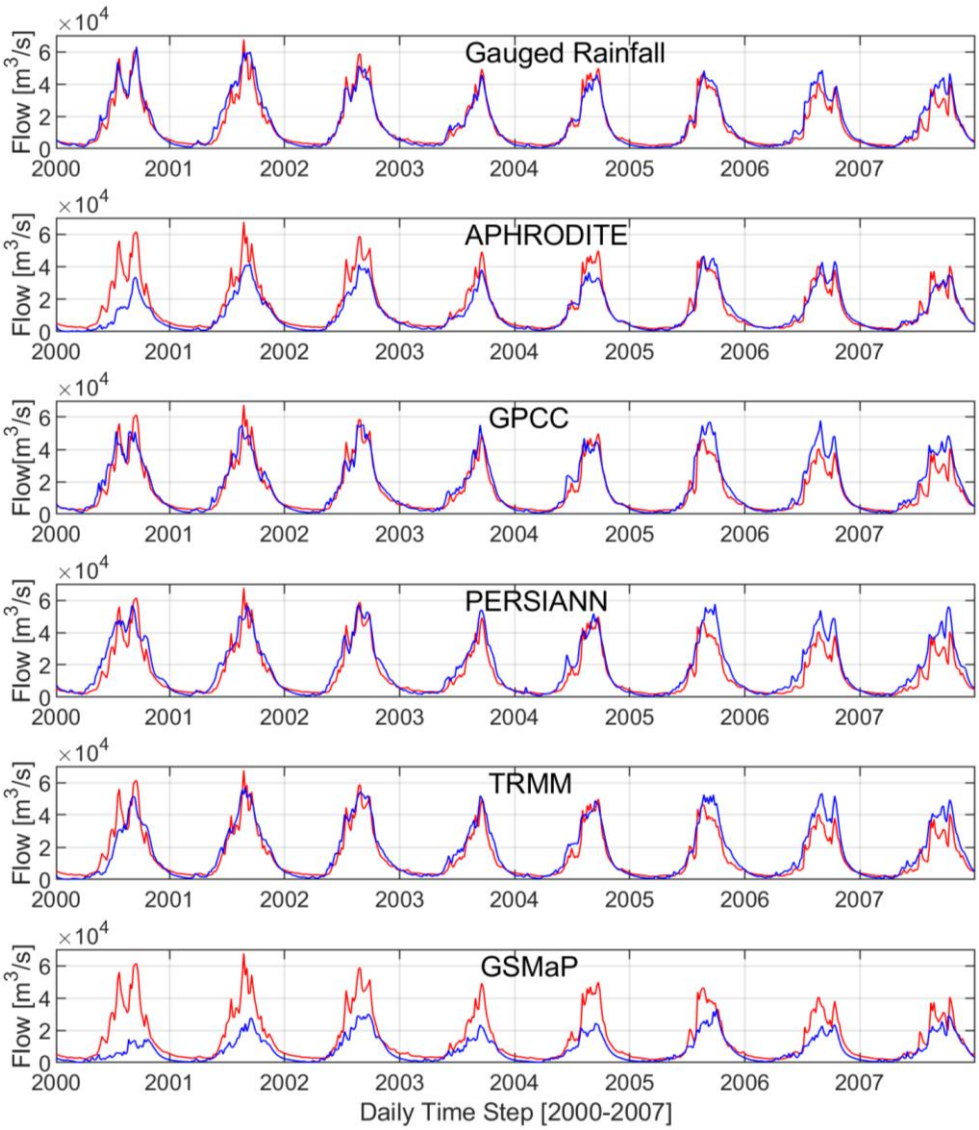

Figure 3.4 Observed (red) and simulated discharge (blue) from individual precipitation datasets at Stung Treng.

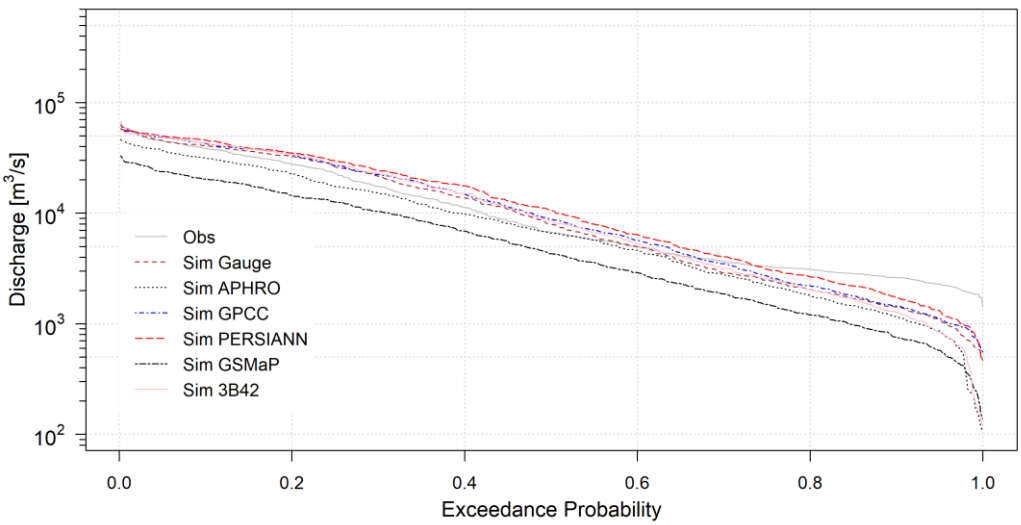

Figure 3.5 Flow Duration Curve of the simulated discharge.

The results of the average annual maximum flood extents in the simulation period (2000–2007) indicated that APHRODITE performed at the highest true ratio TR = 0.69 while the hit ratio indices of GPCC, PERSIANN, and TRMM were among the best (Table 3.5). The error indicators of APHRODITE and GSMaP were NE = -0.06 and 0.20 respectively followed by GPCC (NE = 0.58), TRMM (NE = 0.62), and PERSIANN (NE = 0.80).

Table 3.5 Statistical performance indices of the average annual maximum flood extents of the gridded precipitation datasets of 2000–2007.

Index	Gauge	APHRODITE	GPCC	PERSIANN	GSMaP	TRMM
TR	0.62	0.69	0.58	0.53	0.65	0.57
HR	0.81	0.62	0.86	0.91	0.69	0.86
NE	0.33	-0.06	0.58	0.80	0.20	0.62

GPCC and TRMM and APHRODITE were found to be suitable rainfall product to be used in hydrological modeling in the MRB. The GSMaP product underestimated the amount of

rainfall while PERSIANN-CDR overestimated the rainfall in the MRB. This result agreed with the previous study by Try et al. (2018b) which validated and used the APHRODITE product for modeling a single flood event in the LMB. Guo et al. (2015) found out that GSMaP and TRMM performed better while PERSIANN could not achieve good correlation coefficients in the Central Asia region. Tan et al. (2015) mentioned that TRMM (3B42V7) and APHRODITE performed the best over Malaysia while PERSIANN-CDR had the worst performance. However, PERSIANN-CDR was found to underestimate the rainfall over the Luanhe River Basin, China, and the bias-corrected version of TRMM (3B42) had the smallest error and highest correlation coefficient compared with the real-time version of TRMM (3B42RT) and PERSIANN-CDR.

Results from this study were in line with those of Thom et al. (2017), indicating that the TRMM and APHRODITE datasets had good performances as input data to a hydrological model in the Srepok River Catchment, a tributary of the MRB. However, the GPCC dataset was not evaluated in the above study (Thom et al., 2017). Findings from the present study showed that the high-resolution dataset did not always perform better in comparison with the coarse resolution datasets. For instance, GPCC at the coarsest resolution (1°) performed better than the other products while GSMaP (resolution 0.1°) did not perform well for a large-scale basin such as the MRB. A similar conclusion was found by Vu et al. (2012) where the GPCP rainfall product (i.e. resolution of 1°) was proved to be the second accurate dataset in the Dak Bla river basin, Vietnam.

3.4 Summary

This chapter investigated the performance of the five gridded precipitation datasets for rainfall-runoff modeling and flood inundation simulation in the MRB. The results indicated that the RRI model performed well for prediction of river discharge and flood inundation in the MRB. In addition, TRMM, GPCC, and APHRODITE had a better performance compared to GSMaP and PERSIANN-CDR for rainfall-runoff and inundation modeling in the whole MRB. GPCC and APHRODITE were found suitable for climate change studies and hydrological extreme event analysis in this region since these datasets provide long-

term availability. Additionally, the TRMM dataset is available with 3-hour and daily temporal resolutions up to date, so it could be a useful data source for the flood event and real-time flood modeling. This study provides useful guidance for applications of the gridded precipitation for the hydrological modeling and assessing annual maximum inundated extents.

References

Ashouri, H., Hsu, K.L., Sorooshian, S., Braithwaite, D.K., Knapp, K.R., Cecil, L.D., Nelson, B.R., and Prat, O.P. (2015). PERSIANN-CDR: Daily Precipitation Climate Data Record from Multisatellite Observations for Hydrological and Climate Studies. *Bulletin of the American Meteorological Society*. 96(1): 69–83. doi: 10.1175/BAMS-D-13-00068.1.

Friedl, M.A., Sulla-Menashe, D., Tan, B., Schneider, A., Ramankutty, N., Sibley, A., and Huang, X. (2010). MODIS Collection 5 global land cover: Algorithm refinements and characterization of new datasets. *Remote Sens. Environ*. 114(1): 168–182. doi: 10.1016/j.rse.2009.08.016.

Guo, H., Sheng, C., Anming,. B, Jujun, H., Abebe, G., Xianwu, X., and Xinhua, Z. (2015). Inter-comparison of high-resolution satellite precipitation products over Central Asia. *Remote Sensing*, 7(6): 7181-7211. doi: 10.3390/rs70607181.

Habib, E., Haile, A., Sazib, N., Zhang, Y., and Rientjes, T. (2010). Effect of bias correction of satellite-rainfall estimates on runoff simulations at the source of the Upper Blue Nile. *Remote Sensing*, 6(7): 6688-6708. doi: 10.3390/rs6076688.

Hu, M., Sayama, T., Duan, W., Takara, K., He, B., and Luo, P. (2017). Assessment of hydrological extremes in the Kamo River Basin, Japan. *Hydrological Sciences Journal*, 62(8): 1255-1265. doi: 10.1080/02626667.2017.1319063.

Hu, M., Zhang, X.Q., Li, Y., Yang, H., and Tanaka, K. (2019). Flood mitigation performance of low impact development technologies under different storms for retrofitting an urbanized area. *Journal of Cleaner Production*, 222: 373-380. doi: 10.1016/j.jclepro.2019.03.044.

Huffman, G.J., Bolvin, D.T., Nelkin, E.J., Wolff, D.B., Adler, R.F., Gu, G., Hong, Y., Bowman, K.P., and Stocker, E.F. (2007). The TRMM Multisatellite Precipitation

Analysis (TMPA): Quasi-Global, Multiyear, Combined-Sensor Precipitation Estimates at Fine Scales. Journal of Hydrometeorology, 8(1): 38–55. doi: 10.1175/JHM560.1.

Kobayashi, S., Ota, Y., Harada, Y., Ebita, A., Moriya, M., Onoda, H., Onogi, K., Kamahori, H., Kobayashi, C., Endo, H., and Miyaoka, K. (2015). The JRA-55 Reanalysis: General specifications and basic characteristics. *J. Meteor. Soc. Japan*, 93: 5-48, doi: 10.2151/jmsj.2015-001.

Kubota, T., Shige, S., Hashizume, H., Aonashi, K., Takahashi, N., Seto, S., Hirose, M., Takayabu, Y.N., Ushio, T., Nakagawa, K., and Iwanami, K. (2007). Global Precipitation Map Using Satellite-Borne Microwave Radiometers by the GSMaP Project: Production and Validation. *IEEE Transactions on Geoscience and Remote Sensing*, 45(7): 2259–2275. doi: 10.1109/TGRS.2007.895337.

Lu, X., Kummu, M., and Oeurng, C. (2014). Reappraisal of Sediment Dynamics in the Lower Mekong River, Cambodia. *Earth Surface Processes and Landforms*. 39(14): 1855–1865. doi: 10.1002/esp.3573.

Luo, X., Wu, W., He, D., Li, Y., and Ji, X. (2019). Hydrological Simulation Using TRMM and CHIRPS Precipitation Estimates in the Lower Lancang-Mekong River Basin. *Chinese Geographical Science*. 29(1): 13-25. doi: 10.1007/s11769-019-1014-6.

MRC, (2011). Planning atlas of the lower Mekong river basin. Mekong River Commission. Vientiane, Laos PDR.

MRC, (2015). Annual Mekong Flood Report 2011. Mekong River Commission. Vientiane, Laos PDR.

Oeurng, C., Thomas, A.C., Chung, S., Kondolf, M.G., Thanapon, P., and Mauricio, E.A. (2019). Assessing Climate Change Impacts on River Flows in the Tonle Sap Lake Basin, Cambodia. Water. 11: 618. doi: 10.3390/w11030618.

Okada, T., McAneney, K.J., and Chen, K. (2011). Estimating insured residential losses from large flood scenarios on the Tone River, Japan– a data integration approach. *Nat. Hazards Earth Syst. Sci.* 11: 3373-3382. doi: 10.5194/nhess-11-3373-2011.

Ono, K., Kazama, S., Luminda, N.G., and Koichiro, K. (2013). An Investigation of Extreme Daily Rainfall in the Mekong River Basin Using a Gridded Precipitation Dataset. *Hydrological Research Letters*, 7(3): 66–72. doi: 10.3178/hrl.7.66.

Perera, E., Sayama, T., Magome,. J, Hasegawa, A., and Iwami, Y. (2017). RCP8.5-Based Future Flood Hazard Analysis for the Lower Mekong River Basin. *Hydrology*, 4(4): 55. doi: 10.3390/hydrology4040055.

Phoeurn, C., and Ly, S. (2018). Assessment of satellite rainfall estimates as a pre-analysis for water environment analytical tools: A case study for Tonle Sap Lake in Cambodia. *Engineering Journal*. 22: 229-241. doi: 10.4186/ej.2018.22.1.229.

Sayama, T., Tatebe, Y., Iwami, Y., and Tanaka, S. (2015a). Hydrologic Sensitivity of Flood Runoff and Inundation: 2011 Thailand Floods in the Chao Phraya River Basin. *Natural Hazards and Earth System Sciences*. doi: 10.5194/nhessd-2-7027-2014.

Sayama, T., Tatebe, Y., and Tanaka, S. (2015b). An Emergency Response-Type Rainfall-Runoff-Inundation Simulation for 2011 Thailand Floods. *Journal of Flood Risk Management*, 10(1): 65-78. doi: 10.1111/jfr3.12147.

Tan, M., Ab, I., Zheng, D., Arthur, C., and Vincent, C. (2015). Evaluation of six high-resolution satellite and ground-based precipitation products over Malaysia. *Remote Sensing*. 2: 1504-1528. doi: 10.3390/rs70201504.

Tanaka, T., Yoshioka, H., Siev, S., Fujii, H., Fujihara, Y., Hoshikawa, K., Ly, S., and Yoshimura, C. (2018). An Integrated Hydrological-Hydraulic Model for Simulating Surface Water Flows of a Shallow Lake Surrounded by Large Floodplains. *Water,* 10(9), 1213. doi: 10.3390/w10091213.

Thom, V.T., Dao, N.K., and Do, Q.L. (2017). Using Gridded Rainfall Products in Simulating Streamflow in a Tropical Catchment–A Case Study of the Srepok River Catchment, Vietnam. *Journal of Hydrology and Hydromechanics*. 65(1): 18–25. doi: 10.1515/johh-2016-0047.

Try, S., Lee, D., and Lee, G. (2018a). Application of nightlight satellite imagery for assessing flooding potential area in the Mekong river basin. *J. Korea Warer Resour. Assoc*. 51(7), 565-574. doi: 10.3741/JKWRA.2018.51.7.565.

Try, S., Lee, G., Yu, W., Oeurng, C., and Jang, C. (2018b). Large-Scale Flood-Inundation Modeling in the Mekong River Basin. *Journal of Hydrologic Engineering*, 23(7). doi: 10.1061/(ASCE)HE.1943-5584.0001664.

Try, S., Lee, G., Yu, W., and Oeurng, C. (2019). Delineation of flood-prone areas using geomorphological approach in the Mekong River Basin. *Quaternary International*, 503: 79-86. doi: 10.1016/j.quaint.2018.06.026.

Try, S., Tanaka, S., Tanaka, K., Sayama, T., Oeurng, C., Uk, S., Takara, K., Hu, M., and Han, D., (2020). Comparison of gridded precipitation datasets for rainfall-runoff and inundation modeling in the Mekong River Basin. *Plos ONE*, 15(1), p.e0226814. doi: 10.1371/journal.pone.0226814.

Vu, M.T., Raghavan, S.V., and Liong, S.Y. (2012). SWAT use of gridded observations for simulating runoff – a Vietnam river basin study. *Hydrology and Earth System Sciences*, 16(8): 2801-2811. doi: 10.5194/hess-16-2801-2012.

Yamazaki, D., Ikeshima, D., Tawatari, R., Yamaguchi, T., O'Loughlin, F., Neal, J.C., Sampson, C.C., Kanae, S., and Bates, P.D. (2017). A high accuracy map of global terrain elevations. *Geophysical Research Letters*. 44: 5844-5853, doi: 10.1002/2017GL072874.

Yasutomi, N., Atsushi, H., and Akiyo, Y. (2011). Development of a Long-Term Daily Gridded Temperature Dataset and Its Application to Rain/Snow Discrimination of Daily Precipitation. *Global Environmental Research*, 15(2): 165–172.

Yatagai, A., Kenji, K., Osamu, A., Atsushi, H., Natsuko, Y., and Akio, K. (2012). APHRODITE: Constructing a Long-Term Daily Gridded Precipitation Dataset for Asia Based on a Dense Network of Rain Gauges. *Bulletin of the American Meteorological Society*, 93(9): 1401–1415. doi: 10.1175/BAMS-D-11-00122.1.

Ziese, M., Armin, R.S., Andreas, B., Peter, F., Anja, M.C., and Udo, S. (2018). GPCC Full Data Daily Version.2018 at 1.0°: Daily Land-Surface Precipitation from Rain-Gauges Built on GTS-Based and Historic Data. doi: 10.5676/DWD_GPCC/FD_D_V2018_100.

CHAPTER 4 Projection of extreme flood inundation in the Mekong River Basin under 4 K increasing scenario using large ensemble climate data

4.1 Introduction

Climate change has a profound impact on hydrological processes through changes in precipitation and evaporation (Wang et al., 2019). It plays a significant role in altering river flow, flood characteristics, and water availability, particularly their extreme values (Hu et al., 2017). The changes in the frequency and intensity of future precipitation and flooding influence adaptation strategies of social infrastructure development and water resources management (Hu et al., 2019).

The impacts of climate change on flood risk are complicated and important for our society. Even if climate change increases rainfall intensity, the flood risk and its frequency may not always increase (Sharma et al., 2018). The possible impacts of climate change on the flow regime in the MRB may be spread into the fields of food production, water supply, transportation, and culture (MRC, 2005). Uk et al. (2018) suggested that it is necessary to study the impacts of climate change in the Tonle Sap Lake as it interacts with the main Mekong River.

Previous studies of climate change impacts on the MRB generally depended on individual General Circulation Model (GCM) or mean of GCM ensembles. Kiem et al. (2008) used a single output from the high-resolution Japanese Meteorological Agency Atmospheric General Circulation Model (JMA-AGCM) to investigate variations of temperature and precipitation in 2080–2099 in the MRB. Perera et al. (2017) used a combined method of super-high-resolution AGCM output with a physical-based hydrological model to project

future changes of flood inundation in the Lower Mekong Basin (LMB). Lauri et al. (2012) selected five GCMs to assess the impacts of climate change on the hydrology of the MRB in 2032–2040. Their results showed that climate change increased basin precipitation while the range between GCMs was relatively large.

Typically, a GCM reproduces a single climate scenario or a few scenarios based on some ensemble members. However, it would not be sufficient to predict quantiles for return periods of 100 years or more (Tanaka et al., 2018). Simulation with large ensemble members is necessary to reduce the uncertainty in the estimation of the probability of extreme events. Duan et al. (2019) pointed out that increasing ensemble size could improve the estimation of the mean and standard deviation values of regional precipitation events.

It is important to study the possibility of future changes in flood inundation characteristics in the LMB under climate change impact. The peak flood in the large river basin is generally related to the precipitation prior to the timing of flood peaks. For example, Sayama et al. (2015) found that 6-month precipitation showed the highest correlation to peak inundation in the Chao Phraya River Basin in Thailand. In the MRB, the information on the contribution of antecedent precipitation to peak inundation is not available up to now. So far, there has been no study focusing on the effective duration to evaluate the relative changes in precipitation using large ensemble datasets under climate change in the MRB.

The goal of this study is to address the following questions. (1) What is the duration of effective precipitation contributing to peak flood inundation in the LMB? (2) What is the possible change in the effective precipitation under the future climate condition? (3) What are the projected extreme floods in the future with respect to the peak discharge, the flood extent, and the inundation volume in the LMB using a large ensemble climate dataset?

4.2 Methodology

4.2.1 Flood Inundation Modeling

The river discharge and inundation were simulated using the rainfall-runoff-inundation (RRI) model with a diffusive wave approximation (Sayama et al., 2012; 2015). The topographic information was derived from the MERIT DEM (Yamazaki et al., 2017) by scaling up from 3-arc second (~90 m) to 5-arc minute (~10 km) for the whole MRB simulation and 60-arc second (~2 km) for the LMB. Try et al. (2020) suggested that the Global Precipitation Climatology Centre (GPCC) product is suitable for long-term hydrological modeling in the MRB. Therefore, GPCC precipitation was used for long-term verification in this study. Surface evapotranspiration was obtained from the Japanese 55-year Reanalysis dataset (JRA-55, Kobayashi et al., 2015), and land use was available from MODIS (product: MCD12Q1, year: 2000, Friedl et al., 2010). The river cross-section parameters, river width W (m) and depth D (m), were calculated from equations (4.1) and (4.2) validated by Try et al. (2018) as a function of upstream area A (km^2). Try et al. (2020) have calibrated and validated the RRI model for 8 years (2000–2007) in the MRB. This study used the validated RRI model for flood inundation simulation (1983–2010) to confirm the capability of the model for long-term simulation. Table 4.1 shows the parameter setting used for long-term simulation.

$$D = 0.0015 \times A^{0.7491} \tag{4.1}$$

$$W = 0.0520 \times A^{0.7596} \tag{4.2}$$

Table 4.1 The values of parameter setting of the RRI model used in the study.

Parameters			Mountains	Plains
Manning's coefficient for slope	n	($m^{-1/3}s$)	0.4	0.015
Soil depth	d	(m)	2.0	-
Lateral saturated hydraulic conductivity	k_a	(m/s)	0.1	-
Parameter of unsaturated hydraulic conductivity	β	-	9.0	-
Vertical hydraulic conductivity	k_v	(cm/h)	-	0.06
Soil porosity	φ	-	-	0.6
Wetting front soil suction head	S_f	-	-	0.273
Manning's coefficient for river	n_{river}	($m^{-1/3}s$)	0.03	

4.2.2 Model Performance Indices

The statistical indicators of Nash-Sutcliffe Efficiency (NSE) and Peak Discharge Ratio (PDR) were used for evaluating discharge simulation.

$$\text{NSE} = 1 - \frac{\sum(Q_{sim}(t) - Q_{obs}(t))^2}{\sum(Q_{obs}(t) - \overline{Q_{obs}})^2} \quad (4.3)$$

$$\text{PDR} = Q_{sim}^{peak} / Q_{obs}^{peak} \quad (4.4)$$

where $Q_{sim}(t)$ and $Q_{obs}(t)$ are the simulated and observed discharge at a daily time step t. $\overline{Q_{obs}}$ is mean of observed discharge. Q_{sim}^{peak} and Q_{obs}^{peak} are simulated and observed annual peak discharge.

To evaluate the performance of modelled flood extent, the true ratio (TR) and hit ratio (HR) were used:

$$TR = \frac{IC_{obs} \cap IC_{sim}}{IC_{sim}} \quad (4.5)$$

$$HR = \frac{IC_{obs} \cap IC_{sim}}{IA_{obs}} \quad (4.6)$$

where IC_{sim} and IC_{obs} are the number of inundated cells from simulation and observation. The observed inundation maps were available from NASA MODIS near-real-time global flood mapping product (https://floodmap.modaps.eosdis.nasa.gov/) whose spatial and temporal resolutions are 250 m and 3 days at global scale (Nigro et al., 2014).

4.2.3 d4PDF Dataset

This study used present and future climate variables (precipitation and evapotranspiration) extracted from the d4PDF dataset. The d4PDF is a large number of ensemble climate experiments available with 60 km resolution on the global scale (Mizuta et al., 2017). The present climate simulation (1951–2010) has 100 ensemble members, and the future climate simulation (2051–2110) has 90 ensemble members including six sea surface temperature (SST) patterns and 15 members for each SST. The future climate was projected under the global mean surface air temperature 4 K warmer than the pre-industrial climate, corresponding to the representative concentration pathway 8.5 (RCP8.5) of CMIP5 models. The d4PDF dataset considered SST patterns obtained from the six CMIP5 model outputs: CCSM4, GFDL-CM3, HadGEM2-AO, MIROC5, MPI-ESM-MR, and MRI-CGCM3 denoted as CC, GF, HA, MI, MP, and MR, respectively.

4.2.4 The Generalized Extreme Value (GEV) Distribution

The GEV is a well-known three-parameter distribution for flood extreme fitting from a generalization of three extreme value distributions: Fréchet, Weibull, and Gumbel. The cumulative distribution function (CDF) and probability density function (PDF) of the GEV with variable x are given by the following equations:

$$F(x) = \exp\left\{-\left[1 + \xi\left(\frac{x-\mu}{\sigma}\right)\right]^{-\frac{1}{\xi}}\right\} \quad (4.7)$$

$$f(x) = \frac{1}{\sigma}\left[1 + \xi\left(\frac{x-\mu}{\sigma}\right)\right]^{-1-\frac{1}{\xi}} \exp\left\{-\left[1 + \xi\left(\frac{x-\mu}{\sigma}\right)\right]^{-\frac{1}{\xi}}\right\} \quad (4.8)$$

where μ, σ, and ξ are the location, scale, and shape parameters, respectively.

4.2.5 Statistical Testing

The Kolmogorov-Smirnov (K–S) test is a non-parametric test to check the variation of the CDF of two samples. The maximum difference between two CDFs ranges from 0 to 1 defined by:

$$D_{n,m} = \sup_x |F_n(x) - F_m(x)| \quad (4.9)$$

where F_n and F_m are the empirical distribution functions of the two samples, and sup is supremum function. The null hypothesis, H_0, assumes that the two samples have no significant difference in CDF. When the likelihood of the different distribution of the two samples exceeds a significance level, the null hypothesis is rejected. Two samples have different distribution if

$$D_{n,m} > c(\alpha)\sqrt{\frac{n+m}{nm}} \quad (4.10)$$

where n and m are the sample sizes. At the 5% significance level, $c(\alpha)$ is equal to 1.36. The K-S test of two samples was used to test the variability of annual peak discharge from SST patterns. Each SST pattern covered the period of 60 years with 15 ensemble members (900 years for serial simulation); the rejection of the null hypothesis corresponded to K-S statistics exceeding 0.0641.

This study used the Kullback-Leibler (K-L) divergence to evaluate the difference of probability distribution functions p_1 and p_2 for present and future precipitations of d4PDF as shown in the following:

$$D_{KL}(p_1 \parallel p_2) = \sum_{i=1}^{L} p_{1i} log_2 \left(\frac{p_{1i}}{p_{2i}}\right) \quad (4.11)$$

The probability of i-th value is from set of L elements.

4.2.6 Analysis Procedure

Figure 4.1 shows the flowchart of this study. First, the RRI model was validated from 1983 to 2010. The same parameter setting was used to simulate the present and future discharge and flood inundation. Next, different intervals of precipitation (1-month to 6-month) were calculated counting backward from the day of peak flood to determine the correlation of effective precipitation and peak flood inundation. Their correlation coefficients were determined in comparison to peak discharge and inundation volume. Then, the changes in the most effective precipitation from the present to the future were evaluated. The validated RRI model was used to simulate the whole period and ensemble members of the present (60-year: 1951–2010 × 100-member) and future (60-year: 2051–2110 × 90-member) climate experiments of d4PDF. The flood probability of the present simulation of d4PDF was checked with observed discharge. The simulated peak discharges of the present and future extreme flood events were investigated using GEV fitting. Moreover, the K–S test of two samples was used to check and discuss the variability of different SSTs. Finally, changes in extreme flood events (50-year, 100-year, and 1000-year return periods) were investigated between the present and future climate experiments.

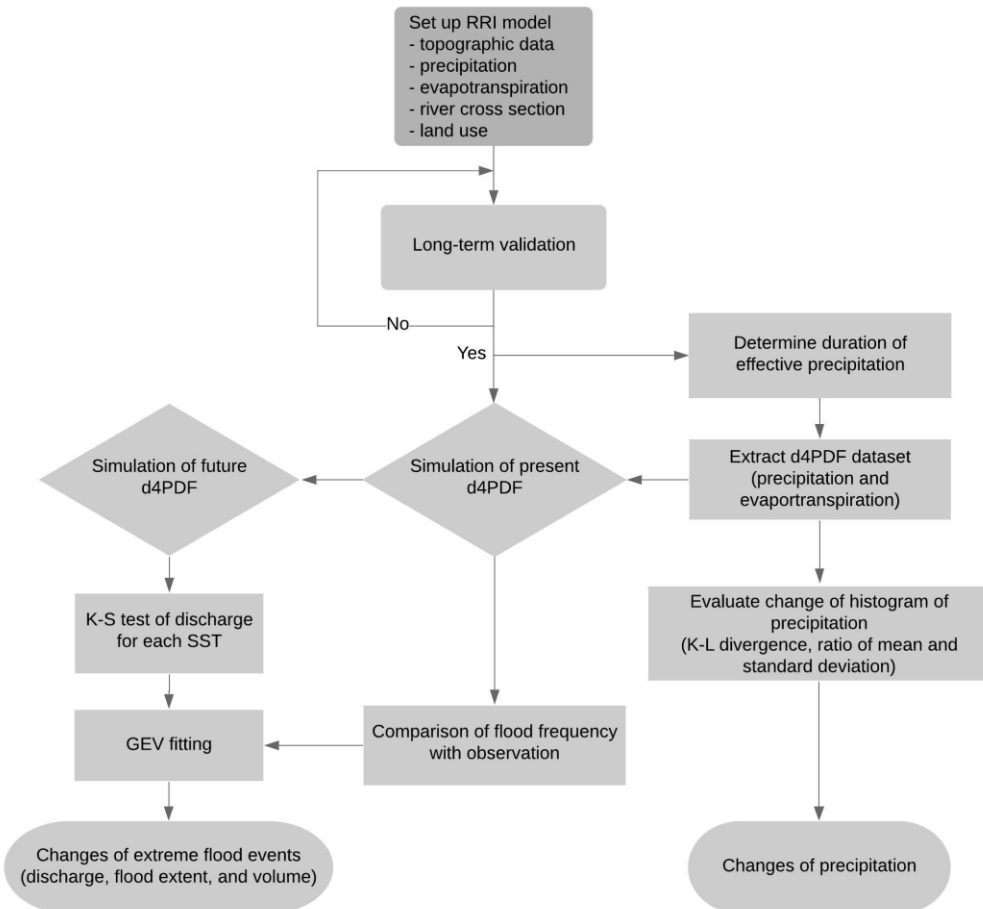

Figure 4.1 Flowchart of this study.

4.3 Results

4.3.1 Long-term Model Validation

The RRI model was validated for 1983 to 2010. The simulation of discharge (Figure 4.2) at the daily time step performed satisfactorily with NSE of 0.71, 0.86, and 0.88 at the stations of Luang Prabang, Pakse, and Kratie, respectively. The coefficient of PDR varied for each year and the station location (Table 4.2). At the Luang Prabang station, most of the years showed an underestimation of model performance with the average PDR = 0.67±0.13. The performances of the RRI model were more satisfactory with PDR =

0.96±0.17 and 0.98±0.16 at Pakse and Kratie. This study mainly focuses on peak flood inundation in the LMB in which the Kratie station is located; therefore, the RRI model is suitable for further analysis in the next section.

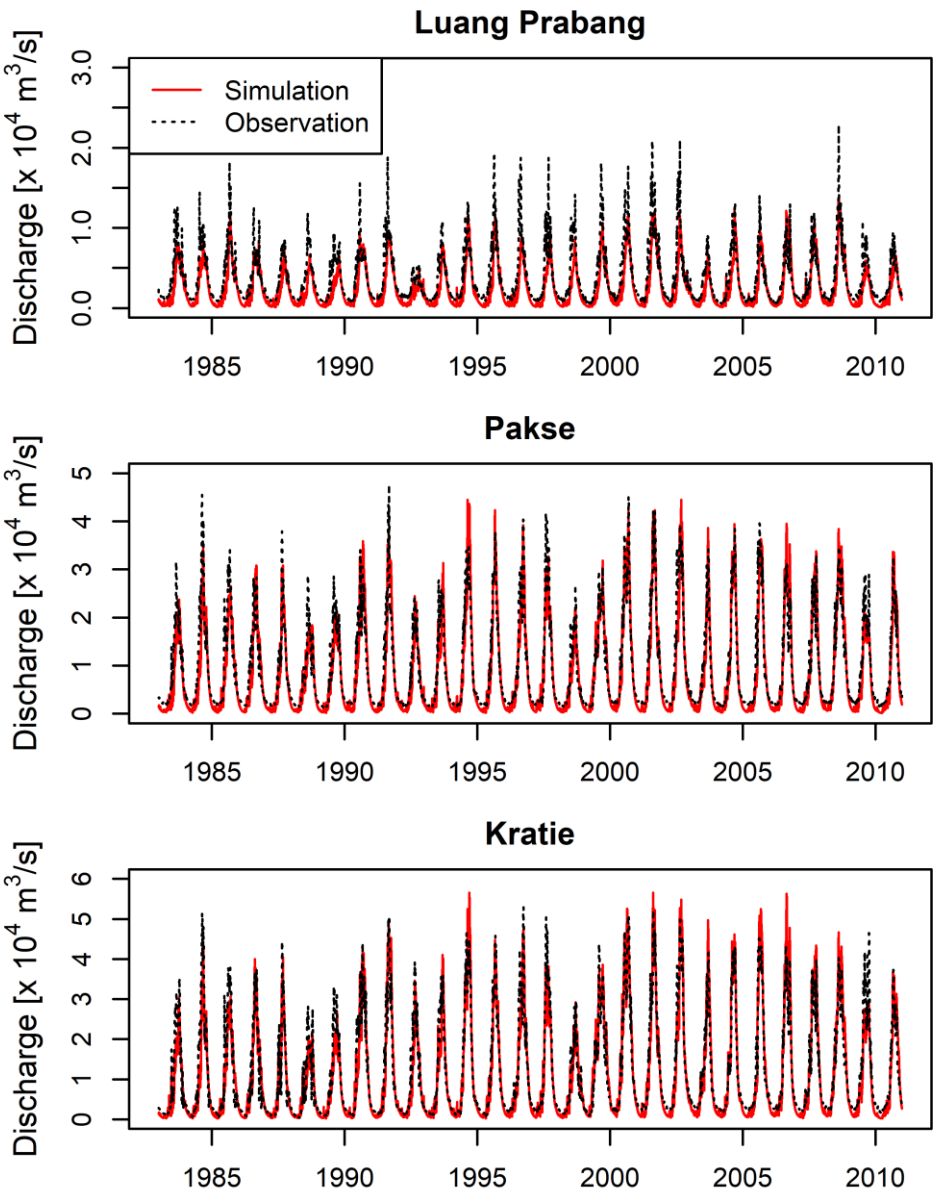

Figure 4.2 Comparison of daily observed and simulated discharge at Luang Prabang, Pakse, and Kratie.

Table 4.2 The Peak Discharge Ratio (PDR) values of simulation over observed discharge.

year	Luang Prabang	Pakse	Kratie
1983	0.64	0.75	0.87
1984	0.57	0.77	0.85
1985	0.65	0.78	0.81
1986	0.66	1.09	1.08
1987	0.82	0.81	0.91
1988	0.56	0.64	0.74
1989	0.69	0.73	0.81
1990	0.61	1.05	0.98
1991	0.50	0.78	0.97
1992	0.83	0.99	0.88
1993	0.72	1.12	1.14
1994	0.87	1.28	1.22
1995	0.61	1.12	0.98
1996	0.48	0.97	0.90
1997	0.51	0.78	0.77
1998	0.62	0.82	0.99
1999	0.59	1.04	0.88
2000	0.65	0.93	1.04
2001	0.58	1.00	1.08
2002	0.58	1.13	1.10
2003	0.75	1.13	1.17
2004	0.97	1.02	1.07
2005	0.67	0.92	1.16
2006	0.93	1.24	1.30
2007	0.88	1.02	1.08
2008	0.61	1.10	1.16
2009	0.54	0.72	0.63
2010	0.69	1.03	0.98
mean ± STD	0.67±0.13	0.96±0.17	0.98±0.16

To evaluate the performance of annual maximum inundation, the threshold of inundation depth of 0.5 m was selected following previous studies (Sayama et al., 2012; 2015; Try et al., 2018; 2020) to identify the flooded and non-flooded areas. The statistic indices of observation and model prediction flood extent for 8 years (2000–2007) were calculated (see Figure 4.3 for the comparison map of simulation and observation). The spatial performance index TR ranged from 0.42 to 0.82 where average accuracy was 58% (avg. TR = 0.58). The indicator HR varied from 0.76 to 0.94 (Table 4.3), and its mean value was 0.86. However, there was a difference between simulated and satellite observed flood extent at the lowest part of the Mekong delta where the simulation could not identify the inundated area. The factors which reduced inundation accuracy would come from two main sources. First, the satellite observation would not be able to detect flooded area at the mangrove forests on the banks of the Tonle Sap Lake while the simulation might correctly identify the area under inundation. Secondly, the simulation was not able to detect the inundated area in some low parts of the Mekong delta where might be influenced by saltwater intrusion. This effect was not considered in this study due to unavailability of observed information.

Table 4.3 The statistical indices of model performance of flood extent: TR and HR.

	2000	2001	2002	2003	2004	2005	2006	2007	avg.
TR	0.82	0.74	0.65	0.42	0.58	0.46	0.49	0.47	0.58
HR	0.85	0.80	0.87	0.89	0.76	0.88	0.94	0.89	0.86

Figure 4.4 shows the relationship between precipitation amounts of different intervals (horizontal axis) and peak discharge (left vertical axis) and peak inundation volume (right vertical axis). The basin-averaged precipitation upstream of the Kratie station was calculated and plotted with peak discharge while the whole basin-averaged precipitation was plotted with peak inundation in the LMB. The results revealed that 3-month precipitation (90 days) had the highest correlation ($R^2 = 0.81$) for both peak discharge and inundation volume. Consequently, the 90-day precipitation was hereafter used for further analysis of the projected future precipitation change.

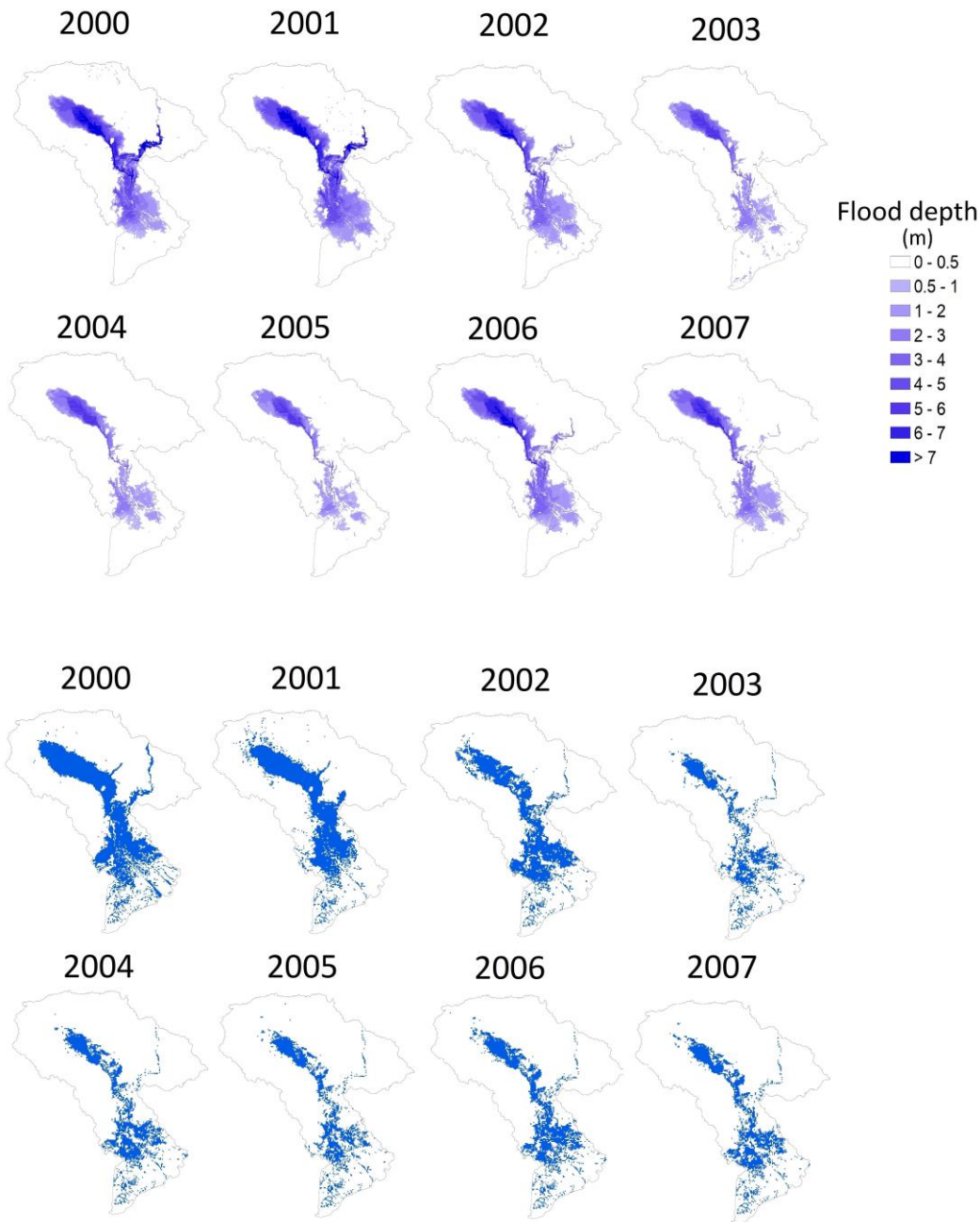

Figure 4.3 Comparison of flood extent from simulation result (top) and MODIS flood observation (bottom).

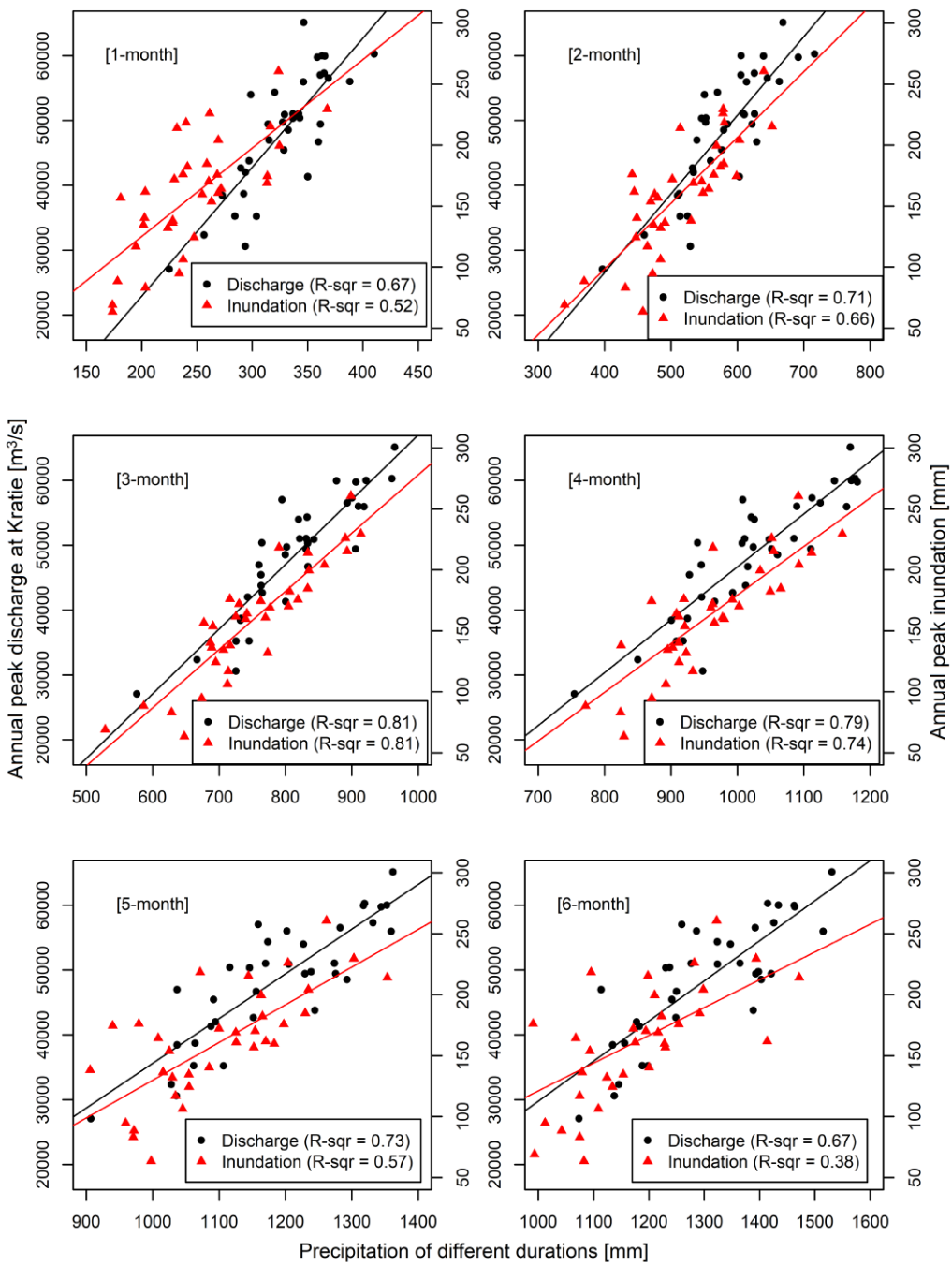

Figure 4.4 Relationship between annual peak discharge at Kratie (black dots and lines) and peak inundation volume (red dots and lines) with precipitation extracted from different durations.

4.3.2 Simulation of d4PDF Dataset

Prior to simulation using the d4PDF dataset, the performance of 90-day precipitation was compared with GPCC precipitation. Figure 4.5 shows the histogram and boxplot of maximum 90-day precipitation from the two datasets. The present d4PDF mean (777 mm) showed an underestimation of 15 mm compared to GPCC precipitation (792 mm). The d4PDF precipitation ranges from 588 mm to 1053 mm while the GPCC product ranges between 544 and 937 mm.

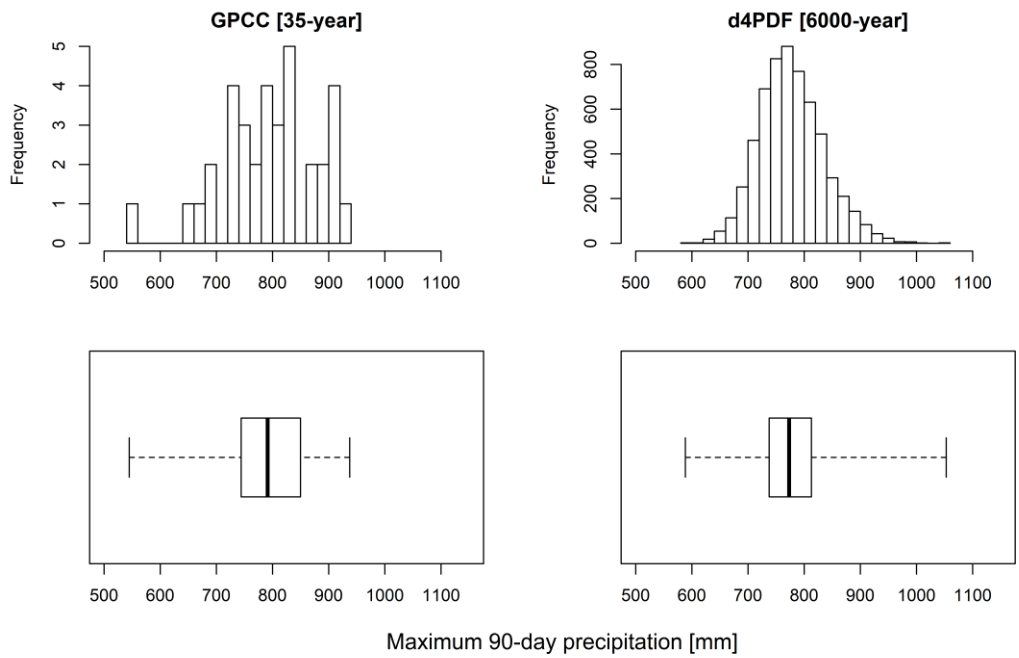

Figure 4.5 Comparison of histogram and boxplot of annual maximum 90-day precipitation from GPCC and d4PDF.

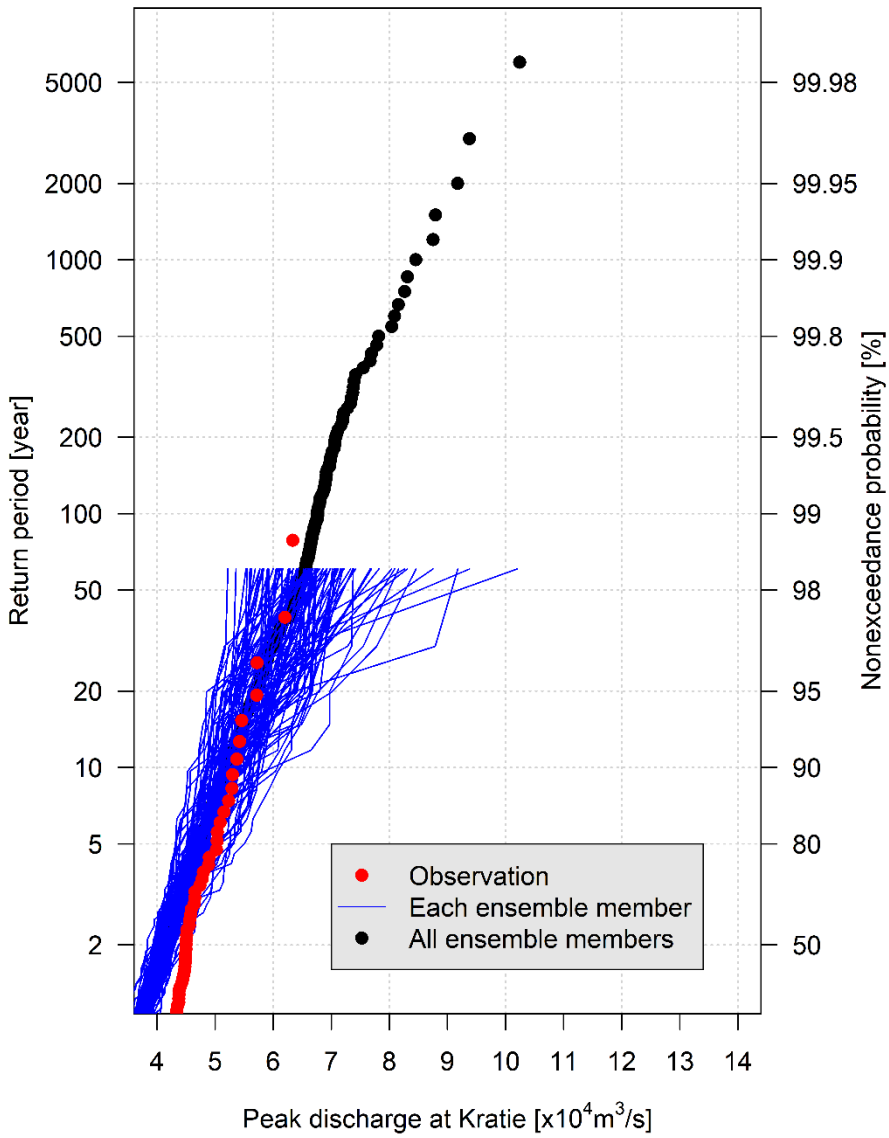

Figure 4.6 Comparison of probability plot of annual peak discharge at Kratie.

Next, the validated RRI model simulated the present experiment of d4PDF (6000 years: 60 years × 100 ensembles). The annual peak discharge at Kratie in the LMB was selected for flood frequency analysis. Then, the non-exceedance probability of discharge from d4PDF was compared with the observed discharge which was available from 1934 to 2011 from the Mekong River Commission. The non-exceedance probability in Figure 4.6 was

determined by the empirical value. The red dots are observed discharge, the blue lines are d4PDF ensemble members of all 60 years and the black dots represent all ensemble members from the present experiment of d4PDF. The large observed flood events were successfully reproduced by the d4PDF ensemble members. Overall, there was a good agreement of flood magnitude between all ensemble members of d4PDF and gauged observation for the large extreme events (e.g. large recurrence interval greater than 10 years) while underestimation was seen in lower return period events (e.g. return period of 2 or 5 years). Since this study investigated large extreme events (return period of 50, 100, and 1000 years), the prediction of d4PDF ensemble was acceptable in this study.

4.3.3 Kolmogorov-Smirnov Test of Two Samples

To investigate the effect of different SST patterns in future climate experiments on the probability distribution, annual peak discharge from each SST (each sample size: 900 years) was carried out with the K-S test for all combinations of the six SST pattern distributions (CC, GF, HA, MI, MP, and MR). At 5% significance level, the results of the K-S test of annual peak discharge showed significant differences (rejection of null hypothesis) in 14 out of 15 cases (CC-GF, CC-HA, CC-MI, CC-MP, CC-MR, GF-HA, GF-MI, GF-MP, GF-MR, HA-MI, HA-MP, HA-MR, MI-MP, MI-MR, and MP-MR) while null hypothesis of only one case (CC-HA) was accepted (Table 4.4).

Table 4.4 K-S statistics evaluation of the null hypothesis test of peak discharge at Kratie (✓is acceptance of the null hypothesis, and × is rejection of the null hypothesis).

SST	GF	HA	MI	MP	MR
CC	×	✓	×	×	×
GF	-	×	×	×	×
HA	-	-	×	×	×
MI	-	-	-	×	×
MP	-	-	-	-	×

4.3.4 Projection of Future Extreme Flood

Since the annual 90-day precipitation had the best correlation with peak discharge and inundation in the LMB, the changes of maximum 90-day precipitation between the present and future climates were assessed. Figure 4.7 shows the shifted probability density of annual maximum 90-day precipitation from present to future climates in the MRB. The Kullback-Leibler divergence was tested to evaluate the shifted distance of probability density from the present (p_1) to future precipitation (p_2) with $D_{KL}(p_1 \parallel p_2)$ = 0.01 bits. The probability density of 90-day precipitation shifted from the present to future climate experiments with changes of mean from 777 mm to 900 mm (ratio: 1.16) and standard deviation from 57 mm to 96 mm (ratio: 1.67).

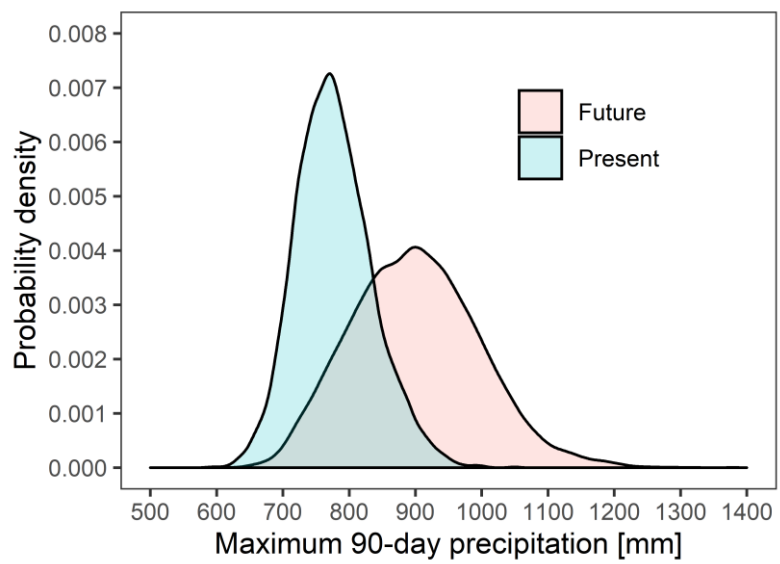

Figure 4.7 Change of probability density of present and future experiments of 90-day precipitation of d4PDF dataset.

This study investigated the magnitude of variation of 1:50, 1:100, and 1:1000 year flood events from present to future. The fitting performance of annual maximum series (AMS) and block maxima of annual peak discharge at Kratie in the LMB was compared. Dealing with the 20-year block maxima approach, we can have 300 and 270 blocks for present and

future climates. Figure 4.8 showed that 20-year block maxima had better performance compared to the AMS fitted curve for the whole dataset simulation (6000 and 5400-year for present and future). The fitted curve of the AMS curve showed an overestimation of empirical values for future projection, particularly when the return period is greater than 50 years. The GEV fitted curve of block maxima showed a good simulation of d4PDF with a greater variation for future projection. In general, there was a clear shift of flood magnitude from the present to future climate projections. The fitted curve from the 20-year block maxima was considered for the projection of extreme events in this study.

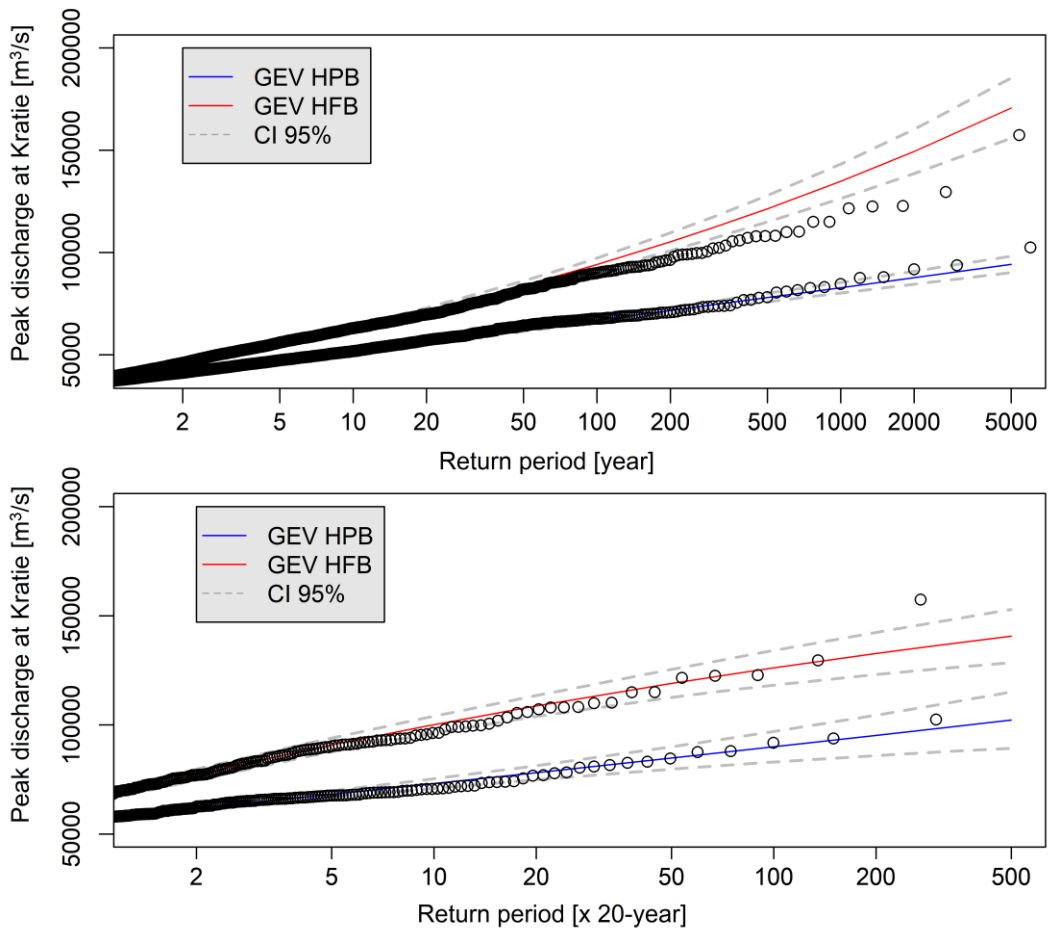

Figure 4.8 Comparison of fitting curves of discharge from annual maximum series (upper) and 20-year block maxima (lower) for present (GEV HPB) and future (GEV HFB) projections including their confidence interval (CI) 95%.

The magnitude of flood inundation of 1:50, 1:100, and 1:1000 year flood events increased from present to future climate experiments (Figure 4.9). The peak discharge at Kratie in the present was 61,588 m^3/s, 67,400 m^3/s, and 84,762 m^3/s for 1:50, 1:100, and 1:1000 year events; these values drastically rose to 77,103 m^3/s (+25%), 89,331 m^3/s (+33%), and 118,912 m^3/s (+40%) in the future (Table 4.5). Moreover, the magnitudes of the extreme events in 50, 100, and 1000 years would increase by +19%, +29%, +36% for inundation extent and +23%, +34%, +37% in terms of inundation volume in the future, respectively.

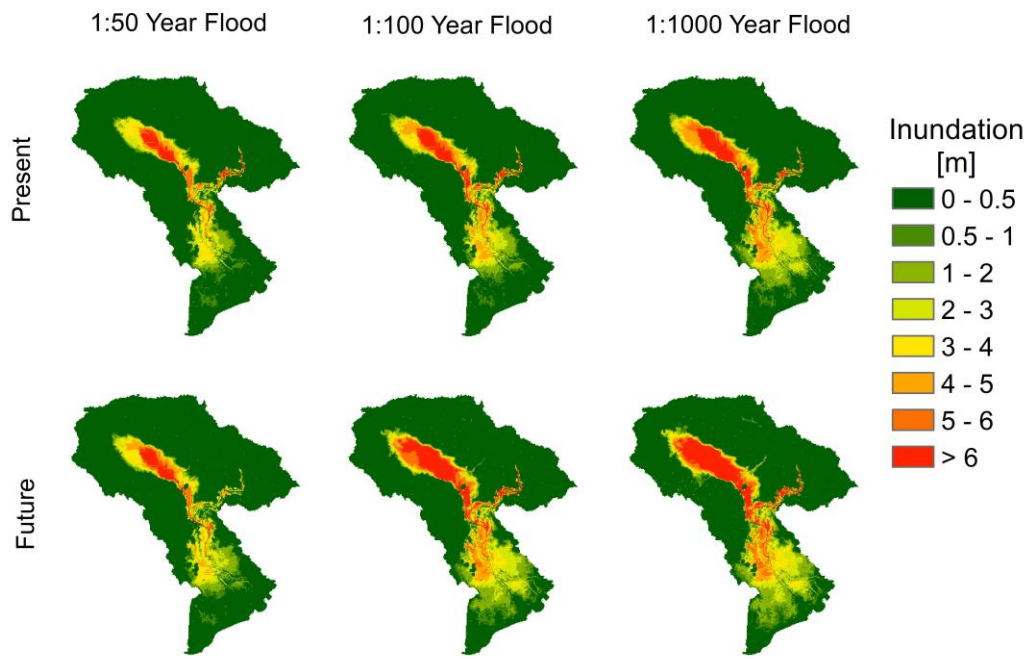

Figure 4.9 Comparison of extreme flood events (50-year, 100-year, and 1000-year return period) for present and future climate experiments.

Table 4.5 Changes of extreme flood events in the LMB from present to future. The bold italic number is relative change values.

Extreme Event		Peak Discharge (m^3/s)	Peak Area (km^2)	Peak Volume (km^3)
1:50 Year Flood	Present	61,588	31,636	114
	Future	77,103 ***(+25%)***	37,677 ***(+19%)***	140 (+23%)
1:100 Year Flood	Present	67,400	33,938	124
	Future	89,331 ***(+33%)***	43,870 ***(+29%)***	166 (+34%)
1:1000 Year Flood	Present	84,762	40,812	156
	Future	118,912 ***(+40%)***	55,438 ***(+36%)***	214 (+37%)

4.4 Discussion

4.4.1 Impact of Ensemble Members on Uncertainties

Figure 4.10 shows the deviation of precipitation and peak discharge selected from random ensemble members of the present d4PDF dataset comparing with the observations. The increasing number of ensemble members (from 2 to 100 members) can improve both the mean and tail of the distribution for both 90-day precipitation and peak discharge. The mean of deviation (central red lines in Figure 4.10) improved from -29 mm and -2,443 m^3/s (2 members) to -16 mm and -1,095 m^3/s (100 members) for precipitation and discharge, respectively. Overall, the deviation of 90-day precipitation over the MRB ranged from -171 mm to +102 mm for 2 members, and it reduced to between -131 mm and +95 mm for 100 members. The peak discharge deviation at 2 ensemble members was between -20,593 m^3/s and 16,108 m^3/s while it changed to -16,593 − 12,807 m^3/s for 100 members. Furthermore, the peak discharge changed its range from the present climate from 27,013 − 60,664 m^3/s to 35,000 − 78,169 m^3/s in the future. The uncertainty boundary of flood inundation extent was assessed for the present and future experiments as shown in Figure

4.11. The range between lower and upper tails of the inundated area shifted from 17,154 − 38,622 km^2 to 18,458 − 43,131 km^2 for present and future climates, respectively.

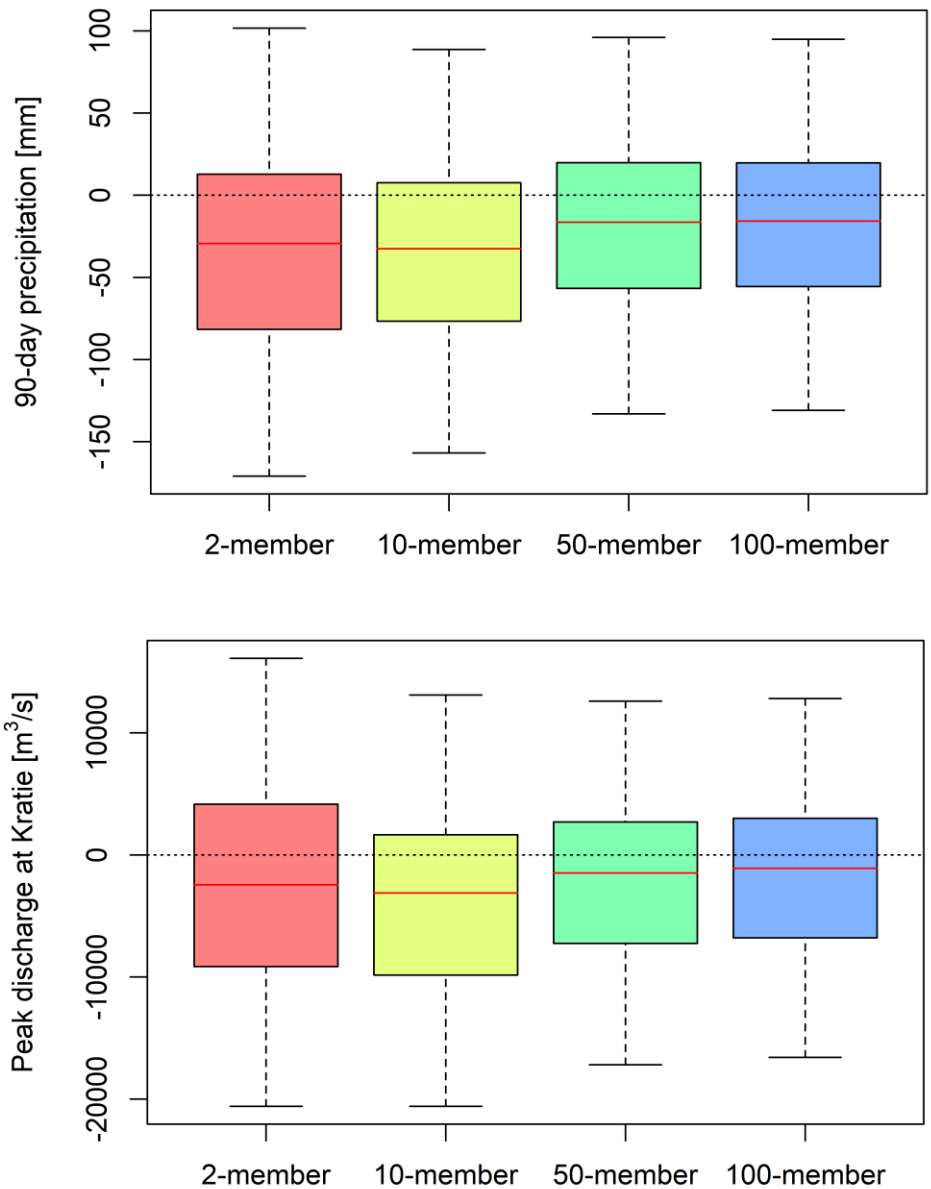

Figure 4.10 The boxplot of the deviation of ensemble number for 90-day precipitation (left) and peak discharge at Kratie (right). The values represent the deviation from the mean of observation. Samples of 2, 10, and 50 members were randomly selected from a total size of 100 members. The central red lines represent mean values.

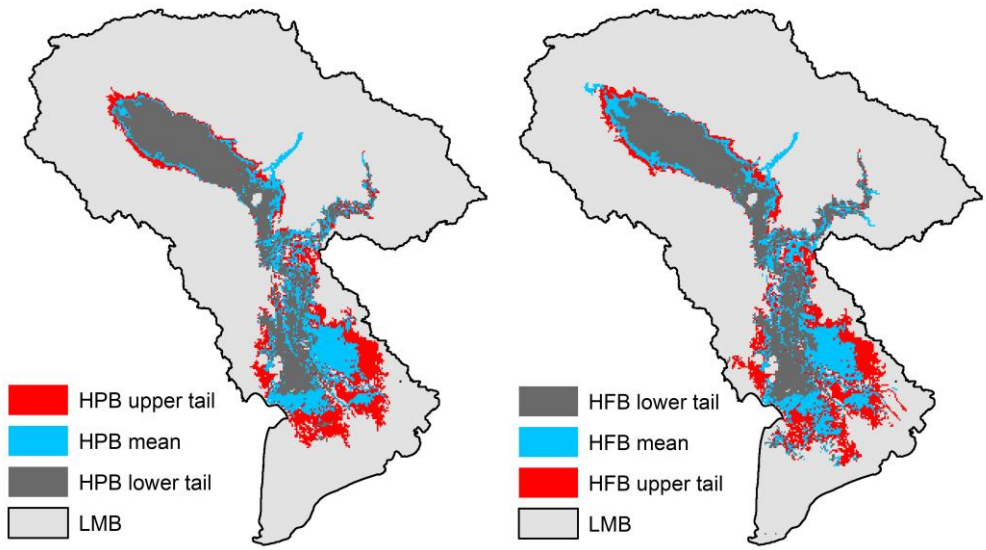

Figure 4.11 Uncertainty boundary of flood extent for the lower tail, mean, and upper tail for the total ensemble for present (left) and future projection (right) in the LMB.

4.4.2 Impact of Mainstream Dams

During the study period (1983–2010), the construction of four dams along the mainstream of the upper Mekong River in China (Binh et al., 2017) was completed (Manwan in 1993, Dachaoshan in 2001, Jinhong in 2008, and Xiaowan in 2009), and two more dams operated in 2012 (Gongguoqiao and Nouzhadu). The Xayaburi dam in Lao PDR was operated in 2019 while other several dams were under construction. To check the impact of Chinese cascade dams on hydrology in the MRB, the simulation period (2012–2016) was conducted by considering six dams operated from 2012. Since there was no available information on dam operation rules, the simulation assumed that the dams were operated to maximize water storage in the reservoirs in flood season and minimize storage in the dry season. Figure 4.12 indicated that these six dams had obvious impacts (i.e. PDR of simulation with and without dams = 0.90) in Chiang Saen, the direct outlet from the Upper Mekong in China. The impacts on peak flooding were gradually weakening at the lower hydrological stations of the basin (PDR = 0.96, 0.99, and 0.99 at Vientiane, Pakse, and Kratie,

respectively). Hence, we could conclude that the impacts of dams are limited by the downstream distance, and the impacts could be neglected at Kratie during peak flooding in the floodplain area of the MRB.

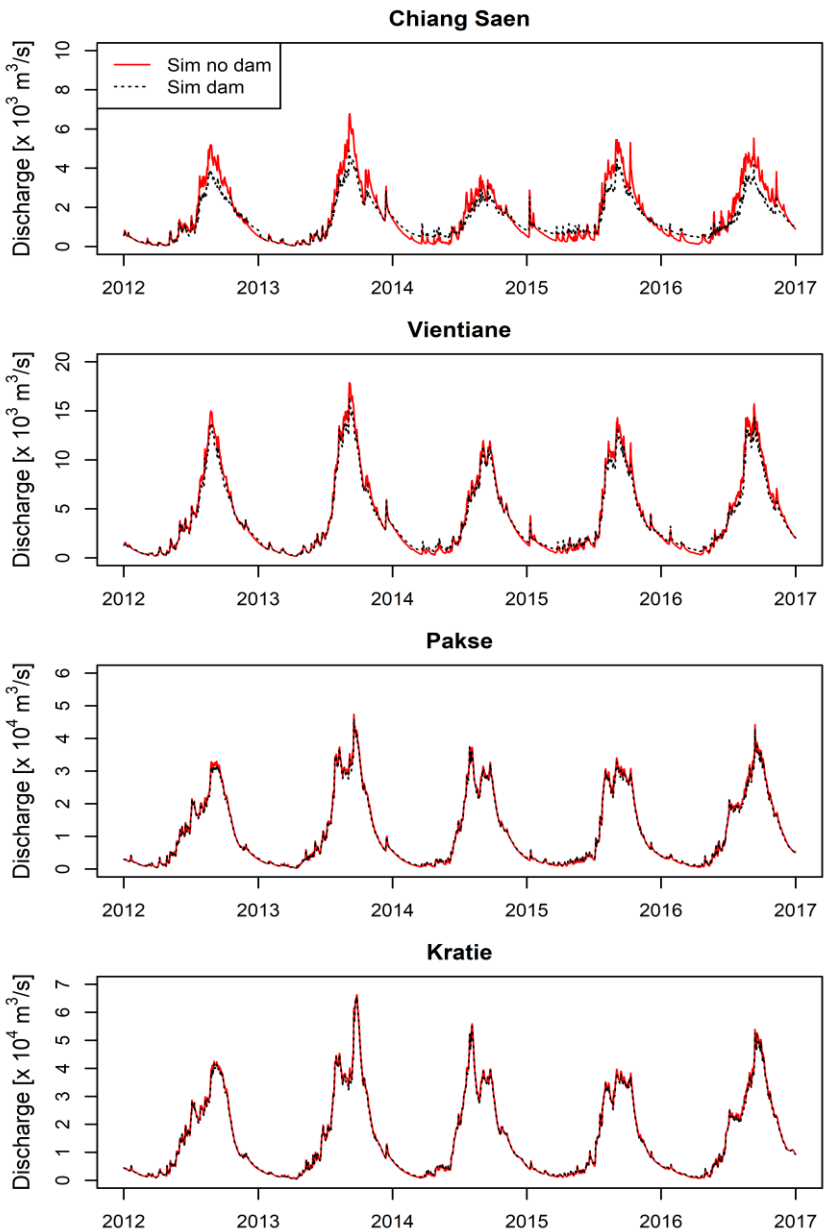

Figure 4.12 The simulation with and without dam at hydrological stations along the mainstream of the MRB.

4.4.3 Implementation of Future Changes

This study investigated the changes in extreme flood inundation events between the present and the future using a large ensemble dataset (d4PDF). The flood probability from all ensemble members in the present d4PDF had a good agreement with observation in the MRB. Similarly, Tanaka (2019) found a very strong relationship between 100-year return level and ensemble mean of block maxima over six river basins in Japan. The application of a large ensemble dataset was able to predict extreme flood events in spite of the absence of bias correction of climate data in this study.

The K-S test showed a significant difference in future SST patterns (14 out of 15 SST combination cases). Duan et al. (2019) also found that the boundary condition input of the SST pattern was a major source of uncertainty in future precipitation projection in southern China. The different patterns of SST play a critical role in extreme precipitation and flood inundation. As a result, ensuring realistic SST patterns is essential when improving the performance of atmospheric models for further climate projection.

The impacts and severity of climate change differ for each sub-basin of the MRB. Oeurng et al. (2019) found that it is likely to decrease in extreme flows in both high and low flow seasons in 11 sub-basins of the Tonle Sap Lake in the LMB. Shrestha et al. (2016) investigated flow change in the Sekong, Sesan, and Srepok (3S), a large sub-basin of the MRB, and revealed a huge growth from 54.1 to 78.9% for the RCP2.6 to RCP8.5 scenarios. However, the studies of climate change effects on river flow for the whole MRB found a similar increase with this study. For instance, Perera et al. (2017) identified an increase of discharge volume at Kratie of 25% from the present (1979–2003) to future climate (2075–2099) under the RCP8.5 scenario. In addition, Lauri et al. (2012) found increases of 13.4% and 8.1% at Kratie in 2032 to 2049 under the A1B and B1 scenarios (comparable to RCP6.0 and RCP4.5, respectively).

4.4.4 Limitations

The potential impacts of climate change on extreme flood inundation in the LMB were conducted under a 4 K warming scenario (comparable to RCP8.5) for future climate projection in the MRB. Other scenarios such as RCP2.6, RCP4.5, and RCP6.0 for future projection were not taken into account in this study. It would require huge and expensive calculation resources because the climate dataset (d4PDF) has large ensemble members (i.e. 90 ensemble members for only the +4K future scenario). This study used projected climate data based on only one GCM (MRI-AGCM) by considering other six GCM in SST setting, but the projection of future flood inundation is also dependent on different GCMs of which direction and model structure may deviate from each other. Due to different of evapotranspiration is quite small between each ensemble member in the climate projection; therefore, this study assumed the same evapotranspiration for each ensemble member.

The simulation uncertainty in this study might be due to some important sources. First, land use was assumed to be static during the simulation period for model verification (1983–2010). Additionally, the influence of model structure and parameters was not investigated. The observation data (e.g. gauged precipitation and river discharge) were insufficient to permit comparison with the baseline simulation. Plus, the future simulation did not include impacts of human activities, which could be addressed by land-use change and water infrastructures such as hydropower dams and irrigation reservoirs in the basin. The uncertainty of climate data in this study is probably due to the absence of bias correction of the d4PDF dataset. Further research will consider bias correction before conducting the simulation.

4.5 Summary

This chapter analyzed the changes in flood frequency under the impacts of climate change using present and future 4 K increasing experiments of the d4PDF dataset. The extreme flood events of the present climate experiment of d4PDF were confirmed by observed discharge. Maximum 90-day precipitation prior to peak flood was found to have the highest correlation with peak discharge and inundation in the LMB. The probability density of 90-

day precipitation significantly shifted from present to future climates in the MRB. The different patterns of SST are an important factor that significantly influences the changes in future precipitation and flood inundation in the LMB. The projection of future climate under 4 K rising experiments reveals a great increase in the severity of flood extreme events in the LMB. To reduce the forthcoming flood damages, it requires an efficient method of water resources planning and management, an effective flood warning and forecasting system, and flood mitigation techniques.

References

Binh, D. V., Kantoush, S., Sumi, T., Mai, N. T., and Trung, L.V. (2017). Study on the impacts of river-damming and climate change on the Mekong Delta of Vietnam. *Disaster Prevention Research Institute Annuals*, 60(B), 804-826.

Duan, W., Hanasaki, N., Shiogama, H., Chen, Y., Zou, S., Nover, D., Zhou, B., and Wang, Y. (2019). Evaluation and Future Projection of Chinese Precipitation Extremes Using Large Ensemble High-Resolution Climate Simulations. *Journal of Climate*, 32(8), 2169-2183. doi: 10.1175/JCLI-D-18-0465.1.

Friedl, M. A., Sulla-Menashe, D., Tan, B., Schneider, A., Ramankutty, N., Sibley, A., and Huang, X. (2010). MODIS Collection 5 global land cover: Algorithm refinements and characterization of new datasets. *Remote sensing of Environment*, 114(1), 168-182. doi: 10.1016/j.rse.2009.08.016.

Hu, M., Sayama, T., Duan, W., Takara, K., He, B., and Luo, P. (2017). Assessment of hydrological extremes in the Kamo River Basin, Japan. *Hydrological Sciences Journal*, 62(8), 1255-1265. doi: 10.1080/02626667.2017.1319063.

Hu, M., Zhang, X., Li, Y., Yang, H., and Tanaka, K. (2019). Flood mitigation performance of low impact development technologies under different storms for retrofitting an urbanized area. *Journal of Cleaner Production*, 222, 373-380. doi: 10.1016/j.jclepro.2019.03.044.

Kiem, A. S., Ishidaira, H., Hapuarachchi, H. P., Zhou, M. C., Hirabayashi, Y., and Takeuchi, K. (2008). Future hydroclimatology of the Mekong River basin simulated using the high-resolution Japan Meteorological Agency (JMA) AGCM. *Hydrological Processes*, 22(9), 1382-1394.

Kobayashi, S., Ota, Y., Harada, Y., Ebita, A., Moriya, M., Onoda, H., Onogi, K., Kamahori, H., Kobayashi, C., Endo, H., Miyaoka, K., and Takahashi, K. (2015). The JRA-55

Reanalysis: General specifications and basic characteristics. *J. Meteor. Soc. Japan*, 93: 5-48. doi: 10.2151/jmsj.2015-001.

Lauri, H., Moel, H. D., Ward, P. J., Räsänen, T. A., Keskinen, M., and Kummu, M. S. (2012). Future changes in Mekong River hydrology: impact of climate change and reservoir operation on discharge. *Natural Hazards and Earth System Sciences*, 16, 4603-4619. doi: 10.5194/hess-16-4603-2012.

Mekong River Commission (MRC), (2005). Overview of the Hydrology of the Mekong Basin, vol. 82, Vientiane, Lao PDR.

Mizuta, R., Murata, A., Ishii, M., Shiogama, H., Hibino, K., Mori, N., Arakawa, O., Imada, Y., Yoshida, K., Aoyagi, T., and Kawase, H. (2017). Over 5,000 years of ensemble future climate simulations by 60-km global and 20-km regional atmospheric models. *Bulletin of the American Meteorological Society*, 98(7), 1383-1398. doi: 10.1175/BAMS-D-16-0099.1. The d4PDF dataset is available for download at http://www.miroc-gcm.jp/~pub/d4PDF/.

Nigro, J., Slayback, D., Policelli, F., and Brakenridge, G.R. (2014). NASA/DFO MODIS near real-time (NRT) global flood mapping product evaluation of flood and permanent water detection. *Evaluation, Greenbelt, MD*, 27.

Oeurng, C., Cochrane, T. A., Chung, S., Kondolf, M. G., Piman, T., and Arias, M. E. (2019). Assessing Climate Change Impacts on River Flows in the Tonle Sap Lake Basin, Cambodia. *Water*, 11(3), 618. doi: 10.3390/w11030618.

Perera, E., Sayama, T., Magome, J., Hasegawa, A., and Iwami, Y. (2017). RCP8.5-Based future flood hazard analysis for the lower Mekong river Basin. *Hydrology*, 4(4), 55. doi: 10.3390/hydrology4040055.

Sayama, T, Ozawa, G., Kawakami, T., Nabesaka, S., and Fukami, K. (2012). Rainfall–runoff–inundation analysis of the 2010 Pakistan flood in the Kabul River basin. *Hydrological Sciences Journal*, 57(2), 298-312. doi: 10.1080/02626667.2011.644245.

Sayama, T., Tatebe, Y., Iwami, Y., and Tanaka, S. (2015). Hydrologic sensitivity of flood runoff and inundation: 2011 Thailand floods in the Chao Phraya River basin. *Natural Hazards and Earth System Sciences*, 15, 1617-1630. doi: 10.5194/nhess-15-1617-2015.

Sharma, A., Wasko, C., and Lettenmaier, D. P. (2018). If precipitation extremes are increasing, why aren't floods? *Water Resources Research*, 54(11), 8545-8551. doi: 10.1029/2018WR023749.

Shrestha, B., Cochrane, T. A., Caruso, B. S., Arias, M. E., and Piman, T. (2016). Uncertainty in flow and sediment projections due to future climate scenarios for the 3S Rivers in the Mekong Basin. *Journal of Hydrology*, 540, 1088-1104. doi: 10.1016/j.jhydrol.2016.07.019.

Tanaka, S. (2019). Interesting Statistical Characteristics of Precipitation Extremes in Major River Basins of Japan using a Large Ensemble of Climate Simulations "d4PDF". Proceeding of THA 2019 International Conference on Water Management and Climate Change towards Asia's Water-Energy-Food Nexus and SDGs, January 23-25, 2019 Bangkok, Thailand.

Tanaka, T., Tachikawa, Y., Ichikawa, Y., and Yorozu, K. (2018). Flood risk curve development with probabilistic rainfall modelling and large ensemble climate simulation data: a case study for the Yodo River basin. *Hydrological Research Letters*, 12(4), 28-33. doi: 10.3178/hrl.12.28.

Try, S., Lee, G., Yu, W., Oeurng, C., and Jang, C. (2018). Large-Scale Flood-Inundation Modeling in the Mekong River Basin. *Journal of Hydrologic Engineering*, 23(7). doi: 10.1061/(ASCE)HE.1943-5584.0001664.

Try, S., Tanaka, S., Tanaka K., Sayama, T., Oeurng, C., Uk, S., Takara, K., Hu, M., and Han, D. (2020). Comparison of gridded precipitation datasets for rainfall-runoff and inundation modeling in the Mekong River Basin. *Plos One*, (15)1. doi: 10.1371/journal.pone.0226814.

Uk, S., Yoshimura, C., Siev, S., Try, S., Yang, H., Oeurng, C., Li, S., and Hul, S. (2018). Tonle Sap Lake: Current status and important research directions for environmental management. *Lakes & Reservoirs: Research & Management*, 23(3), 177-189. doi: 10.1111/lre.12222.

Wang, H., Xiao, W., Wang, Y., Zhao, Y., Lu, F., Yang, M., Hou, B., and Yang, H. (2019). Assessment of the impact of climate change on hydropower potential in the Nanliujiang River basin of China. *Energy*, 167: 950-959. doi: 10.1016/j.energy.2018.10.159.

Yamazaki, D., Ikeshima, D., Tawatari, R., Yamaguchi, T., O'Loughlin, F., Neal, J. C., Sampson, C., Kanae, S., and Bates, P. D. (2017). A high accuracy map of global terrain elevations. *Geophysical Research Letters*, 44(11), 5844-5853. doi: 10.1002/2017GL072874.

CHAPTER 5: Assessing the Effects of Climate Change on Flood Inundation in the Lower Mekong Basin Using High Resolution AGCM Outputs

5.1 Introduction

The impacts of climate change became one among the global concerns threatening the environment and natural resources. The fifth assessment report (AR5) of the Intergovernmental Panel on Climate Change (IPCC) reported the increase of global average temperature from 1.0°C in the lowest emission scenario to 3.7°C in the highest emission scenario by 2100 (IPCC, 2014). Climate change has an impact on the hydrological system by altering the hydrological cycle and precipitation patterns (Wang et al., 2013). The spatial and temporal patterns of precipitation are the main factors affecting flow regimes and climate conditions (Beyene et al., 2010; Wu et al., 2016). The variation of precipitation patterns would disturb the water system in the entire catchment. In Southeast Asia, the precipitation was projected to increase from 1% to 8% at the end of the 21st century (Oeurng et al., 2019). The future hydrologic system will be severely affected by climate change in the Mekong River Basin (MRB) (Lauri et al., 2012; Perera et al., 2017) and its sub-basins: the Tonle Sap Lake (Oeurng et al., 2019) and the Sekong, Sesan, and Srepok Rivers (Oeurng et al., 2016; Shrestha et al., 2016). The increment of river discharge is expected during flood season, while severe droughts are plausible to happen in the dry season (Oeurng et al., 2019). The seasonal inundation and water interchange between the Mekong River and Tonle Sap Lake of Cambodia produce high productive biodiversity, agriculture, and fisheries (Arias et al., 2013; Uk et al., 2018). The Mekong River supports about 70 million people from four countries (Cambodia, Laos PDR, Thailand, and Vietnam) in the Lower Mekong Basin (LMB) where most of the areas are prone to flooding (Try et al.,

2019). The ecosystem of the lake and its floodplain are prone to be affected by altering the hydrological cycle in the Mekong River (Arias et al., 2012).

It is a challenge to predict the change of flow regime (Bates et al., 2008). The IPCC AR5 published climate change scenarios known as the Representative Concentration Pathways (RCP) (IPCC, 2014). The RCP scenarios incorporate four emission scenarios of greenhouse gas: a stringent mitigation scenario (RCP2.6), two intermediate scenarios (RCP4.5 and RCP6.0), and one very high GHG emission scenario (RCP8.5). The future projections given by IPCC reports were based on general circulation models (GCMs) outputs. GCMs are generally capable to produce a coarse resolution that might consist of large uncertainty. Overall, downscaling approaches were taken by statistical downscaling and dynamical downscaling to produce the regional climate condition. The uncertainties of GCMs were dominantly caused by coarse resolution (Li et al., 2012). To overcome this uncertainty, this study used the outputs from two high-resolution atmospheric general circulation models (AGCMs) namely as MRI-AGCM3.2S and MRI-AGCM3.2H with 20km and 60km spatial resolution, respectively. The model performed a historical climate experiment using observed sea surface temperature, and they showed the improvement in heavy monthly-mean precipitation around the tropical pacific region confirmed by numerical skill score (Mizuta et al., 2012).

A hydrological model is an effective tool that can simulate hydrological characteristics under different scenarios. Various hydrological models were developed and applied to investigate the hydrological processes in the MRB and its tributaries: Soil and Water Assessment Tool (SWAT) model (Arnold et al., 1998), Vmod model (Koponen et al., 2010), 2-D Local Inertial Equation (2-D LIE) model (Tanaka et al., 2018), and Rainfall-Runoff-Inundation (RRI) model (Sayama et al., 2012; 2015). Try et al. (2020) used the RRI model for comparison of gridded precipitation products for flood inundation modeling in the MRB. Perera et al. (2017) applied the same model to assess the climate change impacts on hydrological analysis in the MRB using outputs from atmospheric general circulation models (AGCM) based on RCP8.5 scenario considering different sea surface temperature

(SST) boundary condition; however, their study did not consider different emission of greenhouse gas scenarios.

To further the understanding of the hydrological study of climate change impacts in the MRB, this study aims to predict the changes in extreme river discharge in the MRB and aspects of flood inundation such as inundation area, inundation volume, peak inundation duration and time, and inundation probability in the LMB by using present climate (1979–2003) and future projected climate (2075–2099) from high- and super-high-resolution AGCM models under different future projection scenarios.

5.2 Materials and Methods

5.2.1 Climate Change Datasets

The Meteorological Research Institute (MRI) developed a high-resolution (MRI-AGCM3.2H, 60km) (Mizuta et al., 2012) and a super-high-resolution atmospheric climate model (MRI-AGCM3.2S, 20km) (Kitoh and Endo, 2016; Mizuta et al., 2014) with hourly temporal scale. The climate parameters (precipitation and evapotranspiration) were used as input for the RRI model for two 25-year periods: present climate covering of 1979–2003 and the future climate (2075–2099). The MRI-AGCM3.2H model was projected from present (HPA_m01) to future climate based on the degree of GHG emission ranking from low emission (RCP2.6) to high emission (RCP8.5) namely as HFA_rcp26, HFA_rcp45, HFA_rcp60, and HFA_rcp85, respectively. The MRI-AGCM3.2S model was simulated for the present climate (1979–2003) using the observed boundary condition of SST (SPA_m01). The different SST patterns for future projection under the RCP8.5 scenario were characterized by using SST as output from 28 GCMs in Coupled Model Inter-comparison Project Phase 5 (CMIP5) (Taylor et al., 2012). The future climate experiments (2075–2099) were grouped with SST distributions into four clusters: 8-model average (uniform warming in the northern and southern hemispheres), 14-model average (El Nino-like pattern with a larger warming belt in the central equatorial Pacific), 6-model average (larger warming in the northern hemisphere than in the southern hemisphere), and total 28-model average labeled as SFA_rcp85_c1, SFA_rcp85_c2, SFA_rcp85_c3, and SFA_rcp85,

respectively. GPCC was determined to be an accurate precipitation product in the MRB region (Try et al., 2020). Therefore, this precipitation was used as a reference for bias correction as the following linear scaling method:

$$P_{hr}^{BC} = \frac{P_{mon}^{obs}}{P_{mon}^{agcm}} \times P_{hr}^{agcm} \quad (5.1)$$

where P_{mon}^{obs}: average monthly GPCC precipitation, P_{mon}^{agcm}: average monthly AGCM precipitation, P_{hr}^{agcm}: hourly AGCM precipitation, and P_{hr}^{BC}: hourly bias-corrected AGCM precipitation. The correction factor calculated from the present climate was applied to future climate experiments.

The different climate change scenarios would lead to generating different evapotranspiration (ET) in the future. For example, when precipitation increases in the future, and ET may also increase due to the increase in temperature increase. In this case, the surface runoff might not change following only precipitation change. In order to eliminate this uncertainty for future projection, the correction of future ET was calculated by extracting ET from present and future climates of AGCMs as the following equation.

$$\mathrm{ET}_{fut} = \mathrm{ET}_{JRA-55} + \Delta\mathrm{ET}_{fut} \quad (5.2)$$

where ET_{fut} is ET for each future scenario; ET_{JRA-55} is evapotranspiration from JRA–55 dataset; and $\Delta\mathrm{ET}_{fut}$is the change of ET for each future scenario comparing to their present climates.

5.2.2 RRI Model Simulation

The Rainfall-Runoff-Inundation (RRI) model was used to simulate runoff and flood inundation for the MRB. The RRI model is a two-dimensional distributed hydrodynamic model that is able to simulate rainfall-runoff and inundation processes simultaneously (Sayama et al., 2012; 2015). The slope grid cells receive rainfall and flow based on 2D diffusive wave equations, while the in-channel flow is calculated with 1D diffusive

equations. Digital elevation model (DEM), flow direction (DIR), and flow accumulation (ACC) were obtained from the Multi-Error-Removed-Improved-Terrain (MERIT DEM, Yamazaki et al., 2017) and used as input to the RRI model. The river geometry was available from the Mekong River Commission, and land use was from MODIS (product: MCD12Q1) for 2000 (Friedl et al., 2010). The simulation setting was separated into two parts. First, the model was set up with 2.5′ resolution (approx. 5 km) for the whole MRB for assessing river discharge. Then, the model was set up with 1.5′ resolution (approx. 2.7 km) for the LMB for predicting more accurate flood inundation. Try et al. (2020) evaluated the performance of five various gridded precipitation datasets for rainfall-runoff and inundation modeling over the MRB. The result showed that the Global Precipitation Climatology Centre (GPCC) product was suitable for long-term hydrological modeling in the MRB comparing to other precipitation products: APHRODITE, TRMM-3B42V7, PERSIANN-CDR, and GSMaP. Based on a retrospective experiment, this study conducted a simulation of 25 years (1982–2007) using GPCC precipitation for model verification. The surface evapotranspiration was available from the Japanese 55-year Reanalysis dataset (JRA-55) with 3-hourly and 0.5625° resolution (Kobayashi et al., 2015). The calibrated RRI model and its parameter setting (Table 5.1) were retrieved from Try et al. (2020). The performance of river discharge and flood inundation were compared between the observation and simulation results. After verification of the hydrodynamic model, the same parameter setting was used to simulate river discharge and flood inundation using the climate change dataset.

Table 5.1 The values of parameter setting of the RRI model used in the study.

Parameters			Mountains	Plains
Manning's coefficient for slope	n	($m^{-1/3}s$)	0.4	0.015
Soil depth	d	(m)	2.0	-
Lateral saturated hydraulic conductivity	k_a	(m/s)	0.1	-
Parameter of unsaturated hydraulic conductivity	β	-	9.0	-
Vertical hydraulic conductivity	k_v	(cm/h)	-	0.06
Soil porosity	φ	-	-	0.6
Wetting front soil suction head	S_f	-	-	0.273
Manning's coefficient for river	n_{river}	($m^{-1/3}s$)	0.03	

To evaluate the performance of the model, we used statistical indicators: Nash-Sutcliffe model efficiency (NSE), coefficient of determination (R^2), and root mean square error (RMSE):

$$\mathrm{NSE} = 1 - \frac{\sum(Q_{sim}(t) - Q_{obs}(t))^2}{\sum(Q_{obs}(t) - \overline{Q_{obs}})^2} \tag{5.3}$$

$$\mathrm{R}^2 = \frac{\sum((Q_{sim}(t) - \overline{Q_{sim}})(Q_{obs}(t) - \overline{Q_{obs}}))^2}{\sum(Q_{sim}(t) - \overline{Q_{sim}})^2 \sum(Q_{obs}(t) - \overline{Q_{obs}})^2} \tag{5.4}$$

$$\mathrm{RMSE} = \sqrt{\frac{\sum(Q_{sim}(t) - Q_{obs}(t))^2}{n}} \tag{5.5}$$

where $Q_{sim}(t)$ and $Q_{obs}(t)$ are the simulated and observed discharge at time step t. $\overline{Q_{sim}}$ and $\overline{Q_{obs}}$ are the simulated and observed average discharge, and n is the number of data.

5.2.3 Assessing Climate Change Impacts

In addition to assessing the impacts of climate change on extreme river flow and flood inundation in the MRB, the change of precipitation was also examined. The monthly precipitation of the projected future climate was compared with that of the present climate for the entire MRB. Next, the mean annual flow (Q_m) and the high flow exceeded 5% of the time (Q_5) were calculated. Further, the changes of inundation area and volume, flood probability, and inundation peak time and duration were also evaluated from the present period (1979–2003) to the future period (2075–2099). Moreover, the statistical Kolmogorov-Smirnov (K-S) test, a non-parametric test of two samples, was used to check the variation of flood inundation between the present and future climates. The maximum difference of the cumulative distribution function of the two samples is defined by:

$$D_{n,m} = \sup_x |F_n(x) - F_m(x)| \tag{5.6}$$

where F_n and F_m are the empirical distribution functions of the two samples, and sup is the supremum function. The null hypothesis, H_0, assumes that two samples have no significant difference in CDF. When the likelihood of the different distribution of the two samples exceeds a significance level, the null hypothesis is rejected. Two samples have different distribution if

$$D_{n,m} > c(\alpha)\sqrt{\frac{n+m}{nm}} \tag{5.7}$$

where n and m are the sample sizes. At the significance level 5% used in this study, $c(\alpha)$ is equal to 1.36.

5.3 Results

5.3.1 Performance of the Long-Term Model Simulation

The RRI model simulated for 1982–2007, the model verification period, and the performance indices of NSE, R^2, and RMSE were calculated at three stations along the mainstream of the MRB: Luang Prabang, Pakse, and Stung Treng. These three stations were selected according to the availability of observed river discharge, and their locations vary in the upper part of the LMB (i.e. Luang Prang is located near the outlet from the Upper Mekong in China), middle part (Pakse), and downstream of the LMRB (Stung Treng). Figure 5.1 showed the simulated and observed monthly discharge at the three locations. In general, the hydrographs of observation and simulation had a similar pattern for three stations; however, the model predicted underestimation in the low flow season in Luang Prabang. The evaluation statistics were NSE = 0.79. R^2 = 0.85, and RMSE = 1,371 m^3/s. At Pakse, the performance indices were NSE = 0.90, R^2 = 0.92, and RMSE = 3,433 m^3/s. The prediction at Stung Treng was high performance (NSE = 0.91, R^2 = 0.92); however, large flow at this location produced more error value (RMSE = 3,990 m^3/s) than other locations.

The performance of annual maximum flood inundation was determined using true ratio (TR) and hit ratio (HR). The observed flood extent was obtained from the NASA MODIS flood observation dataset (Nigro et al., 2014) for the period of 2000–2007. The threshold of inundation depth of 0.5 m was selected following the previous studies (Sayama et al., 2012; 2015; Try et al., 2018) to identify the flood and non-flood areas. The spatial performance index TR ranged from 0.42 to 0.82 during 2000–2007 where the average accuracy was 58% (avg. TR = 0.58). The HR indicator varied from 0.76 to 0.94, and its mean accuracy was 86% (avg. HR = 0.86). The uncertainty in inundation accuracy was discussed in Chapter 4 (Section 4.3.1. Long-term model validation).

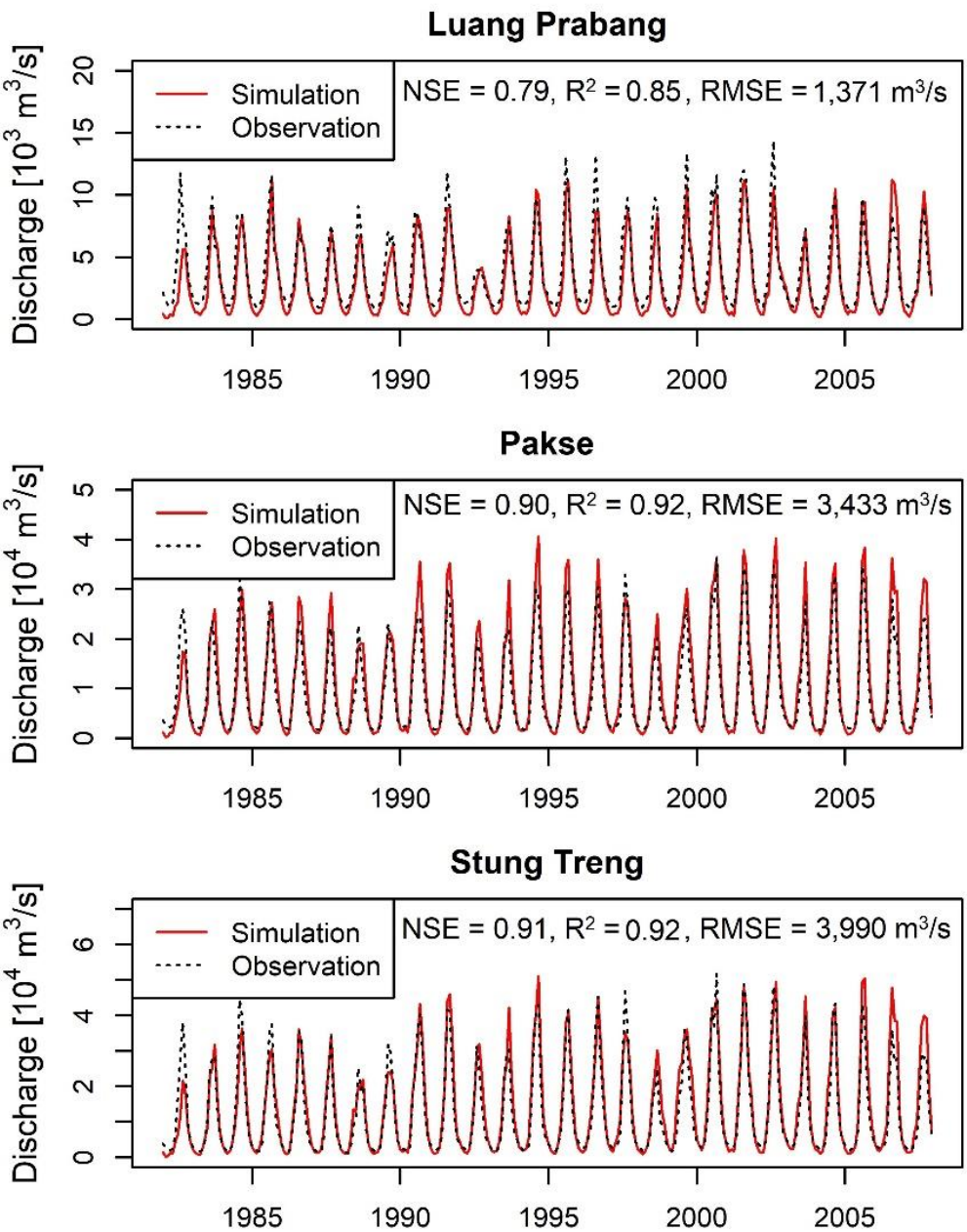

Figure 5.1 Monthly simulated and observed discharges at Luang Prabang, Pakse, and Stung Treng for the period of 1982–2007. Model performance for river discharge was evaluated by Nash–Sutcliffe efficiency (NSE), coefficient of determination (R^2), and root mean square error (RMSE).

5.3.2 Precipitation Changes

The bias correction performance was checked by comparing the precipitation and simulated discharge of historical AGCMs before and after bias correction. Figure 5.2 shows average daily precipitation and simulated discharge comparing between GPCC and AGCMs before and after bias correction. The raw precipitation and discharge had seasonal bias (i.e. overestimation) at the beginning of the wet season. The performance of average daily AGCM precipitation before and after bias correction was improved with R^2 from 0.85 to 0.94 for SPA_m01 and from 0.87 to 0.93 for HPA_m01, respectively. Moreover, the performance discharge was improved from R^2 = 0.89 and 0.96 to R^2 = 0.99 and 0.98 for SPA_m01 and HPA_m01, respectively.

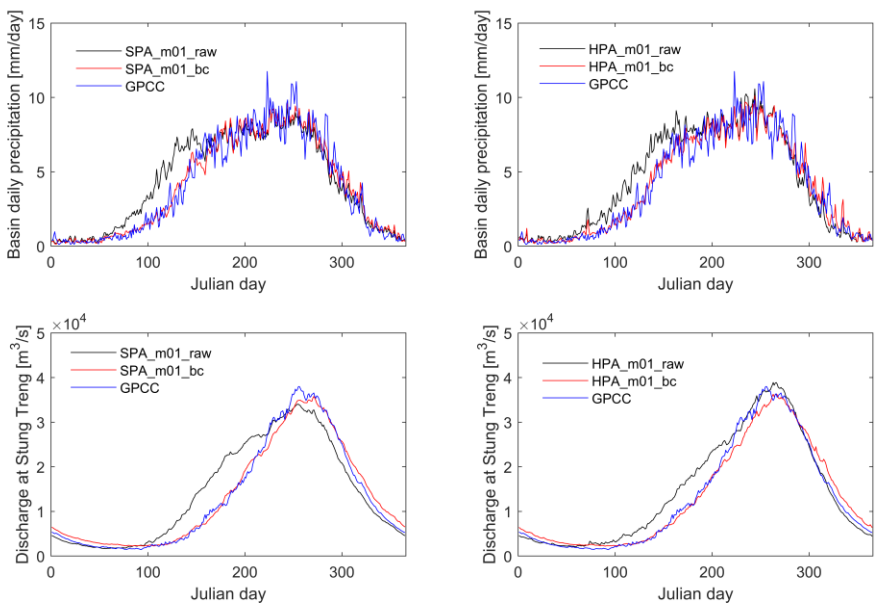

Figure 5.2 Comparison of raw and bias-corrected average daily precipitation and discharge at Stung Treng for historical AGCMs (SPA_m01 and HPA_m01) with GPCC simulation.

Figure 5.3 showed the bias-corrected monthly precipitation from MRI-AGCM3.2H and MRI-AGCM3.2S datasets in the present (1979–2003) and future (2075–2099) climates.

The basin average precipitation was expected to increase for RCP and SST scenarios during the rainy season (May–October). During the late rainy season in September, the precipitation of future scenarios of HFA_rcp45, HFA_60, and HFA_rcp85 significantly raised up while less increase could be observed in HFA_rcp26. Three future SST patterns (SFA_rcp85, SFA_c2, and SFA_c3) provided a higher increase of precipitation than SFA_rcp85_c1 in the rainy season compared to their present climate SPA_m01. The annual precipitation would increase by 6.6%, 8.0%, 9.5%, and 14.2% for four RCP scenarios (RCP2.6–RCP8.5), and four SST pattern scenarios had less diversified increasing (9.9–12.5%).

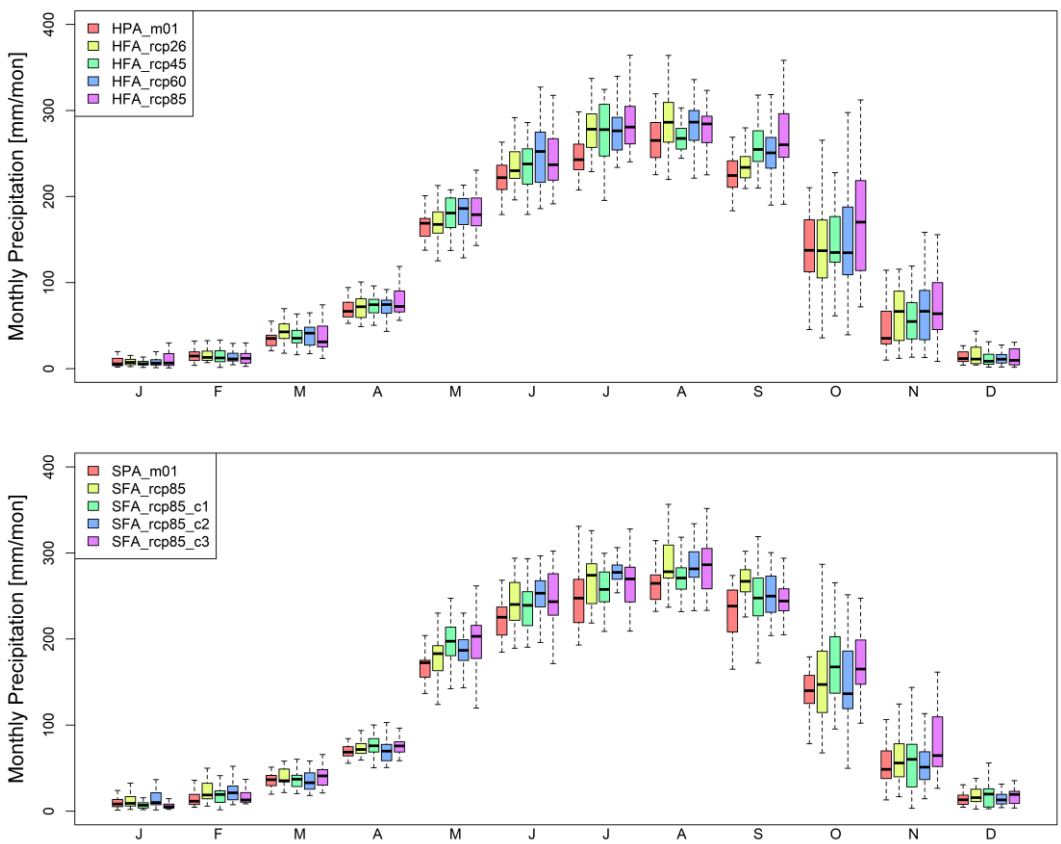

Figure 5.3 Bias corrected monthly precipitation in the present and future climate experiments of MRI-AGCM3.2H and MRI-AGCM3.2S models. The bottom and top of

the box show first and third quartiles, and the flat line inside the box is the median. The whiskers represent the minimum and maximum values.

5.3.3 Effects of Climate Change on River Flow

The future changes in river discharge were assessed by simulation of RRI model using precipitation and evapotranspiration projected by MRI-AGCM3.2H and MRI-AGCM3.2S models from present climate (1979–2003) to the future climate (2075–2099) for four greenhouse gas emission scenarios (RCP2.6, RCP4.5, RCP6.0, and RCP8.5) and four SST scenarios (Figure 5.4). The flow change was examined at four locations along the mainstream of the MRB. Table 5.2 showed the mean annual discharge (Q_m) and extreme river flow exceeding 5% of the time (Q_5). Overall, Q_m and Q_5 increased for all future scenarios. The Qm of the upstream stations (Chiang Saen and Vientiane) was predicted to increase by 5–10% while the downstream stations (Pakse and Kratie) raised up a higher increment of 10–15% for three climate change scenarios (RCP2.6, RCP4.5, and RCP6.0). The Qm for all stations significantly escalated for RCP8.5 (23–26%) and SST scenarios (10±3% – 29±3%). At the end of the 21st century, high flow (Q_5) showed increases of 5–14% at Chiang Saen and Vientiane and 11–18% at Pakse and Kratie for the three low emission scenarios (RCP2.6, RCP4.5, and RCP6.0). The Q_5 momentously stepped up to 21–30% for four observing stations for RCP8.5 while it ranged between 10±4% and 18±3% for the SST scenario. The peak discharge took place in September (Figure 5.4), and this remained the same for all future scenarios at Vientiane, Pakse, and Kratie except Chiang Saen where the peak discharge from SST somehow happened earlier in August.

Table 5.2 Changes (%) of annual mean discharge (Q_m) and flow exceeded 5% of the time (Q_5) for RCP and SST scenarios compared to the present climate. The values for SST scenarios show mean (μ) ± standard deviation (σ).

Station	Scenario	Q_m	Q_5
Chiang Saen	RCP2.6	+6%	+9%
	RCP4.5	+9%	+10%
	RCP6.0	+5%	+14%
	RCP8.5	+23%	+27%
	SST (μ±σ)	+10±3%	+10±4%
Vientiane	RCP2.6	+7%	+5%
	RCP4.5	+10%	+8%
	RCP6.0	+7%	+10%
	RCP8.5	+23%	+21%
	SST (μ±σ)	+11±2%	+10±4%
Pakse	RCP2.6	+10%	+11%
	RCP4.5	+13%	+11%
	RCP6.0	+13%	+17%
	RCP8.5	+26%	+29%
	SST (μ±σ)	+25±3%	+16±4%
Kratie	RCP2.6	+12%	+14%
	RCP4.5	+13%	+13%
	RCP6.0	+15%	+18%
	RCP8.5	+25%	+30%
	SST (μ±σ)	+29±3%	+18±3%

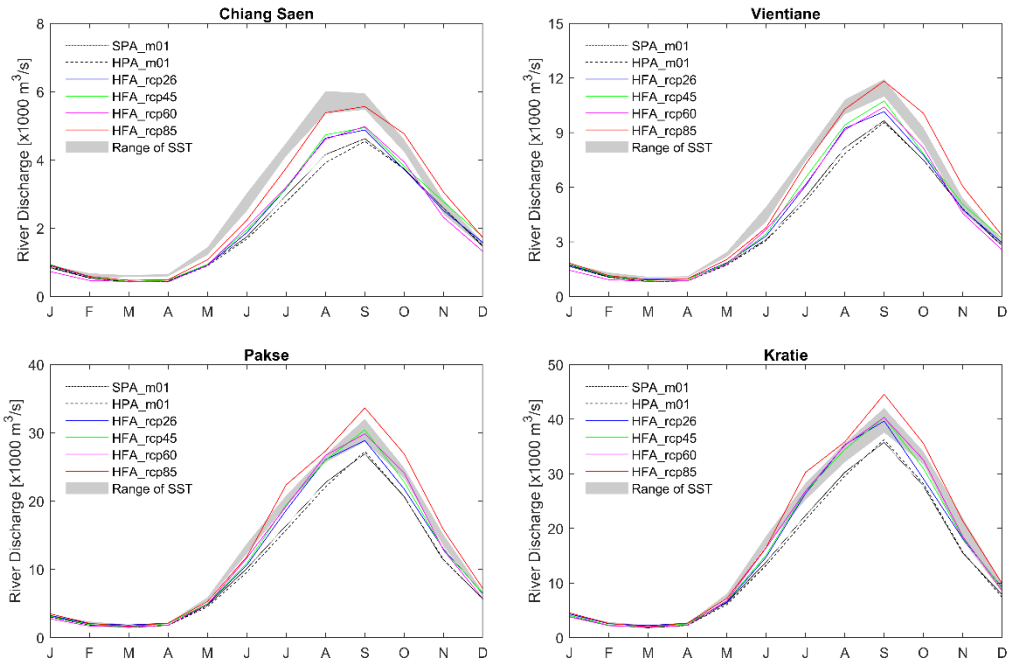

Figure 5.4 Monthly flow for present climate (HPA) comparing with each projected future climate RCP scenarios (HFA) and different sea surface temperature scenarios (SST).

5.3.4 Effect of Climate Change on Flood Inundation

The flood plain and agricultural land are the majority in the LMB, so the threshold was selected at 0.5 m of water depth to classify the inundated and non-inundated area. According to the simulation results, flood magnitudes were expected to increase for all future scenarios. Figure 5.5 showed the 25-year average inundation extent in the present and future climatic conditions. The ratios of mean and variance of the inundation extent of the future and present were 1.19–1.43 and 2.08–3.92 for MRI-AGCM3.2H and 1.26–1.32 and 1.12–2.13 for MRI-AGCM3.2S (Table 5.3), respectively. Figure 5.6 showed boxplot comparison of peak inundation time (days of the year, DOY) and inundation volume in the LMB. There was no significant change of peak flood time of future climate compared to the present climate (i.e. the variation of the median was within ±5 days). The K-S test showed result of no significant difference for all future scenarios (RCP and SST) at significant level 5% (p-value = 0.2370–0.8774). The peak inundation volume took place in

October for the present climate and all projected future scenarios. However, there was a huge variability in peak inundation volume. The first quartile values of the LMB peak inundation volume (the boxplot in the lower row of Figure 5.6) for all future scenarios (100–124km^3 for HFA and 99–118km^3 for SFA) were greater than the third quartile value of their present climates (99 km^3 and 98 km^3 for HPA and SPA). Median of peak inundation volume for HFA increased between 15% for RCP2.6 to 42% for RCP8.5 and 28–41% for SST. The relative ratio of the mean of inundation volume varied between 1.24–1.55 and 1.29–1.41, and the relative ratio of inundation volume variance changed from 2.30 to 4.60 and from 1.66 to 2.09 (Table 5.3) for RCP and SST scenarios, respectively. The result of K-S test of peak inundation volume revealed a significant difference for all RCP and SST scenarios (i.e. null hypothesis was rejected at a significant level of 5% with p-value less than 0.002).

Table 5.3 The ratio (F) of mean (μ) and variance (σ^2) of inundation area and volume for future climates comparing their present climate.

Model	Scenario	Inundation area		Inundation volume	
		F(μ)	F(σ^2)	F(μ)	F(σ^2)
MRI-AGCM3.2H	HFA_rcp26	1.19	2.28	1.24	2.68
	HFA_rcp45	1.26	2.08	1.32	2.30
	HFA_rcp60	1.32	3.92	1.41	4.60
	HFA_rcp85	1.43	3.37	1.55	3.96
	avg.	1.30	2.91	1.38	3.38
MRI-AGCM3.2S	SFA_rcp85	1.32	1.12	1.41	1.66
	SFA_ rcp85_c1	1.26	2.13	1.29	1.98
	SFA_ rcp85_c2	1.32	1.67	1.38	2.09
	SFA_ rcp85_c3	1.27	2.08	1.30	1.89
	avg.	1.29	1.75	1.34	1.90

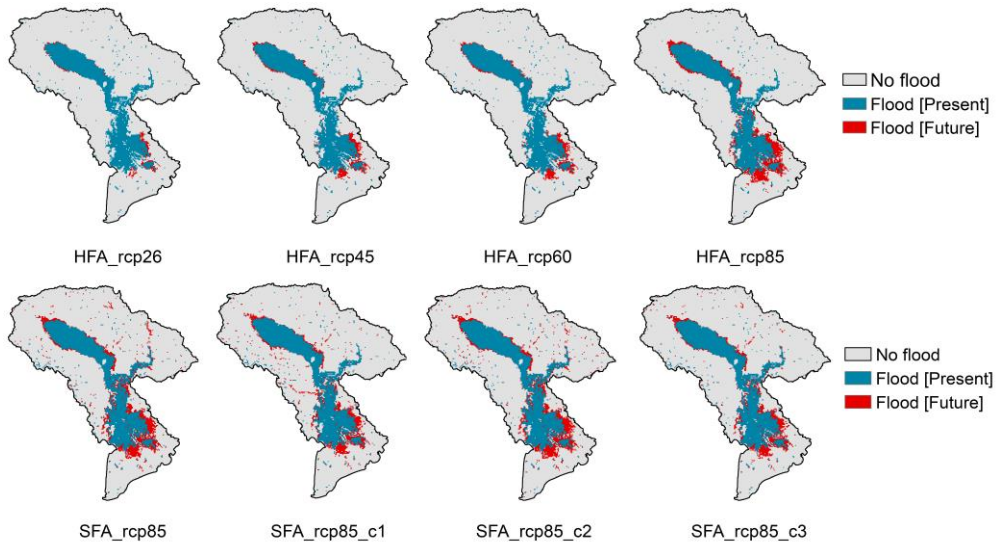

Figure 5.5 25-year average of annual maximum inundation extent for the present and the future climate experiments.

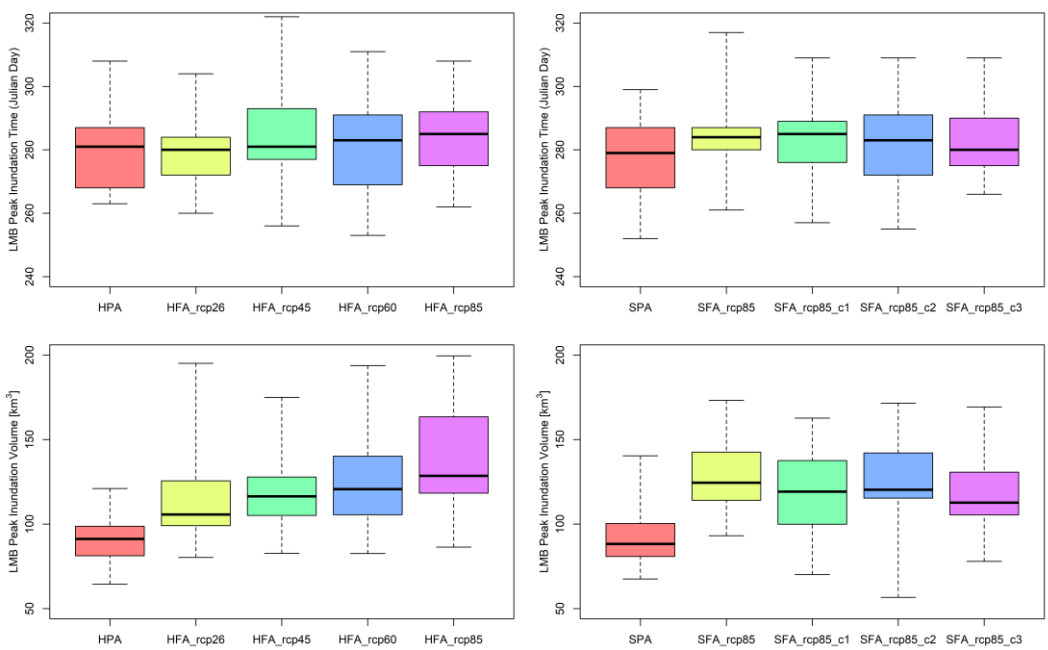

Figure 5.6 Peak inundation time (upper row) and peak inundation volume (lower row) in the LMB resulted from MRI-AGCM3.2H model (left column) and MRI-AGCM3.2S model (right column). The boxplot explanation is the same as Figure 5.3.

Figures 5.7 and 5.8 showed the flood inundation probability, the difference of probability of flood inundation from the present to future (dP), and the K-S test result for each climate model. The dP clearly indicated the positive value for all projected future scenarios. For MRI-AGCM3.2H, the dP ranged within one less increase (HFA_rcp26), two medium increases (HFA_rcp45 and HFA_rcp60), and one large increase (HFA_rcp85). Among the area of significant difference of inundation probability ($dP \geq 0.05$ in Figures 5.7 and 5.8), the proportion for area $dP \geq 0.3$ was only 12% (i.e. area of proportion $0.05 \leq dP < 0.03$ was 88%) for RCP2.6, and this proportion raised up to 48%, 40%, 56% for HFA_rcp45, HFA_rcp60, and HFA_rcp85. On the other hand, the same proportion value of $dP \geq 0.3$ had less diversification (i.e. 54–62%) for ranges of SST scenarios. The spatial K-S test indicated almost no significance in HFA_rcp26 and partial significant in HFA_rcp45 and HFA_rcp60 while large area was found significance in HFA_rcp85. The K-S test for SST patterns determined significance at the most area in SFA_rcp85 following by SFA_rcp85_c3, and SFA_rcp85_c2 and SFA_rcp85_c1 had less area of significance.

The inundation duration, change of duration, and its spatial K-S test results were illustrated in Figures 5.9 and 5.10 for MRI-AGCM3.2H and MRI-AGCM3.2S, respectively. The variation of inundation duration per 25-year in the present and future between -1 and 1 day was considered as no change in this study. Overall, the longer durations of inundation were observed for the LMB for both RCP and SST scenarios. The area with high flood inundation probability commonly experienced long flood durations while the low probability place corresponded with a shorter duration of inundation. Similarly, the spatial K-S test showed significance in most areas regardless of RCP and SST scenarios. The increase of flood duration was observed at the floodplain except inside the Tonle Sap Lake where the water exists for the whole year.

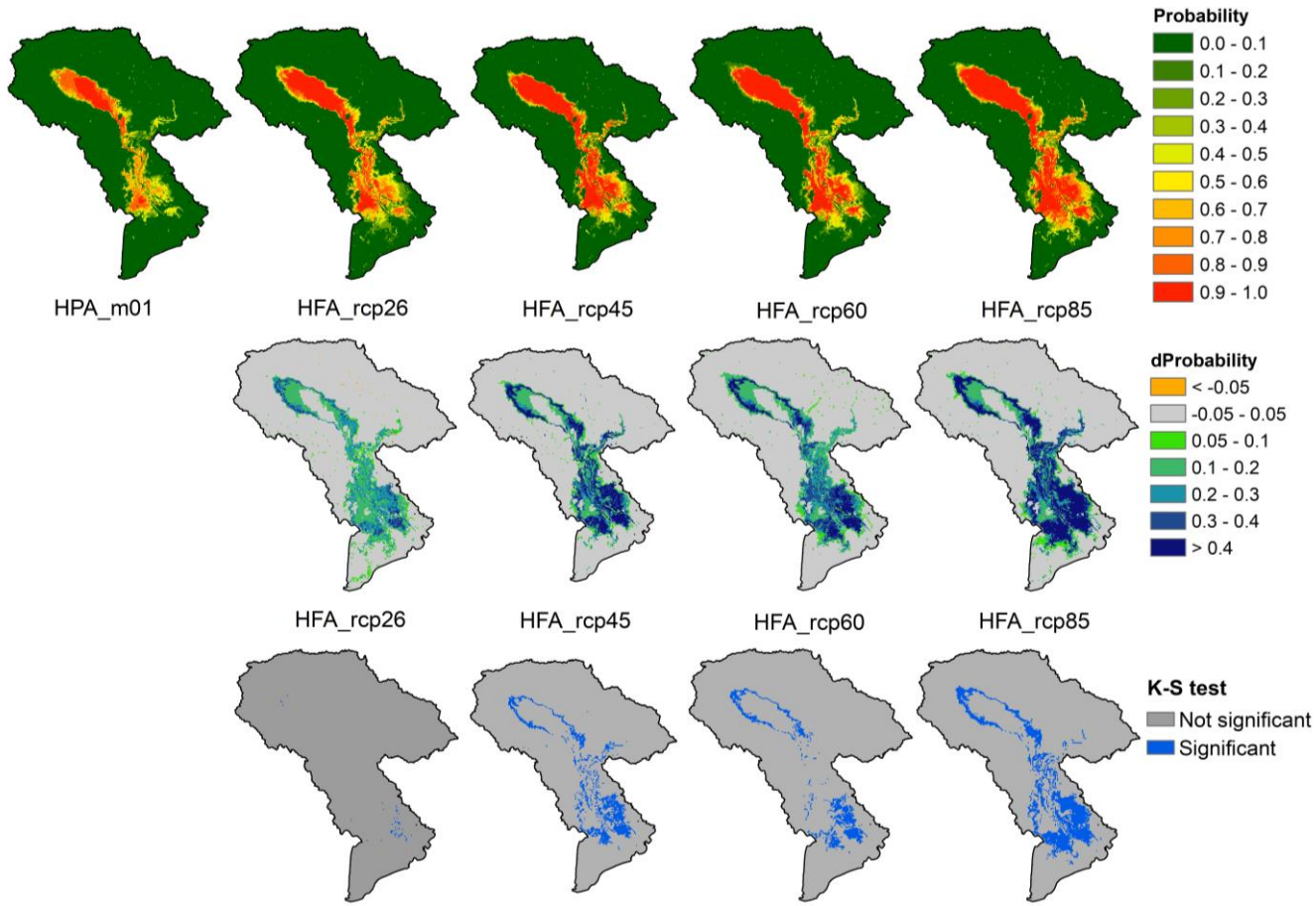

Figure 5.7 Spatial distribution of inundation probability (upper row), difference between present and future RCP scenarios (middle row), and K-S test (lower row) for MRI-AGCM3.2H model.

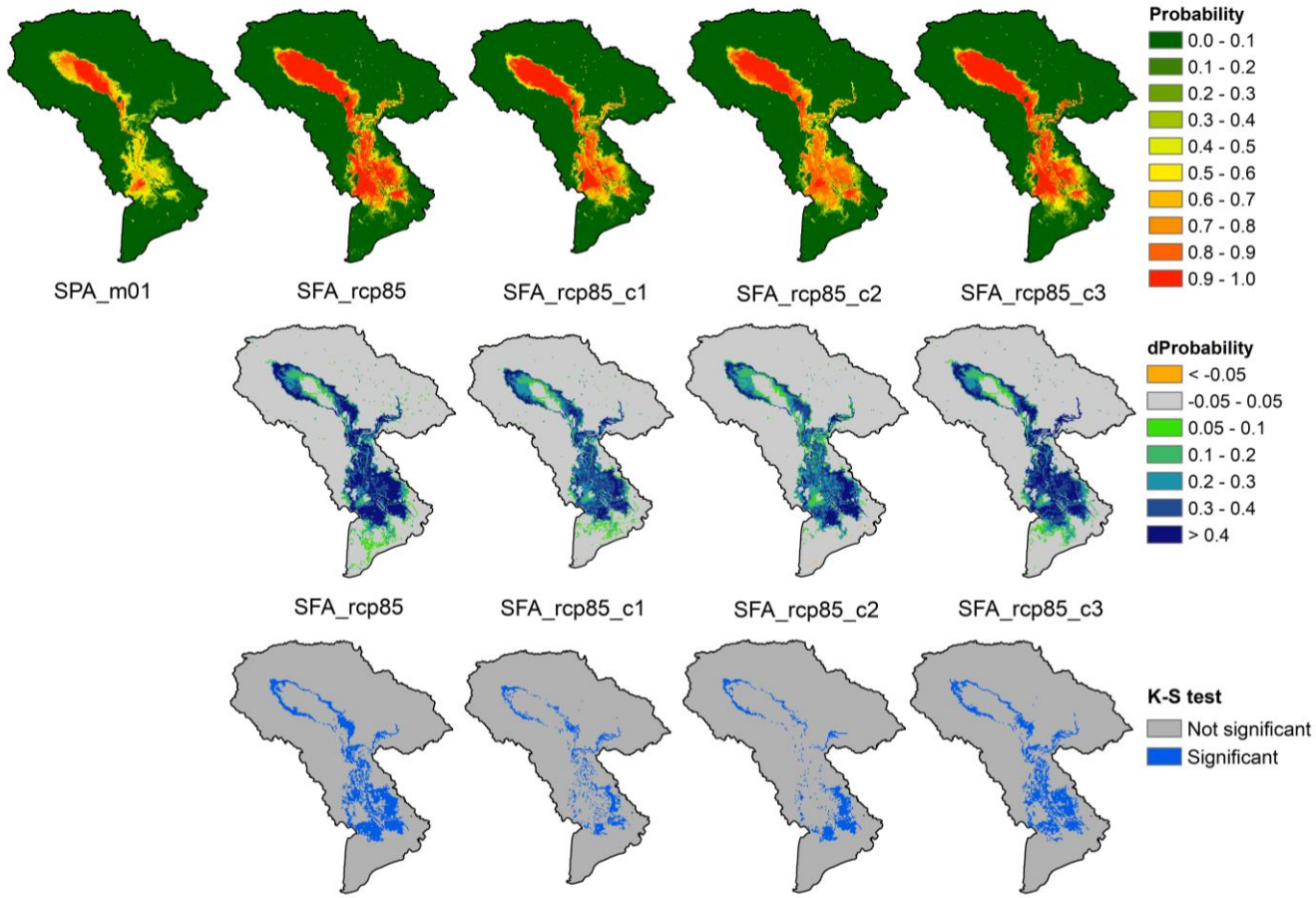

Figure 5.8 Spatial distribution of inundation probability (upper row), difference between present and future SST scenarios (middle row), and K-S test (lower row) for MRI-AGCM3.2S model.

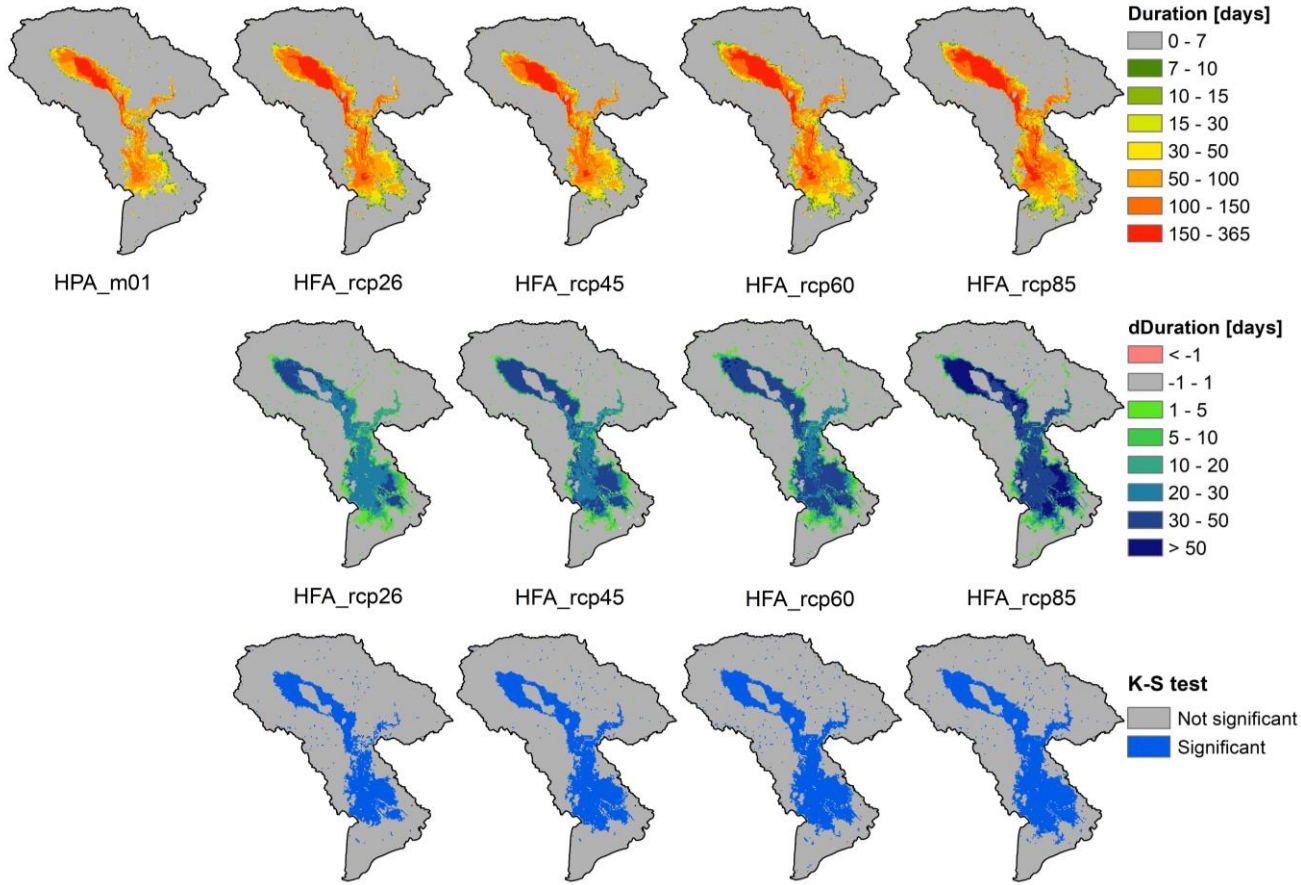

Figure 5.9 Spatial distribution of inundation duration (upper row), difference between present and future RCP scenarios (middle row), and K-S test (lower row) for MRI-AGCM3.2H model.

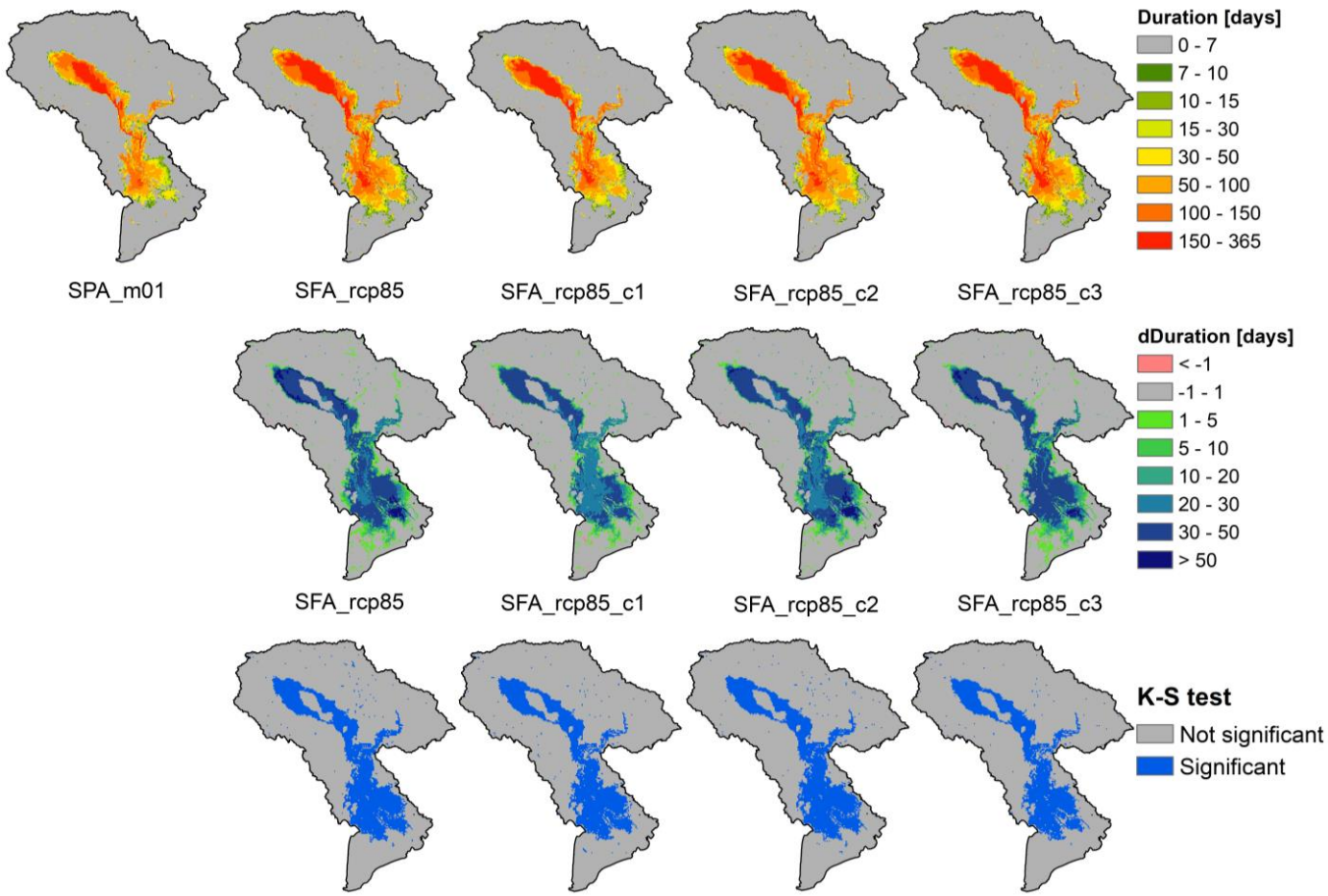

Figure 5.10 Spatial distribution of inundation duration (upper row), difference between present and future SST scenarios (middle row), and K-S test (lower row) for MRI-AGCM3.2S model.

5.4 Discussion

5.4.1 Benefits of High-resolution Data

This study used two high-resolution models MRI-AGCM3.2H and MRI-AGCM3.2S with a spatial resolution of 60 km and 20 km. To see the benefits of fine spatial-scale, two other coarse-resolution GCMs (MRI-CGCM3 and MRI-ESM1) from the CMIP5 were examined to compare their performance without bias correction for 25-year in the historical climate (1979–2003). The grid resolutions of MRI-CGCM3 and MRI-ESM1 are 125 km × 125 km. Figure 5.11 showed the comparison of the spatial distribution of annual average precipitation of GPCC and the four models over the MRB region. The two high-resolution AGCMs (MRI-AGCM3.2H and MRI-AGCM3.2S) used in this showed a similar distribution while the two coarse resolution models (MRI-CGCM3 and MRI-ESM1) indicated a large error, particularly in the area close to the coast. This was the advantage of using observed SST as a boundary condition in AGCM; however, GCMs were not able to consider this effect.

In addition, basin monthly precipitation was also compared between GPCC and four climate models without bias correction. Figure 5.12 showed the similarity of violin shapes between GPCC and two high-resolution AGCMs (MRI-AGCM3.2H and MRI-AGCM3.2S). The mean values range between 131–137 mm for AGCMs and 119–113 mm for GCMs comparing to 126 mm of GPCC. The MRI-CGCM3 and MRI-ESM1 models produced precipitation at more spread density (i.e. their median is at a very low value, and top height of violin is overestimated) comparing to GPCC. Overall, two high-resolution AGCMs used in this study performed better than two GCMs in CMIP5 in terms of spatial and monthly precipitation in the MRB region.

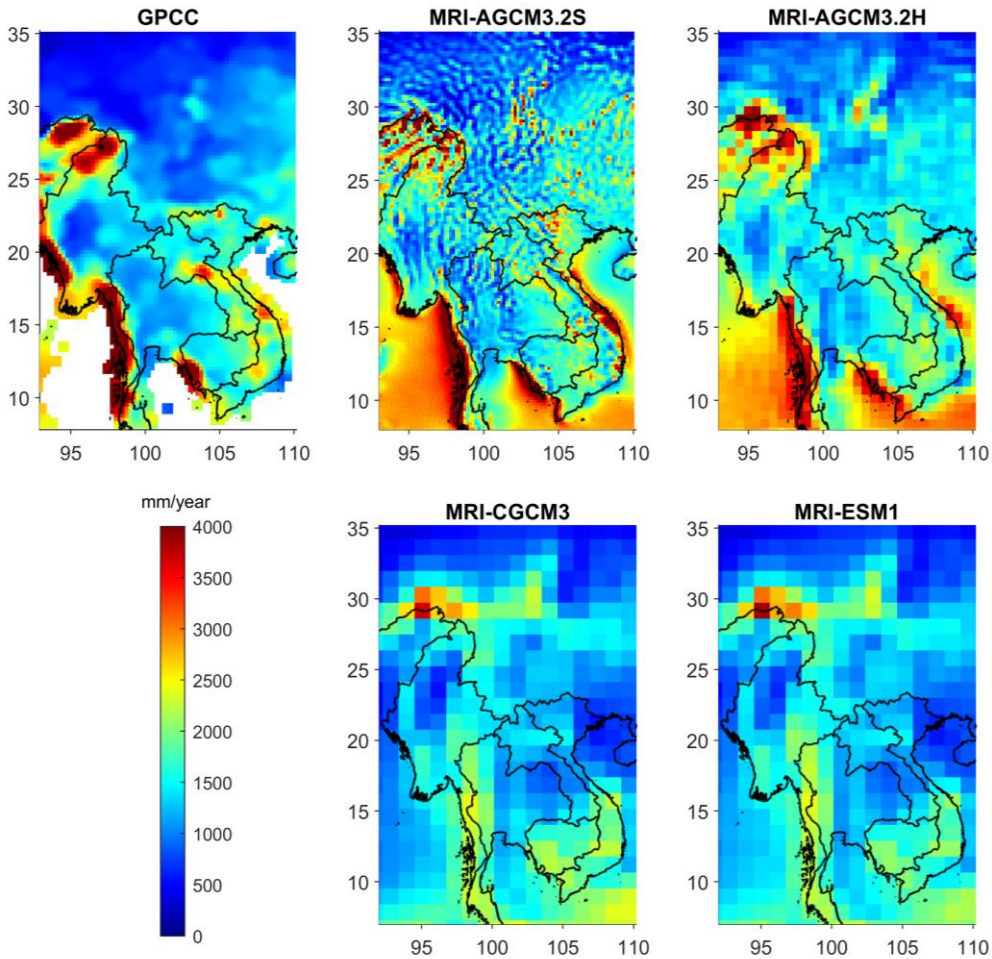

Figure 5.11 Spatial distribution of annual precipitation of GPCC and four climate models (MRI-AGCM-3.2S, MRI-AGCM3.2H, MRI-CGCM3, and MRI-ESM1).

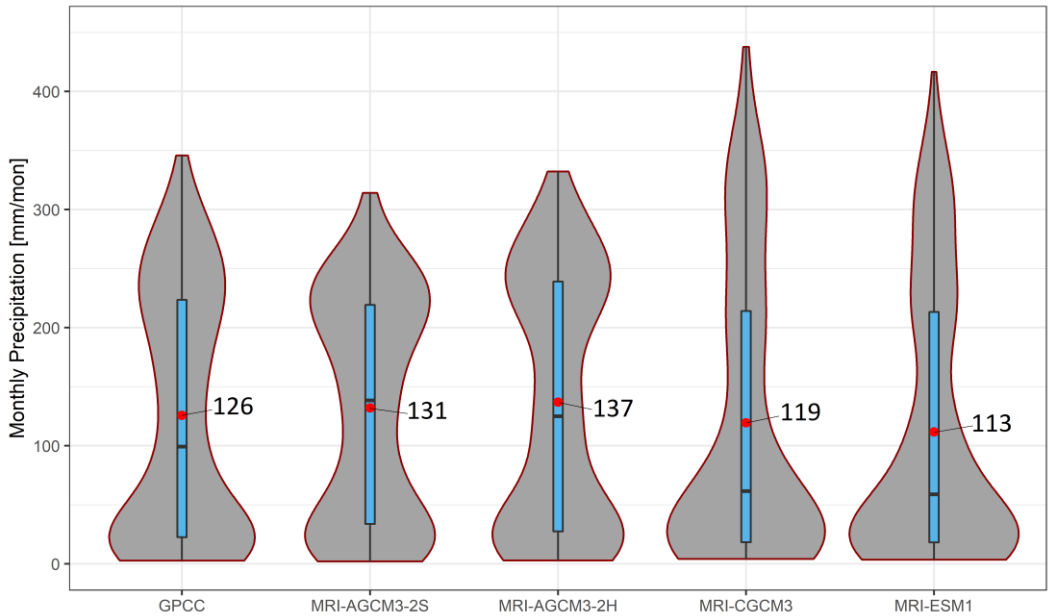

Figure 5.12 Violin plot and boxplot of monthly basin average precipitation of GPCC and four AGCM and GCM models. The red circle and black dots represent mean and median. The side of violin shows the density distribution of data samples.

5.4.2 Implementation of Climate Change Impacts

The results from this study clearly indicated that the river discharge and flood inundation in the MRB were significantly affected by climate change impacts. The simulation results of climate change revealed that flood inundation magnitude in the future in the LMB would be severer than the present climate. The increasing of annual precipitation (6.6–14.2%) could force to enlarge the extreme high flow (Q_5) at the LMB (increasing 13–30% at Kratie) and lead to increase excessive inundation in the LMB up to 19–43% for inundation area and 24–55% for inundation volume. Lauri et al. (2012) determined the change in discharge at Kratie from -10.6 to +13.4% for A1B scenario (comparable to RCP6.0) and between -6.9 and +8.1% for B1 scenario (comparable to RCP4.5) using five GCMs from baseline (1982–1992) to projected period (2032–2042). Västilä et al. (2010) projected annual maximum flooded area in the LMB flood pulse for 2010–2049 by changing between -3% and 14% in for A2 emission scenario (comparable to RCP8.5). Perera et al. (2017) found

out the increasing discharge volume of 25% at Kratie in RCP8.5 scenario. Shrestha et al. (2016) analyzed the uncertainty sources of climate change on river flow in the Sekong, Sesan, and Srepok (3S) Rivers, one of the main tributary of the MRB, using three GCMs (GISS, GFDL, and IPSL) and revealed the results that peak flow was likely to increase ranging from 54.1% for RCP2.6 to 78.9% for RCP8.5 for the 2060s. The assessment results of climate change impacts on hydrological extreme flows in 11 sub-basins of the Tonle Sap Lake by Oeurng et al. (2019) using three GCM models (GFDL-CM3, GISS-E2-R-CC, and IPSL-CM5A-MR) for three projected time horizons (2030s, 2060s, and 2090s) under RCP6.0 scenario revealed that most sub-basins of the Tonle Sap basin would face more extreme drought than flooding.

In addition to the findings of Perera et al. (2017) studied flood inundation under SST patterns in the LMB, this study found the significant increment of flood inundation area and volume on various projected future climate change including 4 RCP scenarios and 4 different SST patterns scenarios. More importantly, further analysis of increasing changes in flood inundation duration and probability was significantly determined in this study while the flood peak time would be no substantial variation.

5.4.3 Limitations

However, the limitation of this study was assessing only output from MRI-AGCM3.2H and MRI-AGCM3.2S. Considering more high-resolution GCMs would provide more reliability for future prediction of flood inundation. Plus, due to the limited capacity of long-term and large-scale simulation, the spatial resolution of the inundation simulation in this study was taken 1.5′ (approx. 2.7 km); therefore, the finer resolution was able to provide more accurate results. Furthermore, the water for urban water supply, irrigation, and power generation purposes was not carried out in this study. The land-use map was taken from MODIS (year: 2000) considered as static from the present to the future. The rapid development would affect the uncertainty in the prediction. The potential effect of land-use change should be considered in future studies in the MRB.

5.5 Summary

This chapter presented the effects of climate change on flow in the MRB and inundation in the LMB from the present period (1979–2003) to the future period (2075–2099). This study compared the extreme river flow, peak inundation area, peak inundation time and volume, flood probability, and inundation duration. The analysis was conducted based on bias-corrected precipitation and evapotranspiration which were outputs from two high-resolution atmospheric models (MRI-AGCM3.2H 60km and MRI-AGCM3.2S 20km). The result indicated that the extreme river flow and extreme flood inundation will be severer and higher magnitude at the end of the 21st century for all future scenarios (RCP and SST). However, flood peak time was observed with no significant variation. The area with a long flood duration corresponded with a high probability of flood inundation. This study provided additional information about climate change impacts on flood inundation for further understanding and preparing for climate change adaptation as well as flood damage reduction strategies in the LMB.

References

Arias, M. E., Cochrane, T. A., Piman, T., Kummu, M., Caruso, B.S, and Killeen, T.J. (2012). Quantifying changes in flooding and habitats in the Tonle Sap Lake (Cambodia) caused by water infrastructure development and climate change in the Mekong Basin. *Journal of Environmental Management*, 112: 53-66. doi: 10.1016/j.jenvman.2012.07.003.

Arias, M. E., Cochrane, T. A., Norton, D., Killeen, T. J., and Khon, P. (2013). The flood pulse as the underlying driver of vegetation in the largest wetland and fishery of the Mekong Basin. *Ambio*. 42(7): 864-76. doi: 10.1007/s13280-013-0424-4.

Arnold, J. G., Srinivasan, R., Muttiah, R. S., and Williams, J. R. (1998). Large area hydrologic modeling and assessment part I: model development. *Journal of the American Water Resources Association*, 34(1): 73-89. doi: 10.1111/j.1752-1688.1998.tb05961.x.

Bates, B. C., Kundzewicz, Z. W., Wu, S., and Palutikof, J. P. (2008). Climate Change and Water. IPCC Technical Paper IV. Intergovernmental Panel on Climate Change, Geneva.

Beyene, T., Lettenmaier, D. P., and Kabat, P. (2010). Hydrologic impacts of climate change on the Nile River Basin: implications of the 2007 IPCC scenarios. *Climatic change*, 100(3-4): 433-461. doi: 10.1007/s10584-009-9693-0.

Friedl, M. A., Sulla-Menashe, D., Tan, B., Schneider, A., Ramankutty, N., Sibley, A., and Huang, X. (2010). MODIS Collection 5 global land cover: Algorithm refinements and characterization of new datasets. *Remote sensing of Environment*, 114(1): 168-182. doi: 10.1016/j.rse.2009.08.016.

Intergovernmental Panel on Climate Change (IPCC) (2014). Sythesis Report. Contribution of Working Groups I, II and III to the Fifth Assessment Report of the IPCC, Geneva, Switzerland.

Kitoh, A., and Endo, H. (2016). Changes in precipitation extremes projected by a 20-km mesh global atmospheric model. *Weather and Climate Extremes*, 11: 41-52. doi: 10.1016/j.wace.2015.09.001.

Kobayashi, S., Ota, Y., Harada, Y., Ebita, A., Moriya, M., Onoda, H., Onogi, K., Kamahori, H., Kobayashi, C., Endo, H., Miyaoka, K., and Takahashi, K. (2015). The JRA-55 Reanalysis: General specifications and basic characteristics. *J. Meteor. Soc. Japan*, 93: 5-48. doi: 10.2151/jmsj.2015-001.

Koponen, J., Lauri, H., Veijalainen, N., and Sarkkula, J. (2010). HBV and IWRM watershed modelling user guide. MRC Information and Knowledge Management Programme, DMS—Detailed Modelling Support for the MRC Project.

Lauri, H., Moel, H. D., Ward, P., Räsänen, T., Keskinen, M., and Kummu, M. (2012). Future changes in Mekong River hydrology: impact of climate change and reservoir operation on discharge. *Hydrology and Earth System Sciences*, 16: 4603-4619. doi: 10.5194/hess-16-4603-2012.

Li, G., Zhang, X., Zwiers, F., and Wen, Q. H. (2012). Quantification of uncertainty in highresolution temperature scenarios for North America. *Journal of Climate*, 25(9): 3373-3389. doi: 10.1175/JCLI-D-11-00217.1.

Mizuta, R., Yoshimura, H., Murakami, H., Matsueda, M., Endo, H., Ose, T., Kamiguchi, K., Hosaka, M., Sugi, M., Yukimoto, S., Kusunoki, S., and Kitoh, A. (2012). Climate simulations using MRI-AGCM3.2 with 20-km grid. *Journal of the Meteorological Society of Japan*. 90: 233-258. doi: 10.2151/jmsj.2012-A12.

Mizuta, R., Arakawa, O., Ose, T., Kusunoki, S., Endo, H., and Kitoh, A. (2014). Classification of CMIP5 future climate responses by the tropical sea surface temperature changes. *Sola*, 10: 167-71. doi: 10.2151/sola.2014-035.

Nigro, J., Slayback, D., Policelli, F., and Brakenridge, G. R. (2014). NASA/DFO MODIS near real-time (NRT) global flood mapping product evaluation of flood and permanent water detection. Evaluation, Greenbelt, MD.

Oeurng, C., Cochrane, T. A., Arias, M. E., Shrestha, B., and Piman, T. (2016). Assessment of changes in riverine nitrate in the Sesan, Srepok and Sekong tributaries of the Lower Mekong River Basin. *Journal of Hydrology: Regional Studies*, 8: 95-111. doi: 10.1016/j.ejrh.2016.07.004.

Oeurng, C., Cochrane, T. A., Chung, S., Kondolf, M. G., Piman, T., Arias, M. E. (2019). Assessing Climate Change Impacts on River Flows in the Tonle Sap Lake Basin, Cambodia. *Water*, 11(3): 618. doi: 10.3390/w11030618.

Perera, E., Sayama, T., Magome, J., Hasegawa, A., and Iwami, Y. (2017). RCP8.5-Based future flood hazard analysis for the lower Mekong river Basin. *Hydrology*, 4(4): 55. doi: 10.3390/hydrology4040055.

Sayama, T., Ozawa, G., Kawakami, T., Nabesaka, S., and Fukami, K. (2012). Rainfall–runoff–inundation analysis of the 2010 Pakistan flood in the Kabul River basin. *Hydrological Sciences Journal*, 57(2): 298-312. doi: 10.1080/02626667.2011.644245.

Sayama, T., Tatebe, Y., Iwami, Y., and Tanaka, S. (2015). Hydrologic sensitivity of flood runoff and inundation: 2011 Thailand floods in the Chao Phraya River basin. *Nat. Hazards Earth Syst. Sci*., 15: 1617–1630. doi: 10.5194/nhess-15-1617-2015.

Shrestha, B., Cochrane, T. A., Caruso, B. S., Arias, M. E., Piman, T. (2016). Uncertainty in flow and sediment projections due to future climate scenarios for the 3S Rivers in the Mekong Basin. *Journal of Hydrology*, 540: 1088-1104. doi: 10.1016/j.jhydrol.2016.07.019.

Tanaka, T., Yoshioka, H., Siev, S., Fujii, H., Fujihara, Y., Hoshikawa, K., Ly, S., and Yoshimura, C. (2018). An Integrated Hydrological-Hydraulic Model for Simulating Surface Water Flows of a Shallow Lake Surrounded by Large Floodplains. *Water*, 10(9): 1213. doi: 10.3390/w10091213.

Taylor, K. E., Stouffer, R. J., and Meehl, G. A. (2012). An overview of CMIP5 and the experiment design. *Bulletin of the American Meteorological Society*, 93(4):485-98.

Try, S., Lee, G., Yu, W., Oeurng, C., and Jang, C. (2018). Large-Scale Flood-Inundation Modeling in the Mekong River Basin. *Journal of Hydrologic Engineering*, 23(7): 05018011. doi: 10.1061/(ASCE)HE.1943-5584.0001664.

Try, S., Lee, G., Yu, W., and Oeurng, C. (2019). Delineation of flood-prone areas using geomorphological approach in the Mekong River Basin. *Quaternary International*, 503: 79-86. doi: 10.1016/j.quaint.2018.06.026.

Try, S., Tanaka, S., Tanaka, K., Sayama, T., Oeurng, C., Uk, S., Takara, K., Hu, M., and Han, D. (2020). Comparison of Various Gridded Precipitation Datasets for RainfallRunoff and Inundation Modeling in the Mekong River Basin. *Plos One*, 15(1). doi: 10.1371/journal.pone.0226814.

Uk, S., Yoshimura, C., Siev, S., Try, S., Yang, H., Oeurng, C., Li, S., and Hul, S. (2018). Tonle Sap Lake: Current status and important research directions for environmental management. *Lakes & Reservoirs: Research & Management*, 23(3): 177-189. doi: 10.1111/lre.12222.

Västilä, K., Kummu, M., Sangmanee, C., and Chinvanno, S. (2010). Modelling climate change impacts on the flood pulse in the Lower Mekong floodplains. *Journal of Water and Climate Change*, 1(1): 67-86. doi: 10.2166/wcc.2010.008.

Wang, S., Jiao, S., and Xin, H. (2013). Spatio-temporal characteristics of temperature and precipitation in Sichuan Province, Southwestern China, 1960–2009. *Quaternary International*, 286: 103-115. doi: 10.1016/j.quaint.2012.04.030.

Wu, F., Wang, X., Cai, Y., and Li, C. (2016). Spatiotemporal analysis of precipitation trends under climate change in the upper reach of Mekong River basin. *Quaternary international*, 392: 137-146. doi: 10.1016/j.quaint.2013.05.049.

Yamazaki, D., Ikeshima, D., Tawatari, R., Yamaguchi, T., O'Loughlin, F., Neal, J. C., Sampson, C. C., Kanae, S., Bates, P. D. (2017). A high accuracy map of global terrain elevations. *Geophysical Research Letters*, 44: 5844-5853. doi: 10.1002/2017GL072874.

CHAPTER 6 Evaluation of Performance of CMIP5 and CMIP6 GCMs for Flood Projection in the Mekong River Basin

6.1 Introduction

The Mekong River Basin (MRB) is one of the largest international rivers with a drainage area of 795,000 km^2 in China, Myanmar, Thailand, Lao PDR, Cambodia, and Vietnam. The annual flood damages range approximately US$ 60–70 million (MRC, 2011). The flood-related damages dramatically increase from 1984 to 2017 (Try et al., 2018a), and the frequency and severity of extreme flood events have also raised in the MRB (Oddo et al., 2018). Try et al. (2018a) found a significant increase in the trend of population settlement close to the river network and floodplain in the Lower Mekong Basin (LMB) in which most areas are prone to flooding (Try et al., 2019). Climate change was projected to affect the hydrological and ecological system in the LMB, particularly in the Tonle Sap Lake (Burnett et al., 2013; Chadwick et al., 2008; Hoang et al., 2016; Johnstone et al., 2013; Keskinen et al., 2013; Uk et al., 2018) as the interaction from the Mekong River. The natural phenomenon of huge seasonal changes of flood inundation is the home to more than 370 plant species, 197 phytoplankton species, and more than 225 bird species (MRC, 2010). The annual flood deposited the sediment as natural fertilizers as benefits for high agricultural productivity and biodiversity.

Climate models are generated from different research groups worldwide. The research groups update their modeling results according to the schedule of the assessment report of the Intergovernmental Panel on Climate Change (IPCC). The IPCC fifth assessment report (AR5) addressed the Coupled Model Intercomparison Project Phase 5 (CMIP5) in 2013 while the CMIP6 is being launched. The climate projections are scenario-dependent. The IPCC AR5 examined different possible future greenhouse gas emissions addressing by four Representative Concentration Pathways (RCPs). These scenarios were RCP2.6, RCP4.5,

RCP6.0, and RCP8.5 (IPCC, 2014). The new Coupled Model Intercomparison Project Phase 6 (CMIP6) has designed new scenarios called Shared Socioeconomic Pathway (SSP) namely SSP1-2.6, SSP2-4.5, SSP4-6.0, and SSP5-8.5 (Eyring et al., 2016; O'Neill et al., 2016). The improvement of CMIP6 scenarios was increasing equilibrium climate sensitivity (ECS). CMIP5's ECS ranges between 1.5C–4.5C which means that 66% chance of true value falls in that range. However, around 34% extra values of ECS was considered in CMIP6 models. The models in CMIP6 generally have a finer spatial resolution which can raise their capability and reduce uncertainty (Chen et al., 2020).

Generally, the information on climate change effects on a river basin is urgently important to policymakers to prepare the mitigation and adaptation activities. The use of the general circulation model (GCM) in climate change projections usually includes uncertainties from different sources identified as assumptions of greenhouse gas (GHG) emission scenario, model configuration, climate downscaling, and unforced variability of the climate system (Giorgi, 2010). Hoang et al. (2016) marked that uncertainty of hydrological extremes under climate change in the MRB was reduced in CMIP5, compared to the previous CMIP3.

Ruan et al. (2018) evaluated the ranking scores of precipitations from CMIP5 GCMs over the LMB. Chhin and Yoden (2018) proposed a framework for model ensemble selection based on historical simulations of CMIP5 GCMs in the Indochina region, and Chhin et al. (2020) used their optimal ensemble subset for future drought projection. Try et al. (2020b) assessed future climate change impacts on flood inundation in the LMB through high-resolution Atmospheric General Circulation Model from Meteorological Research Institute (MRI-AGCM) in which sea surface temperature from 28 CMIP5 GCMs were used as a boundary condition. Try et al. (2020c) projected the extreme flood inundation in the MRB from a large ensemble database for policy decision making for future climate change (d4PDF) using MRI-AGCM with sea surface temperature boundary condition for six CMIP5 GCMs including CCSM4, GFDL-CM3, HadGEM2, MIROC5, MPI-ESM-MR, and CGCM3. Overall, the previous studies of future projections of flooding in the MRB were based on only previous CMIP3 and CMIP5 GCMs while the performance of CMIP6 over CMIP5 is necessarily required in this area.

To overcome this limitation and to explore more information on the possibility of future flood inundation in the MRB, this paper aims to examine the hypothesis stating that the improving performances of CMIP6 over CMIP5 are expected for flood inundation simulation in the MRB. Then, we are going to investigate the effects of climate change on flood inundation in the MRB using designed scenarios in the near future, mid future, and far future at the end of the 21st century.

6.2 Methodology

6.2.1 Flood Modeling

This study used an integrated model of rainfall-runoff and flood inundation (RRI model, Sayama et al., 2012; 2015a; 2015b). The RRI model is a two-dimensional distributed model dealing with slopes and river channels separately. The RRI model calculates flow on slopes and rivers based on 2D and 1D diffusive wave equations which are able to consider reversed flow. To represent the rainfall-runoff-inundation processes, the RRI model simulates lateral subsurface flow, vertical infiltration, and surface flow. The river geometry is assumed to be rectangular with width W [m] and depth D [m] as equations (6.1) and (6.2) in function upstream drainage area A [km^2]. Try et al. (2018b) calculated the geometry coefficients C_W, S_W, C_D, and S_D with values of 0.0015, 0.7491, 0.0520, and 0.7596, respectively for the MRB.

$$W = C_W A^{S_W} \tag{6.1}$$

$$D = C_D A^{S_D} \tag{6.2}$$

The RRI model has been previously used for several purposes that confirms its good performance and ability to simulate flood inundation in the MRB. Try et al. (2018b) used the RRI model for reproducing a historical flood event in 2000, and Try et al. (2020a) evaluated the performance of satellite-based precipitation products. Perera et al. (2017) and Try et al. (2020b) used the RRI model to evaluate the effects of climate change in the LMB

by considering various Representative Concentration Pathways (RCPs) and sea surface temperature (SST) scenarios. Moreover, Try et al. (2020c) validated the RRI model for long-term simulation (1983–2010) before using for the projection of extreme flood inundation events in the MRB. Therefore, the validated RRI model is used in this study.

6.2.2 Climate Change Dataset

Daily precipitation and evapotranspiration were obtained from https://esgf-node.llnl.gov/search/cmip6/ and https://esgf-node.llnl.gov/search/cmip5/ for CMIP6 and CMIP5, respectively. This study selected eight GCMs from CMIP5, and the updated version of the same GCM was also selected in CMIP6 produced by the same institution with CMIP5. Table 6.1 presents the institution, model name, and spatial resolution of each model. Six GCMs (no. 1 to no. 6 in Table 6.1) have the same spatial resolution in both CMIP5 and CMIP6; however, the other two GCMs (no. 7 and no. 8) have gridded resolution double finer in longitude and latitude in CMIP6 compared to CMIP5.

The reference observed-based precipitation used in this study is the Global Precipitation Climatology Center (GPCC, Ziese et al., 2018) which is available at http://gpcc.dwd.de/. GPCC precipitation was confirmed for its higher accuracy than other four gridded precipitation productions (APHRODITE, PERSIANN-CDR, GSMaP, and TRMM) in the MRB by comparing with gauged precipitation (Try et al., 2020a), and this product was validated for long-term flood inundation modeling in the MRB during 1982–2007 (Try et al., 2020b) and 1983–2010 (Try et al., 2020c). Therefore, GPCC is used as a reference to evaluate the performance of GCMs from CMIP5 and CMIP6.

Table 6.1 Description of CMIP5 and CMIP6 models.

No.	Model Name		Resolution	Modeling Agency	References
	CMIP5	CMIP6	Lon. × Lat.		
1	CNRM-CM5	CNRM-CM6-1	1.40625 × 1.40625	Centre National de Recherches Meteorologiques, France	Voldoire et al. (2013)
2	IPSL-CM5A-LR	IPSL-CM6A-LR	2.5 × 1.25874	Institut Pierre-Simon Laplace, France	Dufresne et al. (2013)
3	MIROC5	MIROC6	1.40625 × 1.40625	Atmosphere and Ocean Research Institute, National Institute for Environmental Studies, Japan Agency for Marine-Earth Science and Technology, Japan	Watanabe et al. (2011)
4	MPI-ESM-LR	MPI-ESM1-2-LR	1.875 × 1.875	Max Planck Institute for Meteorology,Germany	Giorgetta et al. (2013)
5	MRI-ESM1	MRI-ESM2.0	1.125 × 1.125	Meteorological Research Institute, Japan	Yukimoto et al. (2012)
6	ACCESS1-3	ACCESS-CM2	1.875 × 1.25	Commonwealth Scientific and Industrial Research Organization and Bureau of Meteorology, Australia	Bi et al. (2013)
7	GFDL-CM3	GFDL-CM4	1.25 × 1.0*	Geophysical Fluid Dynamics Laboratory, USA	Donner et al. (2011)
8	NorESM1-M	NorESM2	1.25 × 0.9375*	Norwegian Climate Centre, Norway	Bentsen et al. (2013)

*Note: the values describe CMIP6 while their spatial resolution in CMIP5 in both longitude and latitude are double coarser than CMIP6.

6.2.3 Performance Assessment

Taylor (2001) proposed a diagram to provide a concise statistical summary of model performance in a single diagram. This study used the Taylor diagram to quantify the pattern similarity from two variables (i.e., monthly precipitation from observation and GCMs). The correlation coefficient R between two discrete variables f and r of is determined by:

$$R = \frac{\frac{1}{N}\sum_{n=1}^{N}(f_f - \bar{f})(r_n - \bar{r})}{\sigma_f \sigma_r} \quad (6.3)$$

where $\bar{f}$ and $\bar{r}$ are the mean values; σ_f and σ_r are the standard deviation of f and r, respectively. N is the number of data that are both temporal and spatial patterns in this study. The statistical indicator, root mean square difference ($RMSD$), was used to quantify the difference between the two variables f and r:

$$RMSD = \sqrt{\frac{1}{N}\sum_{n=1}^{N}(f_f - \bar{f})(r_n - \bar{r})^2} \quad (6.4)$$

Taylor diagram is used to evaluate the performance of precipitation over the entire MRB. Moreover, the precipitation in three main zones inside the MRB (i.e., the Upper Mekong Basin in China, middle of MRB in Thailand and Lao PDR, and LMB in Cambodia and Vietnam in Figure 6.1) was also examined. The simulated discharge from the RRI model from CMIP5 and CMIP6 was figured out in terms of monthly and annual peak discharge, compared with gauged observation. Finally, the best performance GCMs are selected for future projection to check out the possibility of change of flood characteristics in the MRB in the near future, mid future, and far future.

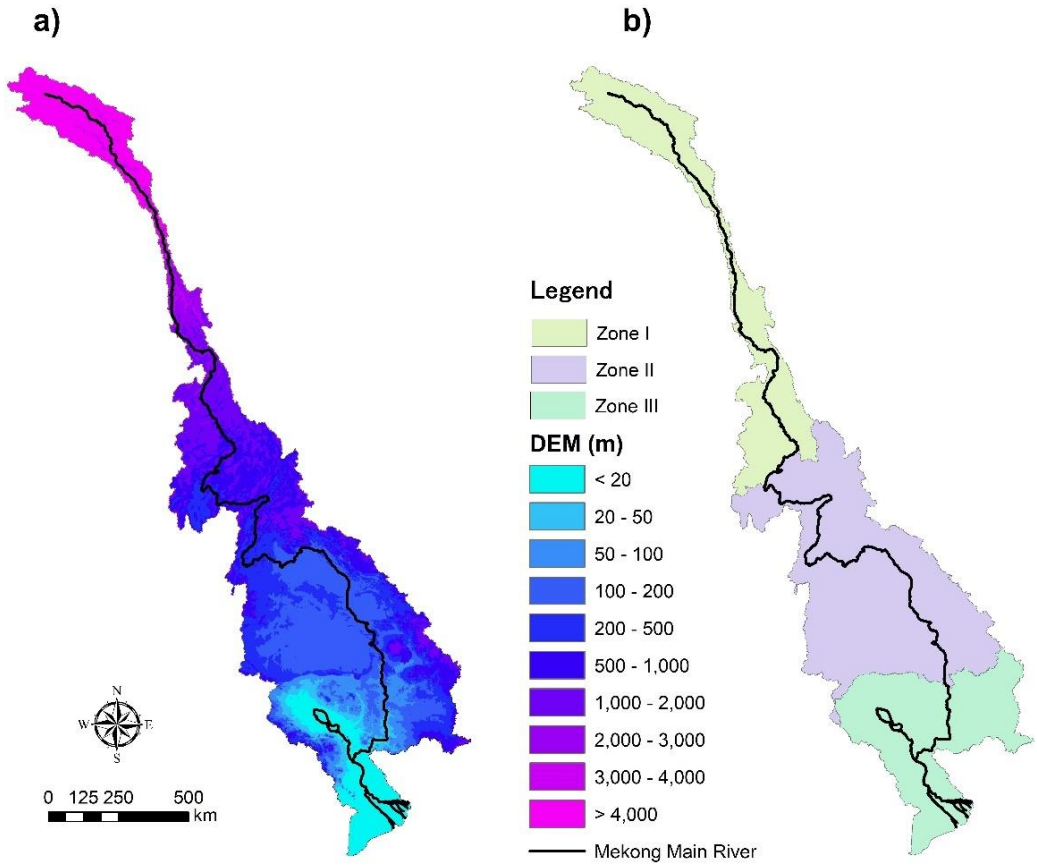

Figure 6.1 Study area of the Mekong River Basin: a) digital elevation model (DEM) and b) three zone for precipitation evaluation.

6.3 Results

6.3.1 Performance of Precipitation

The historical experiments were available for the periods of 1950–2005 and 1950–2014 for CMIP5 and CMIP6, respectively. The results of monthly precipitation based on grid by grid distribution and basin average basin from each GCMs from CMIP5 and CMIP6 were displayed in the Taylor diagram in Figures 6.2 and 6.3, respectively. It is clearly seen that basin average precipitation had higher accuracy in the correlation coefficient (R), root mean square difference (RMSD), and standard deviation (STD). For grid by grid precipitation,

the improvement from the average of eight CMIP5 GCMs with R = 0.48, RMSD = 79.11 mm, and STD = 61.81 mm (STD of GPCC = 87.89 mm) to CMIP6 GCMs with R = 0.58, RMSD = 72.82 mm, and STD = 67.10 mm (Table 6.2). For basin average precipitation, the performance improvement from CMIP5 to CMIP6 was 0.97 to 0.99 for the correlation coefficient, 27.20 mm to 24.67 mm for bias index. However, the standard deviation seems to be larger in CMIP6 110.46 mm comparing to 102.0 mm (STD of GPCC = 101.18).

Table 6.2 Comparison of correlation coefficient (R), root mean square difference (RMSD), and standard deviation (STD) between grid by grid and basin average precipitation from CMIP5 and CMIP6 GCMs.

GCMs		R [-]	RMSD [mm]	STD [mm]		R [-]	RMSD [mm]	STD [mm]
Grid by Grid	GPCC	-	-	87.89		-	-	87.89
	CMIP5	0.55	75.87	67.41	CMIP6	0.55	78.21	75.69
		0.54	73.93	53.18		0.46	81.69	64.95
		0.62	70.53	67.84		0.64	68.34	65.24
		0.46	82.52	66.92		0.38	86.78	63.39
		0.52	75.84	55.73		0.58	72.28	59.12
		0.63	72.21	79.04		0.71	65.67	85.26
		0.40	80.84	43.28		0.62	69.30	60.87
		0.11	101.11	61.08		0.73	60.27	62.24
	avg.	0.48	79.11	61.81		0.58	72.82	67.10
Basin Average	GPCC	-	-	101.18		-	-	101.18
	CMIP5	0.99	17.94	86.95	CMIP6	0.99	20.94	88.01
		0.98	22.74	88.54		0.99	17.79	92.00
		0.96	28.66	94.09		0.99	15.17	94.98
		0.99	19.26	90.10		0.99	16.73	102.33
		0.96	34.67	114.04		0.98	34.26	127.57
		0.93	49.55	126.30		0.98	34.02	127.89
		0.98	20.06	98.84		0.98	41.00	136.52

	0.99	24.74	117.18		0.99	17.46	114.35
avg.	0.97	27.20	102.00		0.99	24.67	110.46

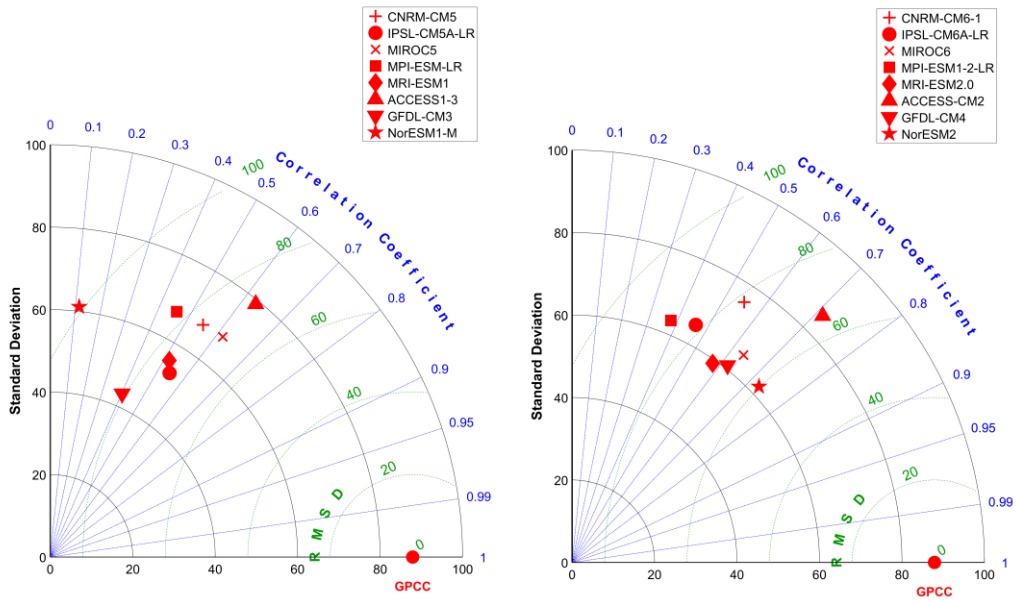

Figure 6.2 Taylor diagram of average monthly precipitation for grid by grid distribution from CMIP5 (left) and CMIP6 (right).

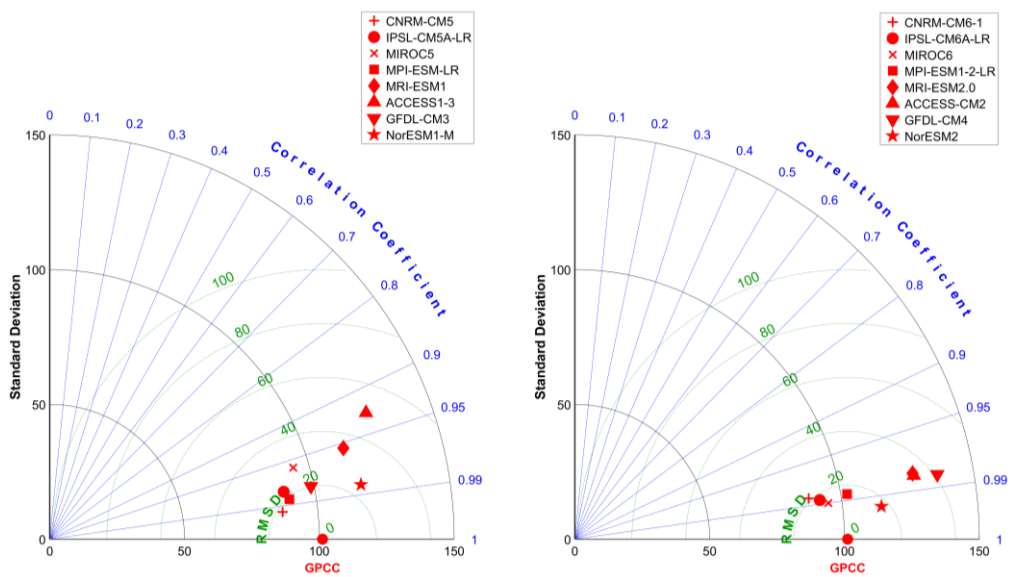

Figure 6.3 Taylor diagram of average monthly precipitation for basin average for CMIP5 (left) and CMIP6 (right).

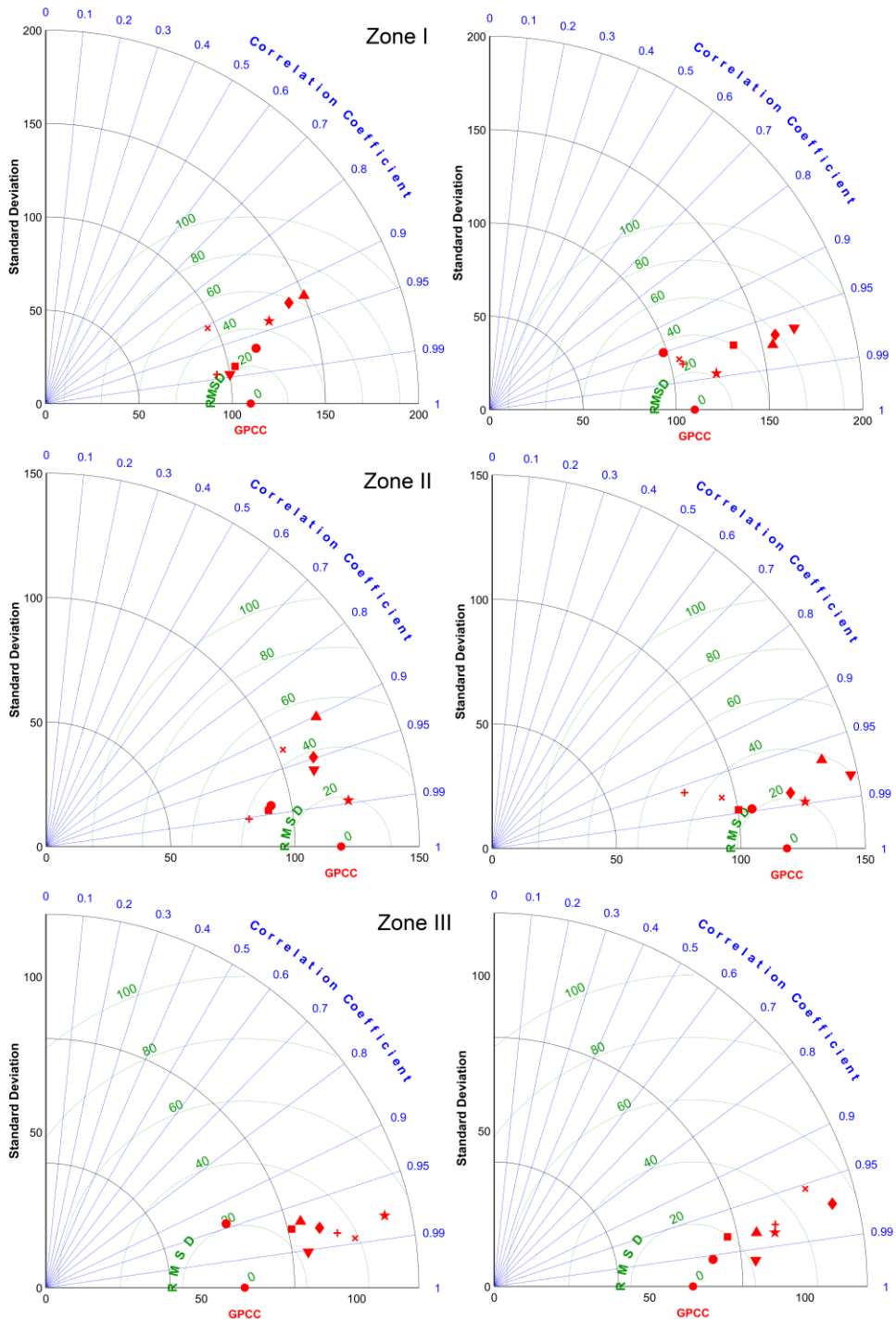

Figure 6.4 Taylor diagram of average monthly precipitation for each zone (I, II, and III) for CMIP5 (left column) and CMIP6 (right column).

Table 6.3 Comparison of monthly precipitation from CMIP5 and CMIP6 GCMs based on each zone: Zone I (upper basin), Zone II (middle basin), and Zone III (lower basin) of the MRB.

	GCMs	R [-]	RMSD [mm]	STD [mm]		R [-]	RMSD [mm]	STD [mm]
Zone I	GPCC	-	-	109.90		-	-	109.90
	CMIP5	0.99	23.85	93.07	CMIP6	0.97	25.22	106.37
		0.97	29.76	116.60		0.95	34.87	97.93
		0.91	46.44	95.79		0.97	28.28	105.05
		0.98	21.57	103.48		0.97	40.29	135.15
		0.92	57.71	141.12		0.97	58.90	158.20
		0.92	63.57	148.83		0.97	54.38	155.66
		0.99	19.19	99.99		0.97	68.93	168.94
		0.94	45.27	127.65		0.99	22.62	123.06
	avg.	0.95	38.42	115.82		0.97	41.69	131.29
Zone II	GPCC	-	-	118.55		-	-	118.55
	CMIP5	0.99	38.59	82.32	CMIP6	0.96	46.88	80.50
		0.98	32.63	91.83		0.99	21.23	105.65
		0.93	45.44	102.82		0.98	33.20	94.50
		0.99	32.60	90.51		0.99	24.91	100.25
		0.95	37.54	113.28		0.98	22.33	122.02
		0.90	53.02	120.34		0.97	38.17	137.18
		0.96	32.69	111.96		0.98	39.10	147.16
		0.99	18.76	122.88		0.99	20.10	127.21
	avg.	0.96	36.41	104.49		0.98	30.74	114.31
Zone III	GPCC	-	-	63.97		-	-	63.97
	CMIP5	0.98	34.58	95.40	CMIP6	0.98	33.09	92.58
		0.94	21.39	61.50		0.99	10.80	70.93
		0.99	38.87	100.70		0.95	47.87	104.92
		0.97	24.14	81.27		0.98	19.42	76.75

	0.98	30.80	90.11	0.97	52.11	112.00
	0.97	27.82	84.60	0.98	26.73	86.13
	0.99	23.44	85.19	1.00	21.84	84.55
	0.98	50.60	111.39	0.98	31.51	91.94
avg.	0.97	31.46	88.77	0.98	30.42	89.97

In addition to precipitation evaluation based on grid by grid and entire basin average, we also investigated three zones displayed in Figure 6.1.b. In general, both CMIP5 and CMIP6 were observed higher performance in Zone III in the LMB (floodplain and delta), following by Zone II (central of the MRB) and Zone I (the Upper Mekong Basin). The tendency of each model distribution in the Taylor plot in Figure 6.4 can be distinguished by an increase of correlation coefficient and reduction of bias index RMSD from CMIP5 to CMIP6. Table 6.3 provides a summary of information on all model performance. For Zone III, the average performance indices among eight GCMs were R = 0.97, RMSD = 31.46 mm, and STD = 88.77 mm (reference to GPCC STD = 63.97 mm) for CMIP5 and R = 0.98, RMSD = 30.42 mm, and STD = 89.97 mm for CMIP6. Similarly, the advancement from CMIP5 to CMIP6 performed by R = 0.96 to 0.98, RMSD = 36.41 mm to 30.74 mm, and STD = 104.49 mm to 114.31 mm (STD of GPCC = 118.55 mm). Among the three zones, Zone I had poor accuracy with R = 0.95 and 0.97, RMSD = 38.42 mm and 41.69 mm, and STD = 115.82 mm and 131.29 mm for CMIP5 and CMIP6, respectively.

6.3.2 Performance of Discharge Simulation

In addition to the evaluation of precipitation, the daily precipitation from all GCMs was used as input to the RRI model to check the ability for simulation of river flow as well as annual peak flood discharge. Figure 6.5 showed a comparison of gauged observation and simulated discharge at Kratie located in the floodplain of the LMB (Try et al., 2020c). During flood season from June to November, the CMIP5 underestimated the river discharge by mean and even though error bar (i.e. mean ± standard deviation), especially, the observation discharge is outside the range of error bar of CMIP5 in July and August. However, its mean results became closer to observation in the late flood period in October-December. The overall performance of CMIP6 was improved during flood season

compared to CMIP5. Particularly, during the peak flood period in September, the mean of CMIP6 was close to the observation while the mean of CMIP5 was an underestimation.

Similar to precipitation and monthly discharge, the performance in terms of annual peak discharge (Figure 6.6) showed a similarity of the performance improvement in CMIP6 compared to CMIP5. While the CMIP5 showed an underestimation of annual peak discharge, the mean from CMIP6 had a good agreement with observation. However, the ranges from lower to upper error bars of CMIP6 was larger than CMIP5 and observation peak discharges.

This study considered wet and dry years as their discharge is higher or less than the average as the threshold. From the observation discharge during 1950–2014, we classified wet and dry years with 31 years (48%) and 34 years (52%). Among the 8 CMIP5 GCMs for the historical experiment (1950–2005), wet years accounted for 137 years (31%), and the remained 311 years (69%) were dry years. The better proportion of CMIP6 GCMs during 1950–2014 was seen by 230 years (44%) and 290 years (56%) for wet and dry years, respectively.

Last but not least, the overall performance from historical experiments from CMIP6 GCMs was better compared to the previous version of CMIP5 for precipitation and flood prediction in the MRB. Therefore, CMIP6 GCMs were used for possible future projection of flood in the MRB as the following section.

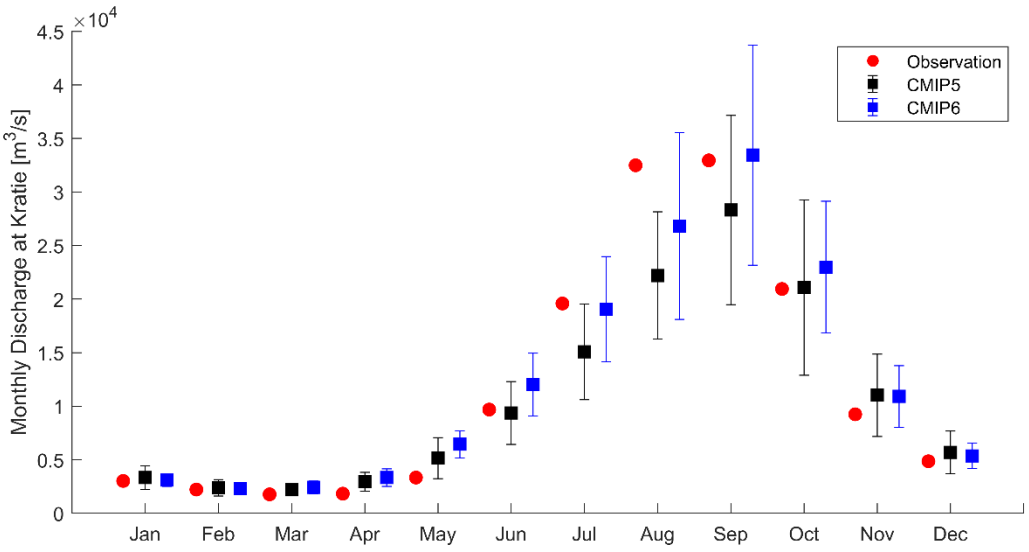

Figure 6.5 Comparison of observed and simulated monthly discharge at Kratie from CMIP5 and CMIP6 GCMs. The central point represents mean, and its lower and upper bars display mean ± standard deviation from model ensembles.

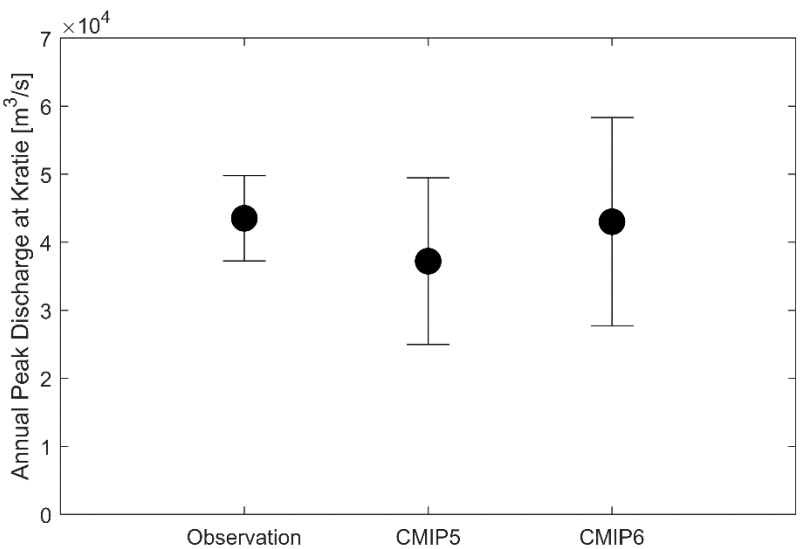

Figure 6.6 Comparison of annual peak discharge at Kratie between observation and simulation from CMIP5 and CMIP6 GCMs. The central point represents mean, and its lower and upper bars display mean plus and minus standard deviation.

6.3.2 Projection of Future Floods

Try et al. (2020c) determined the effective duration of precipitation of 90-day in the MRB correlated with the peak discharge and inundation. For a better representation of precipitation affected on flooding, we, therefore, evaluated the changes of annual maximum 90-day precipitation for the MRB. Figure 6.7 showed 90-day precipitation from the baseline period (1980–2014) to the projected periods in the near future (2026–2050), mid future (2051–2075), and far future (2076–2100) derived from CMIP6 GCMs. Overall, the results indicated that the precipitation would increase for all the future projected periods for both scenarios SSP2-4.5 and SSP5-8.5. According to 8 ensembles from CMIP6 GCMs, the effective precipitation would increase by 4.2 ±5.1%, 6.7±7.2%, and 8.9±11.2% for SSP2-4.5; and 4.0±5.5%, 6.6±7.4%, and 11.6±12.3% for SSP5-8.5 in near, mid, and far futures, respectively.

In addition to the evaluation of the precipitation, the peak flood was also evaluated for the changes for the future projections. The annual peak discharge in Kratie of the LMB was used for the representation of the flooding in the LMB. Generally, the flooding raises up for all considered periods (Figure 6.8). For the SSP2-4.5 scenario, the peak discharge enlarges its magnitude by 10.1±11.8%, 16.4±15.1%, and 17.2±17.9% during the near future, mid future, far future, respectively. Additionally, the peak discharge for SSP5-8.5 sharply increases by 9.9±11.1%, 17.6±14.4%, and 28.9±27.9% for the three periods in the future projection.

The peak discharge in baseline (1980–2014) from the 8 CMIP6 GCMs shows wet years 46% (128/280) and dry years 54% (152/280). This proportion of wet years for the SSP2-4.5 scenario constantly augments to 55% (109/200), 60% (119/200), and 61% (122/200), while the dry years decrease to 46% (91/200), 41% (81/200), and 39% (78/200) for near, mid, and far futures. For the SSP5-8.5 scenario, the ratio for wet years sharply steps up to 56% (44% for dry years), 64% (36%), and 75% (25%), for three projection periods, respectively.

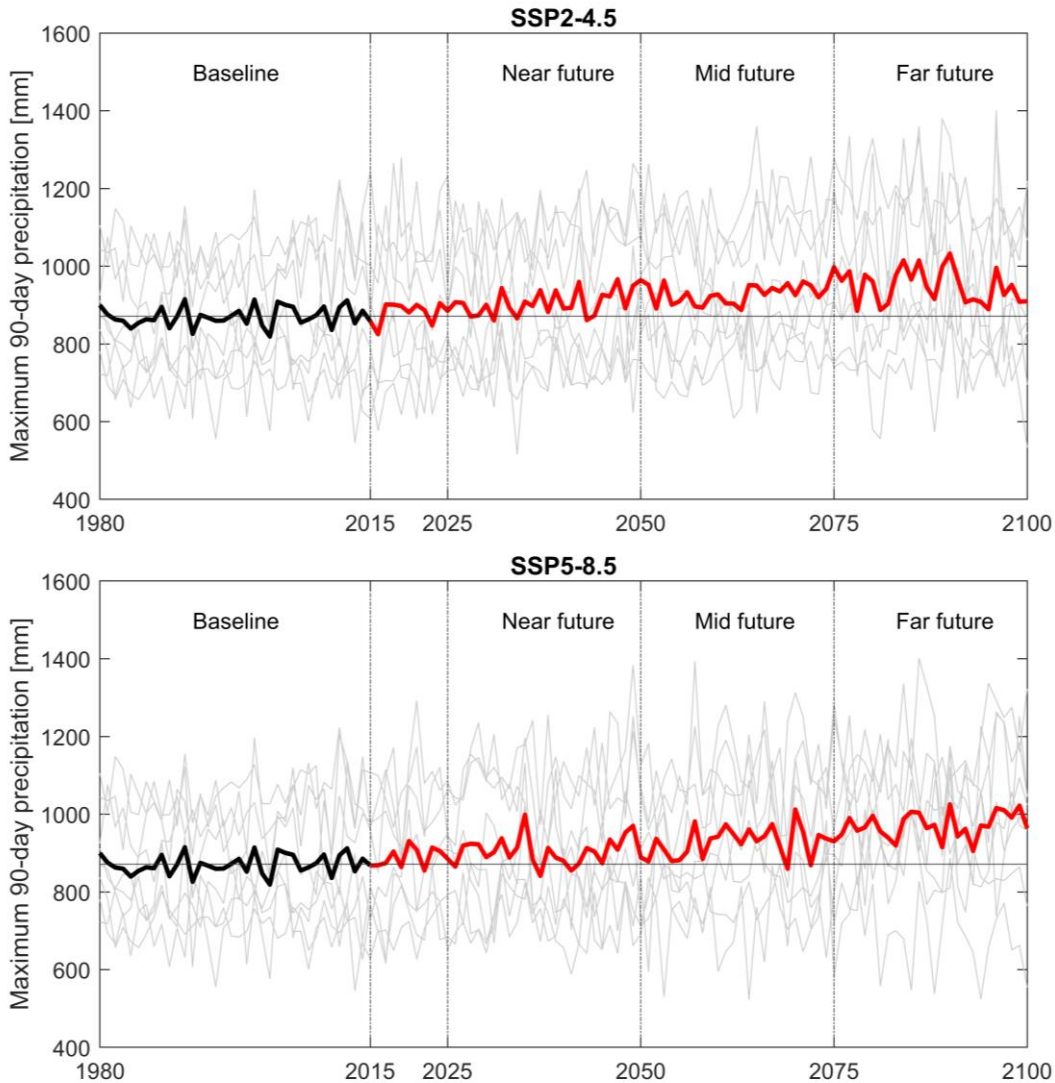

Figure 6.7 Annual maximum 90-day precipitation from baseline to projections in near future, mid future, and far future for SSP2-4.5 and SSP5-8.5. The horizontal straight lines represent mean in baseline period. The central bold lines are mean of model ensembles.

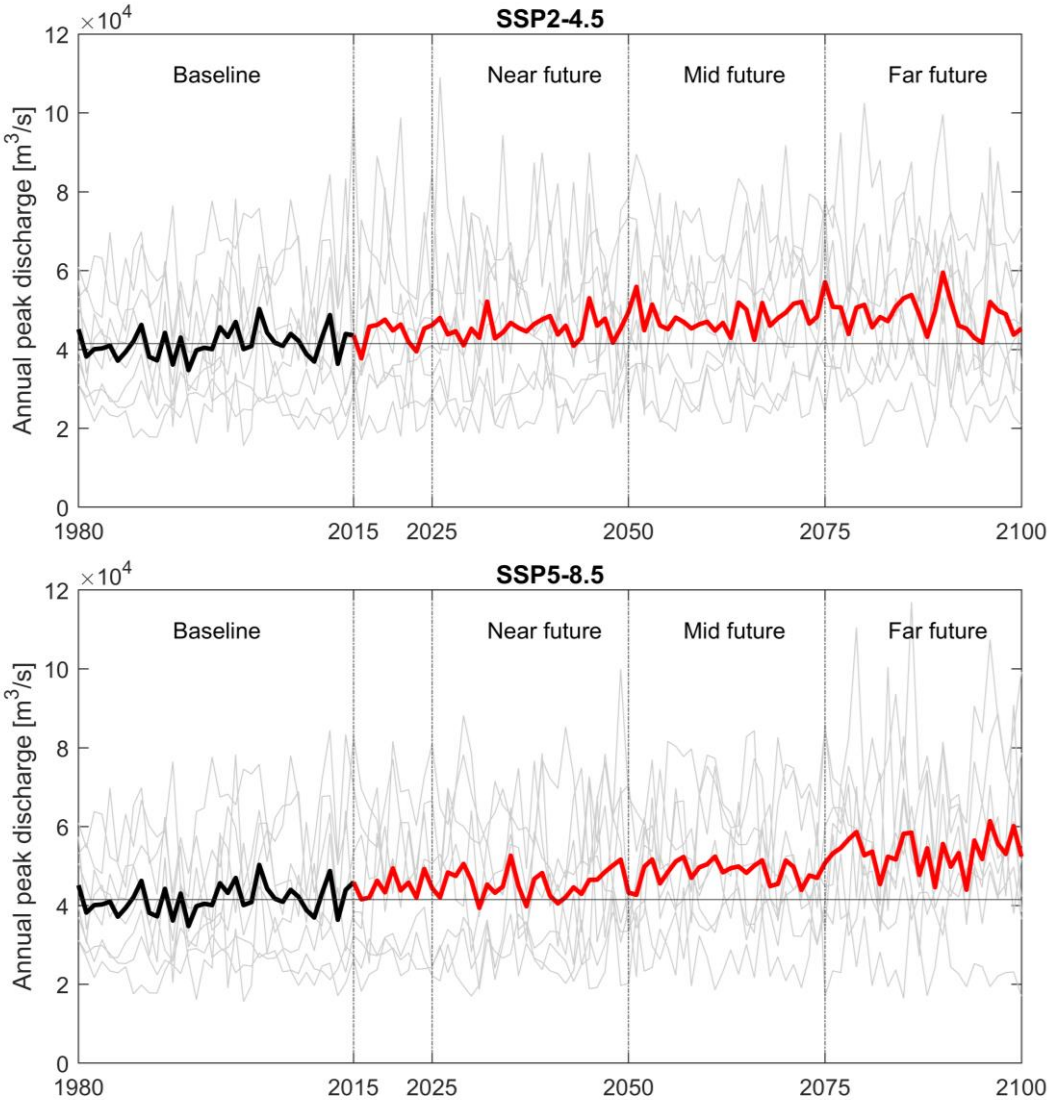

Figure 6.8 Annual peak discharge at Kratie from baseline to projections in near future, mid future, and far future for SSP2-4.5 and SSP5-8.5. The horizontal straight lines represent mean in baseline period. The central bold lines are mean of model ensembles.

6.4 Discussion

The most recent CMIP6 GCMs are expected to improve their characteristics and have better performance for climate simulation over their previous CMIP5. This study analyzed the characteristics of precipitation and flood from 8 CMIP6 GCMs in the MRB by comparing with their sample model from CMIP5According to the Taylor diagram analysis of precipitation based on grid by grid, basin average, and three-zone divisions, the results significantly confirmed the improvement of precipitation from CMIP6 GCMs in term of their correlation and bias values compared with the observation. Similarly, the monthly and annual peak discharge was also ameliorated. Especially, the model ensemble means from CMIP5 expressed an underestimation the values from CMIP6 are close to the observation.

In addition, the projections of future climate in the MRB using the CMIP6 GCMs indicate an increase of both effective precipitation and annual peak discharge in the near (2026–2050), mid (2051–2075), and far (2076–2100) futures by comparing with the baseline period (1980–2014). The increases in peak discharge at Kratie range between 10.1–17.9% and 9.9–28.9% during the three future projected periods for SSP2-4.5 and SSP5-8.5, respectively. These results had a similar agreement with previous studies on the impacts and severity of future climate change in the MRB. For instance, Try et al. (2020b) determined the increase of extreme flow exceeding 5% of times (Q_5) by 13–30% in the projection period in 2075–2099 by comparing to 1979–2003 for ranges of RCP and sea surface temperature scenarios. Similarly, Perera et al. (2017) found the increase of discharge volume in Kratie around 25% for RCP8.5 scenario (comparable to SSP5-8.5 in CMIP6). Vastila et al. (2010) projected annual maximum flood in the LMB for the period of 2010–2049 by changes between -3–14% for A2 scenario in CMIP3 (comparable to RCP8.5 in CMIP5 and SSP5-8.5 in CMIP6).

However, this study used the raw GCMs from CMIP6 without bias correction or downscaling to regional climate yet, the model uncertainties could involve in the result analysis. This study mainly focuses on the evaluation of historical simulation from the climate datasets and the future projection under climate change impact only. To be more

realistic, the cumulative impacts from other sources should be also considered. For example, the land use was assumed to be constant from the baseline to the projected periods. Changes of topography due to soil erosion and deposition were not taken into account. On the other hand, the hydropower and irrigation reservoirs would influence seasonal hydrology and river flow of the river basin. However, the future projections of flooding in this study focus only on annual peak discharge. Try et al. (2020c) found that six mainstream dams in the Upper Mekong River in China during had impact in reduction of annual peak discharge in Kratie only 1% during the period of 2012–2016; therefore, dam reservoirs were neglected in this study. Further studies are needed to assess the cumulative impacts of climate change associated with these land-use changes and water infrastructure development impacts.

6.5 Summary

This study focused on the assessment of the performance of CMIP5 and CMIP6 GCMs in terms of precipitation and discharge simulation in the MRB. The results indicated an improvement of raw CMIP6 GCMs compared to the previous CMIP5 GCMs. Therefore, the studies on climate change impacts on hydrology changes such as floods and droughts using CMIP6 GCMs in the MRB should be more reliable and be carried out as additional information to the results from the previous CMIP3 or CMIP5 GCMs. Moreover, further study should focus on bias correction and downscaling of CMIP6 GCMs to catch up with regional climate and observation and to get finer grid resolution, which is more suitable for spatial distribution, particularly for the studies in the sub-catchments of the MRB. The future projections of flooding in the MRB from 8 CMIP6 GCMs showed a significant increase of effective precipitation as well as annual peak discharge in the near future, mid future, and far future in both SSP2-4.5 and SSP5-8.5 scenarios.

References

Bentsen, M., Bethke, I., Debernard, J.B., Iversen, T., Kirkevåg, A., Seland, Ø., Drange, H., Roelandt, C., Seierstad, I. A., Hoose, C., and Kristjánsson, J. E. (2012). The Norwegian earth system model, NorESM1-M-Part 1: Description and basic evaluation. *GMDD*, *5*(3), pp.2843-2931. doi: 10.5194/gmdd-5-2843-2012.

Bi, D., Dix, M., Marsland, S. J., O'Farrell, S., Rashid, H., Uotila, P., Hirst, A. C., Kowalczyk, E., Golebiewski, M., Sullivan, A., and Yan, H. (2013). The ACCESS coupled model: description, control climate and evaluation. *Aust. Meteorol. Oceanogr. J*, *63*(1), pp.41-64.

Burnett, W., Wattayakorn, G., Kum, V., and Sioudom, K. (2013). Assessing the impact of climate change and development pressures on nutrient inputs into the Mekong River and Tonle Sap, FL, USA.

Chadwick, M., Juntopas, M., and Sithirth, M. (2008). Sustaining Tonle Sap: An assessment of development challenges facing the great lake (pp. 6–9). Bangkok, Thailand: The Sustainable Mekong Research Network (Summernet).

Chen, H., Sun, J., Lin, W., and Xu, H. (2020). Comparison of CMIP6 and CMIP5 models in simulating climate extremes. *Science Bulletin*, 65(17). doi: 10.1016/j.scib.2020.05.015.

Chhin, R., and Yoden, S. (2018). Ranking CMIP5 GCMs for model ensemble selection on regional scale: case study of the Indochina Region. *Journal of Geophysical Research: Atmospheres*, *123*(17), pp.8949-8974. doi: 10.1029/2017JD028026.

Chhin, R., Oeurng, C., and Yoden, S., (2020). Drought projection in the Indochina Region based on the optimal ensemble subset of CMIP5 models. *Climatic Change*, pp.1-19. doi: 10.1007/s10584-020-02850-y.

Donner, L. J., Wyman, B. L., Hemler, R. S., Horowitz, L. W., Ming, Y., Zhao, M., Golaz, J. C., Ginoux, P., Lin, S. J., Schwarzkopf, M. D., and Austin, J. (2011). The dynamical core, physical parameterizations, and basic simulation characteristics of the atmospheric component AM3 of the GFDL global coupled model CM3. *Journal of Climate*, *24*(13), pp.3484-3519. doi: 10.1175/2011JCLI3955.1.

Dufresne, J. L., Foujols, M. A., Denvil, S., Caubel, A., Marti, O., Aumont, O., Balkanski, Y., Bekki, S., Bellenger, H., Benshila, R., and Bony, S. (2013). Climate change projections using the IPSL-CM5 Earth System Model: from CMIP3 to CMIP5. *Climate dynamics*, *40*(9-10), pp.2123-2165. doi: 10.1007/s00382-012-1636-1.

Eyring, V., Bony, S., Meehl, G.A., Senior, C.A., Stevens, B., Stouffer, R.J., and Taylor, K. E. (2016). Overview of the Coupled Model Intercomparison Project Phase 6 (CMIP6) experimental design and organization. *Geoscientific Model Development*, *9*(5), pp.1937-1958. doi: 10.5194/gmd-9-1937-2016.

Giorgetta, M. A., Jungclaus, J., Reick, C. H., Legutke, S., Bader, J., Böttinger, M., Brovkin, V., Crueger, T., Esch, M., Fieg, K., and Glushak, K. (2013). Climate and carbon cycle changes from 1850 to 2100 in MPI-ESM simulations for the Coupled Model Intercomparison Project phase 5. *Journal of Advances in Modeling Earth Systems*, *5*(3), pp.572-597. doi: 10.1002/jame.20038.

Giorgi, F. (2010). Uncertainties in climate change projections, from the global to the regional scale. In *EPJ Web of conferences* (Vol. 9, pp. 115-129). EDP Sciences.

Hoang, L. P., Lauri, H., Kummu, M., Koponen, J., Vliet, M. T. H. V., Supit, I., Rik, L., Pavel, K., and Ludwig, F. (2016). Mekong River flow and hydrological extremes under climate change. *Hydrology and Earth System Sciences*, *20*(7), 3027–3041. doi: 10.5194/hess-20-3027-2016.

Intergovernmental Panel on Climate Change (IPCC), (2014). Sythesis Report. Contribution of Working Groups I, II and III to the Fifth Assessment Report of the IPCC, Geneva, Switzerland.

Johnstone, G., Puskur, R., Declerck, F., Mam, K., Il, O., Mak, S., Pech S., Seak S., Chan, S., and Hak, S. (2013). Tonle Sap Scoping Report. CGIAR Research Program on Aquatic Agricultural Systems. Penang, Malaysia. Project Report: AAS-2013-28.

Keskinen, M., Kummu, M., Salmivaara, A., Someth, P., Lauri, H., Moel, D. H., Ward, P., and Sokhem, P. (2013). *Tonle Sap now and in the future?* Final Report of the Exploring Tonle Sap Futures Study, Aalto University and 100Gen Ltd. with Hatfield Consultants Partnership, VU University Amsterdam, EIA Ltd. and Institute of Technology of Cambodia, in partnership with Tonle Sap Authority and Supreme National Economic Council. Water & Development Publications WD-11, Aalto University, Espoo, Finland.

MRC, (2010). State of the Basin Report 2010, Mekong River Commission, Vientiane, Lao PDR.

MRC, (2011). Planning atlas of the lower Mekong river basin, Mekong River Commission., Vientiane, Laos PDR.

Oddo, P., Ahamed, A., and Bolten, J. (2018). Socioeconomic Impact Evaluation for Near Real-Time Flood Detection in the Lower Mekong River Basin. *Hydrology*, 5(2), 23. doi: 10.3390/hydrology5020023.

O'Neill, B. C., Tebaldi, C., Van Vuuren, D. P., Eyring, V., Friedlingstein, P., Hurtt, G., Knutti, R., Kriegler, E., Lamarque, J. F., Lowe, J., and Meehl, G. A. (2016). The scenario model intercomparison project (ScenarioMIP) for CMIP6. doi: 10.5194/gmd-9-3461-2016.

Perera, E., Sayama, T., Magome, J., Hasegawa, A., and Iwami, Y. (2017). RCP8.5-Based future flood hazard analysis for the lower Mekong river Basin. *Hydrology*, 4(4): 55. doi: 10.3390/hydrology4040055.

Ruan, Y., Yao, Z., Wang, R., and Liu, Z. (2018). Ranking of CMIP5 GCM skills in simulating observed precipitation over the Lower Mekong Basin, using an improved score-based method. *Water*, *10*(12), p.1868. doi: 10.3390/w10121868.

Sayama, T., Ozawa, G., Kawakami, T., Nabesaka, S., and Fukami, K. (2012). Rainfall–runoff–inundation analysis of the 2010 Pakistan flood in the Kabul River basin. *Hydrological Sciences Journal*, 57(2), 298-312. doi: 10.1080/02626667.2011.644245.

Sayama, T., Tatebe, Y., Iwami, Y., and Tanaka, S. (2015a). Hydrologic sensitivity of flood runoff and inundation: 2011 Thailand floods in the Chao Phraya River basin. *Natural Hazards and Earth System Sciences*, 15, 1617-1630. doi: 10.5194/nhess-15-1617-2015.

Sayama, T., Tatebe, Y., and Tanaka, S. (2015b). An Emergency Response-Type Rainfall-Runoff-Inundation Simulation for 2011 Thailand Floods. *Journal of Flood Risk Management*, 10(1): 65-78. doi: 10.1111/jfr3.12147.

Taylor, K. E. (2001). Summarizing multiple aspects of model performance in a single diagram. *Journal of Geophysical Research: Atmospheres*, *106*(D7), pp.7183-7192. doi: 10.1029/2000JD900719.

Try, S., Lee, D., and Lee, G. (2018a). Application of nightlight satellite imagery for assessing flooding potential area in the Mekong river basin. *J. Korea Warer Resour. Assoc.* 51(7), 565-574. doi: 10.3741/JKWRA.2018.51.7.565.

Try, S., Lee, G., Yu, W., Oeurng, C., and Jang, C. (2018b). Large-Scale Flood-Inundation Modeling in the Mekong River Basin. *Journal of Hydrologic Engineering*, 23 (7). doi: 10.1061/(ASCE) HE.1943-5584.0001664.

Try, S., Lee, G., Yu, W., and Oeurng, C. (2019). Delineation of flood-prone areas using geomorphological approach in the Mekong River Basin. *Quaternary International*, 503, 79-86. doi: 10.1016/j.quaint.2018.06.026.

Try, S., Tanaka, S., Tanaka, K., Sayama, T., Oeurng, C., Uk, S., Takara, K., Hu, M., and Han, D. (2020a). Comparison of gridded precipitation datasets for rainfall-runoff and inundation modeling in the Mekong River Basin. *Plos one*, *15*(1), p.e0226814. doi: 10.1371/journal.pone.0226814.

Try, S., Tanaka, S., Tanaka, K., Sayama, T., Lee, G., and Oeurng, C. (2020b). Assessing the effects of climate change on flood inundation in the lower Mekong Basin using high-resolution AGCM outputs. *Progress in Earth and Planetary Science*, *7*(1), pp.1-16. doi: 10.1186/s40645-020-00353-z.

Try, S., Tanaka, S., Tanaka, K., Sayama, T., Hu, M., Sok, T., and Oeurng, C. (2020c). Projection of extreme flood inundation in the Mekong River basin under 4K increasing scenario using large ensemble climate data. *Hydrological Processes,* 34: 4350-4364. doi: 10.1002/hyp.13859.

Uk, S., Yoshimura, C., Siev, S., Try, S., Yang, H., Oeurng, C., Li, S., and Hul, S. (2018). Tonle Sap Lake: Current status and important research directions for environmental management. *Lakes & Reservoirs: Research & Management*, 23(3), 177-189. doi: 10.1111/lre.12222.

Västilä, K., Kummu, M., Sangmanee, C., and Chinvanno, S. (2010). Modelling climate change impacts on the flood pulse in the lower Mekong floodplains. *J. Water Climate Change*, 1(1):67–86. doi: 10.2166/wcc.2010.008.

Voldoire, A., Sanchez-Gomez, E., y Mélia, D.S., Decharme, B., Cassou, C., Sénési, S., Valcke, S., Beau, I., Alias, A., Chevallier, M., and Déqué, M. (2013). The CNRMCM5. 1 global climate model: description and basic evaluation. *Climate dynamics*, *40*(9-10), pp.2091-2121. doi: 10.1007/s00382-011-1259-y.

Watanabe, S., Hajima, T., Sudo, K., Nagashima, T., Takemura, T., Okajima, H., Nozawa, T., Kawase, H., Abe, M., Yokohata, T., and Ise, T. (2011). MIROC-ESM 2010: Model description and basic results of CMIP5-20c3m experiments. *Geoscientific Model Development*, *4*(4), p.845. doi: 10.5194/gmd-4-845-2011.

Yukimoto, S., Adachi, Y., Hosaka, M., Sakami, T., Yoshimura, H., Hirabara, M., Tanaka, T.Y., Shindo, E., Tsujino, H., Deushi, M., and Mizuta, R. (2012). A new global climate model of the Meteorological Research Institute: MRI-CGCM3—Model description

and basic performance—. *Journal of the Meteorological Society of Japan. Ser. II*, *90*, pp.23-64. doi: 10.2151/jmsj.2012-A02.

Ziese, M., Armin, R. S., Andreas, B., Peter, F., Anja, M. C., and Udo, S. (2018). GPCC Full Data Daily Version.2018 at 1.0˚: Daily Land-Surface Precipitation from Rain Gauges Built on GTS-Based and Historic Data. doi: 10.5676/DWD_GPCC/FD_D_V2018_100.

CHAPTER 7 Concluding Remarks and Future Perspectives

7.1 Summary and Conclusion

Climate change impacts on river hydrology and flood inundation have become a global issue attracting the public attention. Climate change drives the spatiotemporal variation of precipitation resulting in changes in frequency and intensity of flooding. The studies of climate change impact on flood phenomena and consequences are important for future control, hazard risk reduction, and improvement of flood resilience and management. The Mekong River Basin (MRB) is located in a zone vulnerable to climate change impact which would affect the local food production, water supply, biodiversity, and environment.

This study focused to provide more detailed information on the possibility of the effects of climate change on flood inundation in the MRB. This research mainly addressed the outcomes as the following. Firstly, the performance of gridded precipitation products was evaluated based on their ability to simulate runoff and flood inundation processes. Next, the possible impacts of climate change were assessed by considering a large ensemble climate dataset (d4PDF), high- and super-high-resolution AGCM outputs (MRI-AGCM3.2S and MRI-AGCM3.2H), and the most recent CMIP6 GCMs.

Five gridded precipitation products were evaluated for their performance for flood inundation in the MRB. The results indicated that GPCC and TRMM had better performance in simulating river discharge and flood inundation than the other three products (PERSIANN-CDR, APHRODITE, and GSMaP). Since GPCC had longer available periods (1982–2016) than TRMM (1998–present) for daily precipitation. Therefore, GPCC is suitable for long-term simulation of hydrological characteristics in the MRB, particularly for the study of climate change impacts on hydrology and flood inundation. In addition, GPCC precipitation is appropriate for use as a reference for bias correction of climate datasets. Its monthly precipitation is available from 1891 to 2016

(version *Full Data Monthly Version 2018*) at various spatial resolutions of 0.25°, 0.5°, 1.0°, and 2.5° at a global scale.

Next, the effective duration of precipitation which has the highest correlation to peak flood inundation was determined, and this duration was used to observe the changes of future precipitation under climate change impact. 90-day precipitation counting backward from the day of peak flooding had the highest correlation with peak discharge and inundation (both $R^2 = 0.81$). According to a large ensemble climate dataset (d4PDF), the changes in future effective precipitation from present climate (60-year: 1951–2010 × 100 ensemble members) to future climate under 4 K increasing scenario (60-year: 2050–2110 × 90 ensemble members) showed a large variation of mean 777–900 mm and standard deviation 57–96 mm. The statistical Kolmogorov-Smirnov (K-S) test identified a significant difference in future sea surface temperature (SST) scenarios (6 future SST scenarios × 15 ensemble members). The extreme flood inundation events of 50-year, 100-year, and 1000-year return periods in the LMB demonstrate an increase of annual peak discharge, inundation extent, and inundation volume by 25–40%, 19–36%, and 23–37%, respectively. The benefits of the application of a large ensemble climate dataset would reduce qualitative uncertainty of future projection of flood inundation.

Additionally, the climate change effects under different RCP and SST scenarios were assessed by using high- and super-high-resolution AGCM output from MRI-AGCM3.2H and MRI-AGCM3.2S models. The results of climate change from the present climate (1979–2003) to the future climate (2075–2099) suggested that the increment of precipitation between 6.6–14.2% could lead to an increase in extreme river flow exceeding 5% of time (Q_5) 13–30%, annual peak inundation extent 19–43%, and annual peak inundation volume 24–55% in the LMB for ranging of RCP and SST scenarios. The statistical K-S test of the spatial distribution of probability and duration of flood inundation showed significance in most areas regardless of RCP and SST scenarios.

The Coupled Model Intercomparison Project Phase 6 (CMIP6) has just been launched as the updated version of the previous CMIP5 GCMs. The performance of the 8 CMIP6 GCMs

was evaluated by comparing their previous CMIP5 GCMs. The Taylor diagram showed results improvement of correlation and error coefficients of precipitation and discharge simulation of the 8 GCMs from CMIP5 to CMIP6. Moreover, there was an improvement of annual peak discharge from mean of CMIP6 GCM ensembles with the observation while the underestimation was seen in CMIP5 GCMs. The projection of future flooding in the LMB using 8 CMIP6 GCMs pointed out an increase of annual peak discharge at Kratie by 10.1 ± 11.8%, 16.4 ± 15.1%, 17.2 ± 17.9% for SSP2-4.5 scenario and 9.9 ± 11.1%, 17.6 ± 14.4%, 28.9 ± 27.9% for SSP5-8.5 scenario, respectively during three projection periods in the near future (2026–2050), mid future (2051–2075), and far future (2076–2100).

This dissertation has analyzed climate change impact on flood inundation in the LMB using various sources of climate outputs including large ensemble climate dataset (d4PDF), high- and super-high-resolution AGCM (MRI-AGCM3.2H and MRI-AGCM3.2S), and the most recent CMIP6 GCMs (Table 7.1). Their performance showed an agreement to reveal the significant increase of the magnitude of extreme flood and inundation in the LMB under future climate projection.

Different climate outputs may have different benefits. The coarse resolution of climate datasets would have less impact on the accuracy of the study for climate change impact on flood inundation in the large-scale river basin (e.g., LMB), but their data quality might be more significant to influence the reduction of uncertainty for future climate projection. The large ensemble members of the climate projection would definitely reduce the qualitative uncertainty of climate projection. However, the climate projection in the tributaries of the MRB or any other small river basin might be still mainly influenced by the resolution of the climate dataset.

Table 7.1 Summary of change of flood inundation in the LMB under different future climate projection

Climate Model	Flood Event	Scenario	Baseline Period	Projection Period	Magnitude Change
d4PDF	50-year return period	+4K	1951-2010	2051-2110	+25%
	100-year return period		1951-2010	2051-2110	+33%
	1000-year return period		1951-2010	2051-2110	+40%
MRI-AGCM3.2H	high flow exceeding 5% of time (Q_5)	RCP2.6	1979-2003	2075-2099	+14%
		RCP4.5	1979-2003	2075-2099	+13%
		RCP6.0	1979-2003	2075-2099	+18%
		RCP8.5	1979-2003	2075-2099	+30%
MRI-AGCM3.2S	Q_5	SST	1979-2003	2075-2099	+18±3%
CMIP6 GCMs	Annual Peak Discharge	SSP2-4.5	1980-2014	2026-2050	+10.1±11.8%
				2051-2075	+16.4±15.1%
				2076-2100	+17.2±17.9%
		SSP5-8.5	1980-2014	2026-2050	+9.9±11.1%
				2051-2075	+17.6±14.4%
				2076-2100	+28.9±27.9%

7.2 Limitations and Future Work

The potential impacts of climate change on flood inundation in the MRB were assessed by using various sources of climate outputs including the d4PDF dataset, MRI-AGCM3.2S, MRI-AGCM3.2H, and CMIP6 GCMs. However, there are some limitations to this study. Firstly, the land use was assumed to be static during the simulation periods to facilitate the simulation condition while the actual land use may change from year to year. The uncertainty sources due to model structure and parameters were not considered. Moreover, the river bed and topography changes were not taken into account in the simulation; in fact, it would vary for the long-term due to soil erosion and deposition. Plus, the impact of water infrastructures such as hydropower and irrigation reservoir were not yet examined in the future projection. Therefore, the future research direction should pay more attention to the study of integrated impacts of climate change, land-use change, and human activities which would provide further understanding and represent more realistic for future characteristics of flood inundation in the MRB. The application of a large ensemble dataset (d4PDF) could reduce the qualitative uncertainty of future projection of flood inundation. However, the future projection of flood inundation was conducted under only one scenario (+4 K increasing) due to the limitation of simulation resources and data availability. Further research needs to consider more scenarios and include bias correction of large ensemble climate data. Even though the CMIP6 GCMs were found to be an improvement of their performance, this study did not apply the bias correction and downscaling of climate data from the global scale to regional climate conditions as well as to get the higher spatial resolution dataset. This would also contain the uncertainty of the projection of future flood inundation.

Appendix A: List of Publications

Peer Reviewed Journals:

Try Sophal, Tanaka Shigenobu, Tanaka Kenji, Sayama Takahiro, Oeurng Chantha. Evaluation of performance of CMIP5 and CMIP6 GCMs for flood projection in the Mekong River Basin. (to be submitted).

Try Sophal, Tanaka Shigenobu, Tanaka Kenji, Sayama Takahiro, Hu Maochuan, Sok Ty, Oeurng Chantha. (2020). Projection of extreme flood inundation in the Mekong River Basin under 4 K increasing scenario using large ensemble climate data. *Hydrological Processes*, 34(22), 4350-4364. doi: 10.1002/hyp.13859.

Try Sophal, Tanaka Shigenobu, Tanaka Kenji, Sayama Takahiro, Lee Giha, Oeurng Chantha. (2020). Assessing the effects of climate change on flood inundation in the Lower Mekong Basin using high-resolution AGCM outputs. *Progress in Earth and Planetary Science, 7*(34). doi: 10.1186/s40645-020-00353-z.

Try Sophal, Tanaka Shigenobu, Tanaka Kenji, Sayama Takahiro, Oeurng Chantha, Uk Sovannara, Takara Kaoru, Hu Maochuan, Han Dawei. (2020). Comparison of gridded precipitation datasets for rainfall-runoff and inundation modeling in the Mekong River Basin. *PloS One*, 15(1). doi: 10.1371/journal.pone.0226814.

Heng Bunmanuth, Oeurng Chantha, **Try Sophal**, Yuzir Ali Muhammad. (2020). Flow regime alteration analysis under climate change in Tonle Sap Sub-basin. *IOP Conference Series: Earth and Environmental Science*, 479 (012007). doi: 10.1088/1755-1315/479/1/012007.

Try Sophal, Lee Giha, Yu Wansik, Oeurng Chantha. (2019). Delineation of flood-prone areas using geomorphological approach in the Mekong River Basin. *Quaternary International*, 503, 79-86. doi: 10.1016/j.quaint.2018.06.026.

Hu Maochuan., Sayama Takahiro, **Try Sophal**, Takara Kaoru, Tanaka Kenji. (2019). Trend analysis of hydroclimatic variables in the Kamo River Basin, Japan. *Water*, 11(9), 1782. doi: 10.3390/w11091782.

Try Sophal, Lee Giha, Yu Wansik, Oeurng Chantha, Jang Changlae. (2018). Large-scale flood inundation modeling in the Mekong River Basin. *Journal of Hydrologic Engineering*, 23(7). doi: 10.1061/(ASCE)HE.1943-5584.0001664.

Uk Sovannara, Yoshimura Chihiro, Siev Sokly, **Try Sophal**, Yang Heejun, Oeurng Chantha, Li Shanshang, Hul Seingheng. (2018). Tonle Sap Lake: Current status and important research directions for environmental management. *Lakes & Reservoirs: Research & Management*, 23(3). doi: 10.1111/lre.12222.

Try Sophal, Lee Daeup, Lee Giha. (2018). Application of nightlight satellite imagery for assessing flooding potential area in the Mekong River Basin. *Journal of Korea Water Resources Association*, 51(7), 565-574. doi: 10.3741/JKWRA.2018.51.7.565.

Presentation and Conference Papers:

Try Sophal, Tanaka Shigenobu, Tanaka Kenji, Sayama Takahiro, Oeurng Chantha. Investigation of extreme flood changes in the Mekong River Basin using +4K climate simulation. *JpGU – AGU Joint Meeting 2020*, 12-16, Jul. 2020, online virtual meeting.

Try Sophal, Tanaka Shigenobu, Tanaka Kenji, Sayama Takahiro, Oeurng Chantha. Flood frequency analysis under climate change impacts in the Lower Mekong using d4PDF dataset. *DPRI annual meeting*, 20-21, Feb. 2020, Kyoto University, Japan.

Try Sophal, Tanaka Shigenobu, Tanaka Kenji, Sayama Takahiro, Oeurng Chantha. Assessing climate change impact on flood inundation in the Lower Mekong Basin. *The 2nd World Congress on Climate Change*, 26-28, Sep. 2019, Berlin, Germany.

Try Sophal, Tanaka Shigenobu, Tanaka Kenji, Sayama Takahiro, Oeurng Chantha. Climate change impacts on flooding in a large-scale basin using high and super-high resolution of Atmospheric General Circulation Model. *Annual conference of Japan Society for Natural Disaster Science (JSNDS)*, 21-22, Sep. 2019, Hokkaido, Japan.

Try Sophal, Tanaka Shigenobu, Tanaka Kenji, Sayama Takahiro, Oeurng Chantha. Climate change impacts on flood inundation in the Lower Mekong Basin using MRI-AGCM3.2S. *Annual conference of Japan Society of Hydrology and Water Resources (JSHWR)*, 11-13, Sep. 2019, Chiba, Japan.

Try Sophal, Tanaka Shigenobu, Tanaka Kenji, Sayama Takahiro, Oeurng Chantha. Future change of inundation in the Mekong River Basin. *The 8th International Conference on Water Resources and Environment Research (ICWRER-2019)*, 14-18, Jun. 2019, Nanjing, China.

Try Sophal, Tanaka Kenji, Sayama Takahiro, Oeurng Chantha, Uk Sovannara, Tanaka Shigenobu. Comparison of satellite precipitation for hydrological modeling. *The 11th Regional Conference on Environmental Engineering (RCEnv-2018)*, 26-27, Sep. 2018, Phnom Penh, Cambodia.

Try Sophal, Tanaka Kenji, Sayama Takahiro, Oeurng Chantha, Tanaka Shigenobu. Comparison of gridded precipitation for river discharge simulation in the Mekong River. *Annual Conference of Japan Society of Hydrology and Water Resources (JSHWR)*, 12-14, Sep. 2018, Mie, Japan.

Appendix B: Shuffled Complex Evolution Algorithm

Shuffled Complex Evolution (SCE-UA) Algorithm

SCE-UA method is a global optimization technique for broad class of problems including hydrological optimization trials. It combines the strengths of Controlled Random Search (CRS) algorithms with the concept of competitive evolution and complex shuffling. The steps of the SCE-UA algorithm are as the following.

Step 1

Initialize. Select $p \geq 1$ and $m \geq n + 1$, where $p =$ number of complexes and $m =$ number of points in each complex. Compute the sample size $s = p \times m$.

Step 2

Generate sample. Sample s points $x_1, \cdots, x_s$ in the feasible space $\Omega \subset \mathbb{R}^n$. Compute the function value f_i at each point x_i. In the absence of prior information, use a uniform sampling distribution.

Step 3

Rang points. Sort the s points in the order of increasing function value. Store them in an array $D = \{x_i, f_i, i = 1, \cdots, s\}$, so that $i = 1$ represents the point with the smallest value.

Step 4

Partition into complexes. Partition D into p complexes, $A^1, \cdots, A^p$, each containing m points, such that $A^k = \{x_j^k, f_j^k | x_j^k = x_{k+p(j-1)}, j = 1, \cdots, m\}$.

Step 5

Evolve each complex. Evolve each complex $A^k, k = 1, \cdots, p$ according to the competitive complex evolution algorithm outline as below:

1. Initialize. Select q, α, and β, where $2 \leq q \leq m$, $\alpha \geq 1$, and $\beta \geq 1$.
2. Assign weight. Assign a triangular probability distribution to A^k, i.e.,

$$\rho_i = \frac{2(m+1-i)}{m(m+1)}, i = 1, \cdots, m$$

   The point x_1^k has the highest probability, $\rho_1 = 2/(m+1)$. The point x_m^k has the lowest probability, $\rho_m = 2/m(m+1)$.

3. Select parents. Randomly choose q distinct points $u_1, \cdots, u_q$ from A^k according to the probability distribution specified above (the q points define a sub-complex). Store them in array $B = \{u_i, v_i, i = 1, \cdots, q\}$, where v_i is the function value of point u_i. Store in L the locations of A^k which are used to construct B.
4. Generate offspring
   (a) Sort B and L so that the q points are arranged in order of increasing function value. Compute the centroid g using the following equation:

$$g = \left[\frac{1}{q-1}\right] \sum_j^{q-1} u_j$$

   (b) Compute the new point $r = 2g - u_q$ (reflection step).
   (c) If r is within Ω, compute the function value f, and go to step (d); else, compute the smallest hypercube H $\subset \mathbb{R}^n$ that contains A^k, randomly generate a point z within H, compute f_z, set $f_r = f_z$ (mutation step).
   (d) If $f_r < f_z$, replace u_q by r go to Step (f); else, compute $c = (q + u_q)/2$ and f_c (contraction step).
5. Replace parents by offspring. Replace B into A^k using the original locations stored in L. Sort A^k in order of increasing function value.
6. Iterate. Repeat Steps 1) through 4) β times, where $\beta \geq 1$ is a user-specified parameter which determines how many offspring should be generate.

Step 6

Shuffle complexes. Replace $A^1, \cdots, A^p$ into D, such that $D = \{A^k, k = 1, \cdots, p\}$. Sort D in order of increasing function value.

Step 7

Check convergence. If the convergence criteria are satisfied, stop; otherwise, return to Step 4.